Title

MICROSTRUCTURAL ASPECTS OF GAS-SOLID REACTIONS

Author

Rau, M-F.

Publication Date

1985

Lawrence Berkeley Laboratory
UNIVERSITY OF CALIFORNIA

Materials & Molecular Research Division

MICROSTRUCTURAL ASPECTS OF GAS-SOLID REACTIONS

M-F. Rau
(Ph.D. Thesis)

January 1985

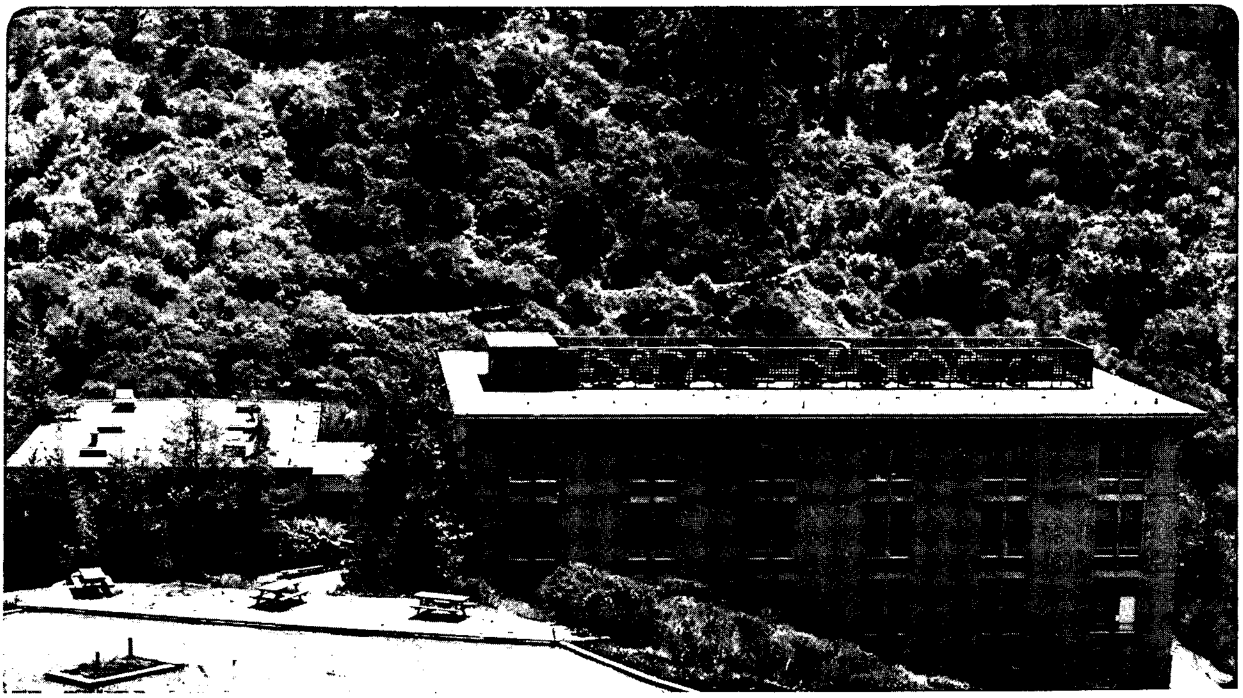

Prepared for the U.S. Department of Energy under Contract DE-AC03-76SF00098

MICROSTRUCTURAL ASPECTS OF GAS-SOLID REACTIONS

Mann-Fu Rau
Ph.D. Thesis

Materials Science and Mineral Engineering
Department of Materials and Molecular Research Division
Lawrence Berkeley Laboratory
University of California
Berkeley, CA 94720

This work was supported by the Division of Materials Sciences, Office of Basic Energy Sciences of the U.S. Department of Energy under Contract No. DE-AC03-76SF00098.

in memory of my father

and to my wife, YU-CHIEN

MICROSTRUCTURAL ASPECTS OF GAS-SOLID REACTIONS

Mann-Fu Rau

Doctor of Philosophy
Materials Science and Mineral Engineering

Chairman of Committee

ABSTRACT

Dynamic studies of the reduction of single crystal iron oxides have been carried out between 300 to 610°C in a high voltage electron microscope using pure hydrogen and hydrogen/argon gas mixtures as reducing agents with pressures up to 50 torr.

The reduction of hematite by pure hydrogen at the temperature below 400°C is via the following path,

$$\begin{array}{c}\text{Single crystal}\\\text{hematite}\end{array} \dashrightarrow \begin{array}{c}\text{Lath}\\\text{magnetite}\end{array} \dashrightarrow \begin{array}{c}\text{Porous}\\\text{magnetite}\end{array} \dashrightarrow \begin{array}{c}\text{Porous}\\\text{iron}\end{array}$$

The reduction fronts appear in hemispherical configurations and the reduction proceeds in a topochemical manner. The transition between hematite and lath magnetite occurs rapidly, so that it may not be seen if the reaction is fast. However, the transition between porous magnetite and porous iron takes place slowly, and appears to be the rate-controlling step. Directional elongated pores form at the interface of lath magnetite and porous magnetite, and spherical pores distribute randomly within the region of porous magnetite. Under the same partial pressure of hydrogen, the reduction rate of hydrogen/argon gas mixture is at least two orders of magnitude slower than the reduction rate of pure hydrogen. The reduction takes place in an internal reaction manner and the product is granular magnetite.

When a single crystal magnetite specimen is exposed to pure hydrogen at 350°C, the formation of pits happens prior to the nucleation of porous iron. The size and the shape of pits change initially but are unchanged after porous iron forms. Iron nucleation takes place near or right on the pits. Iron grows isotropicly when the reaction rate is fast. The reduced magnetite has a circular morphology and locates inside the specimen which implies that an edge is not necessary for nucleation. A pronounced decrease of the rate of reduction was observed when the reducing gas was replaced by hydrogen/argon gas mixtures. At a low reducing potential, e.g. conducting the reaction with a gas mixture, or during the incubation period, the reduction proceeds preferentially along certain directions. The direction with a close packed lattice has been shown to have a faster reaction rate, e.g. <111>.

The reduction of wustite at temperature below 570°C occurs in a complex way. Iron nuclei can be formed via both disproportionation and reduction. At a high reducing potential, the morphology of products is similar to the reduced magnetite. On the other hand, at a low reducing potential disproportionation into magnetite and iron accompanies the reduction.

Increasing temperature and pressure will increase the rate of reduction using pure hydrogan as reducing agent. Dislocations, cracks, edges and thin regions provide active sites for the reduction.

CONTENTS

CHAPTER 2 PREVIOUS STUDIES

CHAPTER 3 EXPERIMANTAL PROCEDURES

CHAPTER 4 RESULTS AND DISCUSSIONS

CHAPTER 1 INTRODUCTION

Gas-solid reactions are one of the most important processes in widely varying branches of technology[1], e.g. the extraction of metals from their ores, the gasification of coal, the utilizing of catalyst in petroleum cracking operations, etc.. From a metallurgical point of view,iron oxide reduction is one of the ancient and the most important process. For example, the blast furnace is still the major process in the ironmaking industry. However, iron ore reduction by hydrogen and carbon monoxide, called 'direct reduction', is a growing industrial process[2-7], especially where high quality metallurgical coke is in short supply but natural gas is readily available. Natural gas can be either directly used as a reducing agent, or converted into hydrogen and carbon monoxide then used for reduction.

A great deal of published papers have been on the reduction of iron ores by hydrogen or carbon monoxide. Most of the investigations observed the strong interrelation between the rate of the reduction and the structure of the products and the original ores, in other words, the kinetics are influenced by the structure.

The microscope is an important tool for the characterization of solid structure. The development in microscopy, from optical to electron microscopy, has contributed much modern science and technology.[8-18] Scanning electron microscopy (SEM) has been widely used for the studies of iron oxide reduction.[19-33] Recently the transmission electron microscope (TEM) has been extensively used,[34-36] because it can provide information down to atomic levels.

A new technique of direct observation of chemical processes occuring in the electron microscope has been introduced. It employs a piece of special equipment, called the 'environmental cell', which is installed on the electron microscope, so that gas-solid reactions can be performed inside the microscope. The main object of this research, taking advantages of the special experimental facilities in the Lawrence Berkeley Laboratory, was to investigate the microstructural changes during the reduction of iron oxides to study the relationship between the structure morphology and the kinetics. To achieve this, in-situ experiments have been carried out on three iron oxides with temperature, partial pressure of hydrogen and type of gas mixture as the controllable parameters.

CHAPTER 2 PREVIOUS STUDIES

2.1 Fundamentals

2.1.1 The Iron-Oxygen System

The temperature-composition diagram for the iron-oxygen system, based on the data of Darken and Gurry,[37] has been recognized for years. (see Figure 1) Within the last two score years, except that Kellogg and co-workers[38,39] used mathematical relations to correlate the thermodynamic properties of the solid and liquid phases in this syatem, no additional thermodynamic data have been published.

Iron forms three solid compounds with oxygen: wustite ($Fe_{1-y}O$), magnetite (Fe_3O_4) and hematite (Fe_2O_3). Some properties of the oxides are listed in Table 1. The crystal structures of the oxides were discussed in detail in the book by Bogdandy and Engell in 1971.[40] Therefore only those topics closely related to the present work will be mentioned in this thesis.

Wustite may contain between 23.1 and 25.6% oxygen. It is a non-stoichimetric compound and unstable with respect to Fe and Fe_3O_4 at temperatures lower than 570°C. Wustite has a rock-salt structure and is normally represented as $Fe_{0.95}O$. The oxygen sublattice is almost fully occupied, while, on the other hand, a number of lattice points in the iron sub-lattice are vacant.[41] The defect structure of wustite has been studied using X-ray diffraction methods by Koch and Cohen.[42] They found that the defects present in wustite are clustered in a periodic array.

Taking advantage of the rapid development in electron microscopy, their observation was confirmed by the evidence from the high resolution images of wustite which have recently become available.[43-45] The decomposition of FeO -> Fe_3O_4 + Fe was observed by Iijima[43] as the wustite specimen was bombarded by an electron beam.

Magnetite crystallizes in a cubic spinel structure in which the oxygen ions form a cubic close-packed array. It is ferrimagnetic with a Curie temperature of 627°C. Magnetite has a lattice constant of 8.396 Å, almost twice the value of wustite, 4.307 Å. The lattice similarity causes a superimposed diffraction pattern which results in difficulties in distinguishing the wustite from the magnetite in coexisting phases, especially if the magnetite is the major phase.

Hematite may exist in two forms with different lattices: (1) α- Fe_2O_3 is of rhombohedral corundum type, the oxygen ions are arranged in a close-packed hexagonal lattice and two-thirds of the octahedral interstices are occupied by ferric ions. (2) γ- Fe_2O_3 is, like magnetite, a cubic spinel type. The structure of this phase may be regarded as a cubic close-packed array of oxide ions with the ferric ions distributed randomly over both the octahedral and the tetrahedral interstices. It may be obtained by oxidation of magnetite below 400°C.

The standard free energy changes, ΔG°_T, for the formation of three oxides from their elements are as follows:

$$2\ Fe + O_2 = 2\ FeO \qquad \Delta G^\circ_T = -124100 + 29.90\ T \quad \text{cal/mole } O_2 \qquad (2.1)$$

$$6\ FeO + O_2 = 2\ Fe_3O_4 \qquad \Delta G^\circ_T = -149240 + 59.80\ T \quad \text{"} \qquad (2.2)$$

$$4\ Fe_304 + O_2 = 6\ Fe_2O_3 \qquad \Delta G^\circ_T = -119240 + 67.24\ T \quad \text{"} \qquad (2.3)$$

In addition to reactions (2.1)-(2.3), two more reactions are important in iron-oxide reduction by hydrogen gas,

$$3/2\ Fe + O_2 = 1/2\ Fe_3O_4 \qquad (2.4)$$

$$2H_2 + O_2 = 2H_2O \qquad (2.5)$$

A plot of the standard free energy change for a reaction versus the temperature is called the Ellingham Diagram. Figure 2 is the Ellingham Diagram for iron, hydrogen and their oxides. From the diagram the free energy of formation of the oxides can be obtained at any temperature in the range over which the data is valid.

2.1.2 The Iron-Oxygen-Hydrogen System

The reduction of iron oxides by hydrogen takes place in three stages at temperature above 570°C and two stages below 570°C. The reactions involved are listed in Table 2. Note that at 298°K all of these reactions are endothermic except the first. The equilibrium constants, the H_2O/H_2 ratio and the equilibrium gas composition can then be calculated. Figure 3 shows the equilibrium gas composition versus temperature diagram for the iron-hydrogen-oxygen system.

2.2 Iron Oxide Reduction

Because of its practical importance, gaseous reduction of iron oxieds has been extensively investigated during the past half century. Much of the early work on iron oxide reduction carried out before 1976 has been summarized.[20, 40, 46, 47] From the results of the previous studies, it is clear that gaseous reduction of iron oxides is quite a complex reaction influenced by many factors, e.g. temperature, partial pressure of gaseous reactant, physical properties of iron oxides and impurities. Although rate equations for iron oxide have been published, none are of universal generality. Many early investigations have to be regarded as incomplete for neglect of one or more factors, especially the structural effects.

Previous works on the reduction of iron oxides can be classified into two categories. The first group has dealt with the kinetics of the reduction of the iron oxides. Its emphasis has been on the determination of the rate-controlling step, the activation energy involved and the reaction rate as a function of reduction temperature, gas mixture compositions, etc.. The second group, on the other hand, has concerned the structure of the solids, either parent oxides or products formed and examined the change of the morphology due to the release of oxygen atoms and the formation of products.

2.2.1 Reaction Kinetics

Bogdandy and Janke[48] studied the reduction of Malmberg ore pellets using hydrogen and water vapor. Their measured value for the apparent activation energy as a function of particle size indicated that the reduction is proceeding under diffusion control for pellets greater than about 15 mm in diameter. Kohl and Engell[10] observed the importance of the form of the iron layer. Under conditions where the iron product forms a nonporous layer the progress of reaction is slowed down considerably. The mechanism of reaction under these conditions was considered to be solid state diffusion.

Using a synthetic magnetite, Quets et al.[49,84] were able to keep the size of the reaction interface unchanged during the course of reaction. They observed that the reaction was directly proportional to hydrogen partial pressure over the temperature range from 400 to 1000°C. A high activation energy obtained indicated that the reaction was controlled by chemical kinetics. A simular approach was used by Lu and Bitsianes[50] to study the reduction of dense natural and synthetic hematites by hydrogen and carbon monoxide. From their experimental results, they noted that diffusion through the ash layer presented a significant resistance to the progress of reaction.

With a low porosity ore, Spitzer et al.[51] presented an extension of the shrinking core model in which allowance is made for the existence of three reaction interfaces within a hematite pellet undergoing reduction to iron.

Seth and Ross[52] studied the reduction of ferric oxide compacts by hydrogen. Mixed control result was reported under the conditions of their experiments.

Many investigators have tried to perform their experiments under conditions such that both the resistances associated with external mass transfer and with pore diffusion are eliminated. For example, the effect of external mass transfer could be eliminated by using high enough gas flow rates. However, the effect of pore diffusion was difficult to eliminate, even by using very thin pellets. For this reason, the chemical reaction rate constant was deduced from the initial rate measurements,[25] when the contribution from pore diffusion was at its minimum. Unfortunately, this method presents difficulties when incubation periods (periods when the reaction accelerates from a low initial rate), such as in studies done by El-Rahaiby and Rao.[26] They investigated the kinetics of reduction of wustite using hydrogen at relatively modest temperatures, ranging from 238 to 417°C. An important new feature of the work is the use of extremely thin, polycrystalline, specimens of wustite (about 50 μm in thickness). Their results of the extent of reaction (α) vs. the time are sigmoid-shaped and exhibit three distinct characteristics: (i) incubation period-flat region, (ii) acceleratory period-intermediate region, and (iii) decaying region-decreasing region. Instead of taking the slope of the initial region, they selected the slope in the region between α= 0.3 and 0.7, which can be considered as a constant rate region. The activation energy obtained, 17.1 Kcal/mole, is in reasonably good agreement with the results from the studies by Turkdogan and Vinters,[21] 18.6 Kcal/mole, and by Feinman and Drexler,[53] 16.7 Kcal/mole. In a simular manner, Rao and his collaborators[32,33,54] have conducted studies on the other two iron oxides, magnetite and hematite. It is worth noting that the activation energies for the hydrogen reduction of dense magnetite specimens is 18.6 Kcal/mole and of dense hematite is 14.6 Kcal/mole. On the other hand, the rate of reduction of hematite is somewhat higher than that of wustite or magnetite. The reason for this behaviour, they thought, is the formation of porous magnetite during the reduction of hematite in the following sequential manner:

Hematite ---> Magnetite ---> Iron

This porous magnetite tends to give faster kinetics owing to the fact that it presents a larger reaction interface to the incoming reducing gas.

Although the value of the activation energy obtained by Turkdogan and Vinters[21] agrees with the result of El-Rahaiby and Rao,[26] the rate constant values reported by the former researchers are significantly smaller than the data reported by the latter ones. The difference is probably due to the influence of pore diffusion. Turkdogan and Vinters not only used a high porosity (roughly 30%) natural Venezuelan hematite, but also have carried out their experiments at relatively high temperatures (500 to 1000°C) which is in a range of mixed control region. Under their experimental conditions, Turkdogan et al. found that the time to achieve a given extent of reduction of a sphere was not proportional to the particle diameter. The result ruled out the possibility of the reaction proceeding according to a chemically controlled shrinking core model. Beyond a particle radius of about one millimeter the initial rate of reaction was found to be inversely proportional to the particle size; this was interpreted as indicating mixed control during the initial stages of reaction. Beyond the initial stages, these investigators believed that pore diffussion was rate controlling for the particles greater than 1mm.

A short note from Szekeley and Karatas[25] presented their experimental measurements on the rate of wustite reduction with carbon monoxide. The wustite specimen was prepared in a cylindrical disk shape with a porosity of 38%. Their results have shown that pore diffusion played an important role in the reaction under the experimental conditions.

Since pores in original ores play an important role in the kinetics of reactions, it was examined by Koo who[55] characterized the structural properties of Venezuelan Cerro Bolivar ore. He found that the most active ore has much smaller pore surface area and lower porosity but with larger mean pore size. These three parameters, i.e. surface area, porosity and mean pore size, are important structure factors in determining the rate of iron ore reduction.

An interesting task, the effect of magnetic field on reduction of hematite has been carried out by Skorski.[56] He performed a reaction of reduction of fine hematite powder by pure hydrogen in tube type electric furnace with or without a magnetic field. He found that the rate of the reduction of hematite by hydrogen was increasing with the intensity of magnetic field from 500 to 1400 oersted. He concluded that this effect was attributed to the magnetic properties of hydrogen itself, because neither CH_4 nor CO produced a similar increase when under the same conditions. Although Svare[57] disputed this explanation, Peters[58] offered an alternative one, based on thermodynamics, which indicated that an increase in reaction rate is expected under the influence of a strong magnetic field when the reactants were relatively non-magnetic and the products were strongly magnetic. However, this explaination could not confirm the results obtained by Rowe et al.[59] who investigated the effects of magnetic field on reduction of magnetite and wustite. The results are as follows:

Fe_2O_3 --> Fe_3O_4 --> Fe	reduction is speeded up
Fe_3O_4 --> Fe	"
FeO --> Fe	reduction is slowed down

No resonable explanation was given.

2.2.2 Observations of Structural Changes

Turkdogan et al. concluded that no single rate equation can be derived to describe the reaction mechanisms. The problem lies in the complex morphology change of either product or parent oxides during the reduction period. They suggested using X-ray and microscopic examination of the reduced samples for better understanding the nature of the rate-controlling processes. Most of the recent studies on the kinetics of the iron oxides reduction looked into the importance of structural effects, either macroscopically or microscopically.

Due to difference in specific volume and crystal structure of iron oxides and iron, the morphology of samples before and after reduction could not be the same. The most common case is the porous structure formed after reduction, e.g. sponge iron is the typical iron product from direct reduction of iron ores.

Edstrom et al.[8, 9] using optical microscopy studied the relation between microstructure and reduction rate. They found differences in the reducibility of hematite and magnetite and noted that the faster reduction of hematite is due to an earlier and more extensive formation of pores in the reaction products.

Themelis and Gauvin[19] studied the reduction of their model oxide spheres with hydrogen at temperatures between 500 and 1100°C. By the help of optical microscopy, they observed that reduction was initiated at the surface of the particle and proceeded inwards by means of diffusion of the reducing gas through the micropores of the reduced layer. The reduction rate increased with increasing of the temperature up to 600°C and slowed down above 600°C due to the crystallization of the reduced layer which inhibited the access of reducing gas to parts of the unreduced core.

Bradshaw and Matyas[16] investigated the reduction mechanism of hematite pellets to magnetite by using porosimetry and light microscopy. They noted that the rate of formation of magnetite nuclei exerted a limiting effect on the rate of reduction.

Turkdogan et al.[20, 21, 60] have carried out a very through examination of iron produced by gaseous reduction of iron oxides. They found that the pore surface area decreased with increasing reduction temperature. Using scanning electron microscopy, they observed that no further structural changes on holding the iron at temperature once reaction had been completed.

St. John and Hayes[27] investigated the morphology change of wustite specimens reduced by H_2/H_2O gas mixtures between 600 and 1000°C. They observed that faceted pits occured prior to iron nucleation when the wustite specimen was reduced in 1 atm pure H_2 at 1000°C, and the porous iron formed subsequently on the same specimen. At temperatures lower than 900°C, the pit formation before iron nucleation was much less pronounced. Three types of product morphology could be formed: (i) porous iron, (ii) a porous wustite covered with dense iron, and (iii) dense wustite covered with dense iron. They noted that the pore sizes produced, in general, increase as the reducing gas composition approaches that of the Fe/FeO equilibrium composition. The kinetics of a similar system has been studied by Moukassi et al..[28] They showed that the existing 'rate minimum' is connected with the iron texture evolution toward a dense layer of metal which acts as a barrier against the

the diffusion of gas through the pores.

Not only the form of products, but also the shape of pores depends on temperatures. Brill-Edwards et al.[11] studied the reduction of polycrystalline hematite and observed, in a cross-section view, that randomly distributed spherical pores formed at temperature between 400 and 700°C, while directional elongated pores appeared between 700 and 900°C. The hematite/magnetite interface was found to be hemispherical at temperature below 600°C and elliptically conical at higher temperature . However, configurations may be totally different when a cross section was chosen from an orthogonal view, e.g. an apparently spherical pore may change into a groove if the pore is of a cylindrical type. Pluschkell et al.[14] and Rao[15] used a hot stage microscope; they performed a direct observation of the growth of the iron phase on wustite. The iron nuclei grew in a circular configuration on the wustite specimen surface, however, its cross-section is of a spherical lens shape which resulted from a nonisotropic growth of the metal nucleus.

The formation of two distinct morphological types of magnetite during the reduction of hematite has been observed by several groups of researchers.[11, 17, 18, 34, 35, 61] They stated that porous magnetite was the low temperature transformation product and that lath magnetite was favored at high temperatures. Furthermore, Swann and Tighe[34] found that lath magnetite acted as nuclei for porous growth and, on the other hand, nuclei containing purely porous growth appeared without prior lath formation. However, there is some disagreement on the temperature range over which this transition takes place. Hayes and his collaborators noted that the transformation depends not only on the temperature of the reduction, but also the oxygen potential of the reducing gas mixtures.

Summarizing the previous studies, it is well known that the shape, the size and the porosity of original particles play an important role in reduction kinetics. Furthermore, during reduction, the formation of pores and products can change the reaction rate significantly in either direction , e.g. the formation of porous magnetite can accelerate the reduction of hematite, on the other hand, the formation of dense iron can reduced the reaction rate. Therefore, in order to interprete the kinetics data, a knowledge of the microstructural change is necessary.

2.3 Electron Microscopy

2.3.1 Conventional Electron Microscopy

The importance of using X-ray and microscopy to study the kinetics of iron oxide reduction is well understood. The morphologies of the products are revealed by microscopy and the compositions of the products are examined by X-ray diffraction; normally these two techniques are carried out in a separate manner. However, the modern electron microscope, either scanning electron microscope (SEM) or transmission electron microscope (TEM), makes it possible to perform two techniques in one instrument easily and precisely. The SEM equiped with X-ray analysis,[62] for instance, is gradually becoming standard equipment in every laboratory. TEM, on the other hand, has both functions:[83] in the microscopy mode, morphologies of microstructure can be obtained in detail; in the diffraction mode, a diffraction pattern provides basic crystallographic imformation such as (i) the orientation of the specimen, (ii) orientation relationships between crystals, and (iii) qualitative phase identifications. Or more sophisticated scanning transmission electron microscrope (STEM) can even do chemical analysis inside TEM.

Therefore, many recent investigators have utilized either SEM or TEM to study reaction mechanisms at a much finer scale (which can not be reached by using an optical microscope.) For example, a surface groove or porous fracture is shown in a dark band with a light microscope, which may be mistaken for a new phase or precipitate without examining it in a SEM. Further more, without making use of the TEM, it is impossible to study the effect of defects, such as dislocations[63] and domain boundaries,[64] on the nucleation of metals, or to see the epitaxial growth of metals at the early stage of metal oxide reduction.[63]

2.3.2 Controlled Atmosphere Electron Microscopy

2.3.2.1 Development and Design

In spite of the high power of SEM and TEM, information obtained, either in a form of micrographs or diffraction patterns, still do not reveal the true history of reduction. Important occurrences during the reaction of reduction can not be recorded with normal electron microscopes. The problem is solved by attaching a special stage, called the 'environmental cell' (E-cell), into the microscope in the such a manner that it is possible to produce a controlled atmosphere around the specimen (which can be heated at the same time.) Hence, reactions between gases and solids can be directly observed and continuously followed, with specimen temperature, gas pressure and gas composition as controllable parameters. This design has been employed on light microscopes,[15,65] SEM[24,66,67] and TEM.[68] The method applied in this research belongs to the last, therefore, only the design on the TEM will be described.

An E-cell (Figure 4) consists of a chamber around the specimen into which a controlled flow of a chosen gas can be introduced. The basic design requirement with such a device is to contain the environment within the cell so that the main microscope vacuum remains undisturbed. Gas leakage from around the specimen into the column vacuum occurs, but is controlled by the size of the apertures supplemented in some instances by the provision of differential pumping. The thickness of the environment must be kept to a minimum to achieve sufficient electron transmission through the cell so that images of satisfactory quality can be obtained. However, this conflicts with the need to have adequate space for independent specimen tilting and translation, and the provision of heating attachments in the cell gap, and so for most designs a compromise is necessary for the aperture spacing. A gas reservoir with a capacity large in comparison with the leak rate through the apertures must be provided to ensure that the gas inlet pressure measured is the same as that in the cell.

The designer is less restricted when it comes to E-cell installations in high voltage electron microscropes (HVEM). The increased gap between upper and lower objective pole pieces allow sufficient room to accommodate a stage large enough to incorporate heating attachments and also provide full specimen translation and tilting.

There has been steady development in the E-cell designs since fifty years ago, and several recent reviews[69-71] indicate the accerated interest in E-cell work brough about by the availability of HVEMs. An E-cell designed by Swann and Tighe[72] in 1971 equips most functions as shown on Table 3, and it is the same E-cell design used at the Lawrence Berkeley Laboratory.

2.3.2.2 Advantages and Disadvantages

There are several advantages to do in-situ studies in the E-cell:

(1) In-situ experiments offer a valuable insight into gas-solid reactions. In this study, for example, it was possible to investigate the early stages of nucleation and then growth could

be followed. Both of morphology and crystallograph of the products could be verified.

(2) Sample preparation is not necessary after reaction, so that the posibility of having structure induced during polishing is ruled out. For example, a reduced layer of lower oxide, such as magnetite and wustite is weak and brittle and is easily chipped off. The metallic layer is so soft that micro pores smaller than 1 μm are easily embedded and appear as a dense layer.

(3) In-situ experiments consume small amount of materials. From an economic point of view, it is reasonable to use high purity single crystals, normally expensive and hard to obtain, to perform the experiment. The result is more realistic since a lot of factors which might influence the reaction rate are illuminated. For example, impurities may accelerate the reaction rate and grain boundaries may act as nucleation sites. Another reason to use single crystal is to confirm that the reduction products from iron oxides should be porous. Most of the previous work done does not give any definite information on the porosity of the different phases, as the specimens already contained considerable porosity or cracks.

(4) The temperature distribution is nearly uniform over the specimen, so that no hot spot or temperature gradient takes place. The reduction process occurs under isothermal conditions. The large temperature difference found between the core and surface of pellets is avoided.[40]

(5) Rapid achevement of reaction temperature.

Although in-situ study in HVEM gives a few advantages, it may bring several disadvantages, too.

(1) The experimental set up is costly. The cost of an E-cell is not

prohibitive, but a HVEM is scarce and expensive. Maintenance requires expertise.

(2) Because specimens are thin foils, cross-section information can not be obtained.

(3) In-situ studies of gas-solid reactions are critically influenced by the nature and cleanliness of the specimen surface. Careful specimen preparation is required.

(4) Radiation damage of the specimen should be considered. The nucleation and growth of new phases may be enhanced in the area being exposed to the beam.

(5) Contamination is hardly avoidable. It is wise during specimen examination not to linger on one particular area of the specimen too long, otherwise sufficient contamination may build up to either initiate or suppress the reaction.

2.3.2.3 In-situ Studies

In-situ studies of gas-solid reactions have been widely carried out in gas reaction cells. A great number of studies have been focused on the oxidation of metals, alloys and semiconductors,[73] and a few on reduction of metal oxides.[35,74-77] Other applications include: catalytic effects of metal particle on graphite surface,[67] crystal growth by chemical vapor deposition,[78] and thermal decomposition of the ammonium salt.[62,79]

Swann and his collaborators[34,35,80] have carried out a series of in-situ studies of the reduction of iron oxides in their designed E-cell in the AEI EM7 electron microscope. They have performed a very detailed study in the reduction of hematite to magnetite using H_2-He and CO-CO_2

mixtures as reducing gases. A hematite specimen was reduced by 50 torr 5%H_2/95%He gas mixture at 450°C for 2 min then was cooled to 350°C to reduce the rate of reaction sufficiently to obtain sharp micrographs. It was found that the magnetite produced by the reduction formed in colonies with scalloped boundaries. Stereo-microscopy showed that the magnetite was surface nucleated and grew inwards, as well as parallel to the hematite surface, and also that a network of fine pores or tunnels formed initially in the hematite, with magnetite on the tunnel walls. The kinetics and morphology of the oxide reduction reaction also depended on the reducing gas used. Magnetite formed in CO at 500°C, for example, was seen to grow in the form of dendrites, having mid-ribs lying approximately along the $\langle 10\bar{1}0 \rangle$ directions. The most important variable affecting magnetite morphology was observed to be the reduction temperature. At $\leq$ 650°C, the hemispherical magnetite colonies contain a network of tunnels connecting the reaction interface to the gas environment, but at $\geq$ 850°C, there is a strong tendency for the magnetite to form as plates. Between 650 and 850°C, an intermediate structure developed.

CHAPTER 3 EXPERIMENTAL PROCEDURE

3.1 Materials

The iron oxides were obtained from three different sources. Wustite single crystal boules grown by skull melting[81,82] was supplied by Harrison, Aragon and Sandberg, all at Purdue University. Magnetite single crystal slab was prepared in the Argonne National Laboratory and was donated by Peterson at the University of Chicago. Neither the source of the hematite single crystal slab nor the method used for the crystal growth is known. However, the hematite sample has been examined by spectrographic analysis. The composition in oxide is as follows:

Fe	principal constituent
Al	0.004%
Ti	.004
V	.003
Mn	.001

Four different gas mixtures were used for this research. The data are listed in Table 4. In order to meet the safety requirement, the cylinder of pure hydrogen was purchased in a size #6 (3 in X 12½ in). The other gases came in a regular size #1A (9 in X 52 in). The content of pure hydrogen and 10% H_2/90% Ar has been analyzed using an AERO VAC mass spectrometer (MONITORR 722). The results shown in Figure 5 indicated that the residual oxygen in the cylinders is negligible.

3.2 Specimen Preparation

The specimen preparation techniques for three oxides were essentially the same. Discs approximately 1 mm in thickness were cut from the boule or slab. For easy handling, discs of oxide were mounted on a piece of quartz disc which is one inch in diameter and half an inch in thickness. After mounting, the discs were hand ground on #600 silicon carbide paper and then polished using 6 μm and 1 μm diamond paste to produce a smooth surface. The discs were turned over and ground on silicon carbide paper to approximately 4 mils (about 100 μm) and then ground further using diamond paste to about 2 mils. The final step was to cut the discs into between 1mm and 2 mm pieces and mount them on 3mm nickel grids with a ceramic glue Aremco 503. Other glues like epoxy or silver paste were not suitable for this study since they would evaporate at elevated temperatures and block the aperture of the E-cell. Copper grid was avoided because it would alloy with the material of the hot stage furnace which was made of Inconel. After mounting, the specimens were placed in an ion-beam mill for further thinning until a hole appeared. Initially, the samples were thinned at an angle of incidence of 25° using 6 kV. When they were very thin, the angle of incidence was 10° and 5 kV was used. In order to reduce the transformation between wustite and magnetite, a cold stage was used for preparation of wustite specimens. Thereafter, the specimens were ready to be loaded into the E-cell on the HVEM for microscopy.

3.3 Electron Microscopy

Most of this research work was conducted on the Hitachi HU-650 electron microscope and occasionally on the Kratos EM-1500 electron microscope. Both are at the Lawrence Berkeley Laboratory. Accerating voltages were 650 kV and 500 kV on the Hitachi microscope and 1.5 MV and 1.1 MV on the Kratos microscope.

Both microscopes are equiped with an E-cell designed and made by the Gatan Co., with a single tilt heating specimen hot stage is shown on Figure 6. The heating element is 0.003 inch platinum wire with 45 turns and is surrounded by the Aremco 503 ceramic as an insulator. The furnace which is made of Inconel (a Ni and Cr based alloy) conducts heat through the nickel grid to the specimen. A stainless steel (304 type) screw is used to fix the position of the mounted specimen and give a good contact between the nickel grid and the furnace. The temperature is measured by attaching a type R thermocouple (Pt/Pt-13%Rh) to the outside of furnace. The temperature difference between the furnace and the specimen has been measured by connecting another thermocouple to a nickel grid in the furnace under a vacuum condition. The result shown in Figure 7 indicates that the higher the heating temperature, the larger the variation. It is expected to have a larger divergence if the test is conducted in a higher pressure environment. This is because of greater heat transport from the specimen into the gas at higher gas pressure. Other accessories include a hot stage power supply built by the same company with a model no.580-0301. Theoretically, a maximum temperature of 910°C can be obtained in vacuum with a 1.608 amps current input. In practice the maximum temperature achieved depends on the type, composition and pressure of the gas mixture used in the E-cell. The temperature- hot stage current calibration curves in different reducing gases is shown in Figure 8. One reason for not using a hydrogen/helium mixture is because helium has a high thermal conductivity which reduces the maximum temperature significantly.

A schematic diagram of the experimental set-up is shown in Figure 9. In order to reduce the possibility of leaking from connections, gas mixtures were directly applied to the E-cell without purification. The flow rate of gas mixtures is a function of pressure . It has been measured by a Hastings flowmeter (model no. NALL-500) which was connected between the gas cylinder and the pressure gauge. The flow rate-pressure calibration curve for 10%H_2/90%Ar gas mixture is shown in Figure 10. However, the flow meter was disconnected when the calibration has been accomplished. The mechanical pump provided the differential pumping when the valve #3 was opened. The valve #2, a needle valve, should be opened carefully and always operated at the last. Whenever the three valves were opened, gas mixture started to leak into the optical column pressure was necessary in order not to discharge the high voltage due to an abnormal pressure increase. Ten minutes were necessary for the pressure to reach a stable reading.

The electron beam was scattered when the gas mixture filled the E-cell. This resulted in foggy images especially at higher pressures. The specimens were pre-examined and recorded by taking photographs before applying current to the hot stage. The desired reaction temperature could be obtained from the previous calibration data for inputting a certain amount of current. The starting time of the reaction could clearly be defined since the temperature could get up to the expected values within ten seconds. Specimens drifted during the period of heating up making recording difficult, especially when the reaction rate was fast. In order to overcome this problem, reaction driving forces were chosen as low as possible. For example, using just a slightly positive pressure could slow down the reaction rate, which made possible the recording of the early stages of nucleation. It was necessary to stop the reaction at a low extent of the reduction because the highly reduced specimen might fall apart due to the formation of the porous products.

Shutting off was done in a reverse order. Failing to do this caused the temperature to jump up and overheat the wire of the hot stage. Specimens were saved and re-examined after the E-cell was removed from the mocroscope. In the conventional mode, a double tilt holder could be used to do structural analysis. Also, more information from the electron diffraction pattern could be obtained. (Note that only a portion of the whole diffraction pattern can be viewed with the E-cell in the microscope.)

Usually it was necessary to have assistance in operating the electron microscope; one investigator did microscopy while the other monitored accessories and kept records. Especially when reaction proceeds rapidly, there is not enough time for taking notes between shooting photographs. However, when no helper is available, then a tape recorder can play an important role. Some data can not be recorded as micrographs, for instance, the best way to record an incubation period is by taking notes.

CHAPTER 4 RESULTS AND DISCUSSIONS

4.1 Hematite Reduction Studies

Although Swann and his collaborators have advanced the study of the reduction of hematite by directly observing the reduction progress in HVEM, their consideration was focused on the transformation between hematite and magnetite, the first stage of the reduction of hematite. The further reduction of magnetite to wustite, or iron has never been explored by this methodology.

Before reducing, a portion of the surface of hematite specimen was observed having a distribution of precipitate in a size range of a hundredth micron (Figure 11). An inserted electron diffraction pattern shows a group of uniform rings overlapping a single crystal pattern. The ring pattern is recognized of magnetite and the regular pattern, certainly, is of the matrix of hematite. Presumably these precipitates were not formed during the crystal growth of hematite, but were introduced during the preparation of specimens. The specimen might have been exposed to a reducing atmosphere, e.g. in ion beam milling process. The ring pattern indicates that no preferential direction for the formation of magnetite precipitates.

4.1.1 Reduction with pure hydrogen

Having been exposed to 2 torr pure hydrogen at 387°C for 2 min and 30 sec, the hematite specimen started to show evidence of nucleation. The recorded time is an incubation period which has been noted by several other investigators. Thereafter, the morphology changed rapidly from a single crystal to a polycrystal. In Figure 12, electron micrographs reveal the change of morphology of a region before and after 3 min and 40 sec under the reducing condition. A typical diffraction pattern for the central part of the region is shown on Figure 13(a), which is polystalline magnetite. On the other hand, to the right of the region, porous iron coexists with magnetite. It is noted that the porous iron site was the origin of the reduction. The transition of hematite --> magnetite --> iron took place rapidly, so that no record could be obtained. The magnification had to be reduced in order to see the interface of the hematite and magnetite. Figure 14 is the area to the right hand side of Figure 12. The sequence electron micrographs reveals the development of pores which is indicated by arrow. The phenomenon is expected during the transformation from magnetite to iron, since the oxygen atom has to be moved out off the lattice and leave iron atoms behind. The overview of whole reaction zones taken after 14 min and 40 sec is shown on Figure 15, and is a region not previously struck by the electron beam. This semicircularly reaction zones are a typical configuration for the reduction of hematite under these conditions. The reaction started on an edge and extend into the inner region of the specimen. It is worth noting that the precipitates which can be seen as black dots in unreacted region of matrix hematite have not become nucleation sites for the new phases. If the reduction starts from precipitates, the reduction would rather be a type of uniform internal reduction, since magnetite precipitates were distributed over the specimen. However, in this case, the hematite is reduced in a topochemical manner. Figure 16 shows four distinguishable reaction zones and is a electron micrograph taken after E-cell was removed. Specimen is the same one as Figure 12-15 and had been in specimen box over one month. Pure iron doesn't reoxidize but has a weaker diffraction pattern (c.f. Figure 16a and 13b). Figure 16b-16d, all of magnetite diffraction patterns, reveal two types magnetite, i.e. lath magnetite (Figure 16d) and porous magnetite (Figure 16b and 16d). All the diffraction patterns taken were using a 0.5 μm aperture with a center indicated by dark line. The reason for magnetite having two different porosities can be explained in the schematic diagram of the cross-section of the specimen (Figure 17). Overall, the specimen is thinner at the iron rich region. In region II, polycrystalline magnetite is the major component with a high porosity, however, in region III, polycrystalline magnetite coexist with matrix hematite which lead to a low apparent porosity. Region IV and V are lath magnetite and hematite, respectively.

There are three possibilities for not seeing the formation of wustite: (a) wustite is not stable at temperature below 570°C, which is higher than the temperature of this experimental run, i.e. 417°C. From the equilibrium phase diagram of iron oxides and H_2O/H_2, in Figure 3, it is only expected to see the transition of hematite --> magnetite --> iron. Edstrom[8] has observed the same results even at 600°C. (b) wustite did form during the reduction but can not be distinguished due to the similarity of the lattice structure between wustite and magnetite. (c) wustite is an intermediate phase, it transforms into iron and magnetite in a short period.

Swann and Tighe[34], in their ex-situ study of hematite reduction, noted that porous magnetite structure is the product for hematite reduction at the temperature below 650°C and that the lath magnetite morphology for the reduction temperature above 850°C. Hayes and his coworkers[61] observed that after initial lath mangetite growth, the remainder of the transition can take place by the porous growth mechanism. Their observation of the lath magnetite acting as nuclei for porous growth is confirmed by noting that the lath magnetite is an intermediate phase between hematite and porous magnetite in Figure 16.

In regions with magnetite, the morphologykeeps changing as long as the specimen is under a reducing condition. However the final product, iron, forms, no sintering occurs. In Figure 18a and 18b, morphologies are shown of porous iron obtained from reducing hematite with 2 torr pure hydrogen at 417°C for 3 min and 14 min, respectively. It is noted that the large portion of the morphology is unchanged except the area near the marker "X", the retraction of the residual magnetite and the enlargement of pore size can be seen. No sintering evidence can be drawn from this information.

The reduction rate was observed slowing down when the reaction front reached the thicker part of the specimen. The lath magnetite front advanced slowly and the same situation existed for porous magnetite and iron regions. It is interesting to note that the width of lath magnetite is almost the same, about 1 μm. (see Figure 15 and 16) This observation makes unlikely the possibility of the rate controlling step being the transition between lath magnetite and porous magnetite. This can also be confirmed by Figure 19 which shows the morphology of a partially reduced hematite specimen obtained under the same reducing conditions as Figure 12b. The lath magnetite is not found as its transition is rapid.

The change from hematite to either magnetite structure should not be the rate controlling step since magnetite is the dominant phase for a partial reduced specimen. The direct investigations of the results obtained lead to a conclusion that the rate controlling step for hematite reduction by hydrogen is probably the transition from magnetite to iron. The conclusion confirms Rao and Moinpour's[18] observation. They studied the kinetics of reduction of hematite with pure hydrogen at 245 to 482°C, and noted that the rate-controlling step appears to be the magnetite to iron conversion step. On the other hand, the plate-like morphology of the iron region implies that the mechanism of the reduction reaction is the movement of oxygen to the surface of magnetite crystal leaving iron behind.

An effect of the beam on the reduction rate was observed. Hematite reduction occured in the area with the electron beam passing through it or adjacent to it. Kim[85] has investigated the beam effect on the dissociation of chalcocite and magnesite. He exposed a thin specimen of calcocite or magnesite to a convergent beam and found that the area exposured under the beam has a range of 100 to 400°C higher temperature than outer region depending on several parameters, e.g. the thickness of the specimen, the diameter and intensity of the beam, the heat conductivity of the material, and etc.. The selected nucleation phenomenon in this study might be due to the temperature effect. However, this may not be true for area adjacent to the beam but not directly under it. A mathematic method for beam heating evaluation is demonstrated and discussed in Appendix. Another possibility is radiation damage, especially since this research is conducted in a HVEM, or due to contamination on the surface of specimen.

Both effects have been observed by Swann et al. in their studies of the reduction of iron oxides. Another possibility is that the rate was accelerated due to the magnetic field of the microscope. This effect has been studied by Skorski[56], who observed the reaction rate of hematite reduction by hydrogen is proportional to the magnetic field strength. The quantative study of this phenomenon needs strict control over all the possible parameters, e.g. the magnitude of the magnetic lens, the thickness of the specimen etc.. This is beyond the scope of the present investigation.

The regions located far from the electron beam have a slower reaction rate. In Figure 20, magnetite nucleated and grew all over the specimen in a manner of uniform internal reduction.

4.1.2 Reduction with hydrogen/argon gas mixture

The reaction rate of hematite reduced by 10%H_2/90%Ar was found to be much slower than by reducing with pure hydrogen. This was even true at higher hydrogen partial pressures and temperatures. The electron micrograph shown in Figure 21 is the morphology of a hematite specimen reduced with a 40 torr gas mixture at 610°C for 5 min and 20 sec. The original single crystal appearance was destroyed, i.e. the original flat surface has changed to a granular structure. The pair of the stereo micrographs in Figure 22 reveal the crystalline morphology of hematite after 8 minutes reducing period. It is noted that no pores were developed.

The morphology of specimen continuously changed when more hematite was reduced to magnetite. The crystal's size kept growing and strains were induced on the surface. The reduction of hematite to magnetite is quite completely achieved after 10 min duration time at 610°C. A typical morphology of new magnetite phase is shown on Figure 23 a . Two diffraction patterns, 23 c and 23 d , both of magnetite, were taken from the center and the tip of 23 a , respectively. The dark field image in 23b corresponds to 23a with a $\vec{g}$=220.

The reasons for the slower reaction rate in this study will be discussed as follows: (a) High flow rate is required to maintain high pressure in E-cell. The heat is carried away easier from the surface of specimens which may have a much lower intrinsic temperature. (b) Hydrogen diffusivity is lowered by higher total pressure. (c) The surface of specimen may be blocked due to adsorption of argon molecules.

The reaction is under uniform internal reduction, no preferential interaction site was observed. The beam effect is not pronounced under these experimental conditions.

4.1.3 Summary

In situ reduction of single crystal hematite has been carried out in HVEM. Reduction rate and reaction manner are different using pure hydrogen than using 10%H_2/90%Ar gas mixture. Reduction proceeds fast using pure hydrogen as reducing agent and is in a topochemical manner.Five distinguishable reaction zones are revealed and imply that the reaction under the experimental condition is via the following path,

$$\text{Single crystal hematite} \dashrightarrow \text{Lath magnetite} \dashrightarrow \text{Porous magnetite} \dashrightarrow \text{Porous iron}$$

No evidence showing the existence of wustite was obtained. The typical reaction front appear in hemisheric configurations. The rate-controlling step is prabably the conversion between porous magnetite and porous iron. Directional elongated pores form at the interface of lath magnetite and porous magnetite, and spherical pores distribute randomly within the porous magnetite. Reduction proceeds much slower using 10%H_2/90%Ar gas mixture even at higher temperature. The reduction takes place in an internal reaction manner and the product is granular magnetite.

4.2 Magnetite Reduction Studies

Due to the temperature limitation in the E-cell, the magnetite specimen was reduced at temperatures lower than 570°C which is the lowest temperature for the intermediate oxide, wustite, to be formed as a stable phase. It was expected to observe the direct reduction from magnetite to iron via the following reaction,

$$Fe_3O_4 + 4\ H_2 = 3\ Fe + 4\ H_2O \qquad (4.1)$$

Although Edstrom found the existing compounts in his reduced magnetite were only magnetite and iron, his experiment was conducted at the macro-scale. However in this study wustite might be formed as a transition phase, or be a stable phase due to the beam effect, which might produce a high temperature region.

Prior to reduction, magnetite has point defects distributed on the surface, which can be seen on Figure 24a. The dark field image with a $\vec{g}$=220 is shown on Figure 24b. The electron diffraction pattern (Figure 24c) shows that the defects are coherent with matrix. The defects may disappear (Figure 24d) with a small tilting angle, (1.1°).

4.2.1 Reduction with pure H_2

The sequence of change in the morphology of magnetite during the reaction is shown in Figure 25. The magnetite specimen was exposed to 2 torr pure hydrogen at 300°C. After a short incubation period, i.e. about 4 minutes (The data was recorded in the notebook not from photograph,) faceted pits formed first, then iron nucleation occured in the region adjacent to the pits. Iron nucleation and growth took place simulataneously and expanded over the magnetite surface. A comparision of the same area before and after 13 minutes reduction is shown in Figure 26. It is noted that the nucleation site corresponded to the original thinner area of the specimen after sample preparation, e.g. the edge and the region pointed by arrows.

Identification of the pits from the electron diffraction pattern is still magnetite. The bright and dark field image in Figure 27 shows the pits have a close relationship with the parent matrix. The facets of these pits appear to be {111} planes, corresponding to the densest oxygen planar packing in the cubic oxide, magnetite. The schematic illustration in Figure 28 shows the development of this polyhedron from triangle. Presumably if velocity V_1 in <110> direction is faster than V_2 in <100> direction, then the hexagonal configuration is formed. In Figure 29, the assumption can be strengthened by observing the growth of pits from partially reducing specimen. It is noted that the formation of pits occured only after the hot stage was turned on. Whenever the nucleation took place, pits stopped growing. This phenomenon also can be seen in Figure 29. Pits would be swallowed and run over by the iron cluster. There are two criteria to see the pits after reaction (retained pits): (a) If the area of pit is large, much larger than the averaged pore size of the iron cluster, the evidence of pit existence will be observed. (b) If the ratio of the depth of pit (h) to the local thickness of magnetite is high, pit will be left over even if the component has been changed to fine particles of α-iron. The specimen was further reduced at 300°C with a slightly positive pressure of hydrogen for 8 min and 30 sec and the morphology of the retained pits is shown in Figure 30, which can be compared with Figure 27. Both pictures were taken from the same region.

The iron cluster contains not only polycrystalline α-iron, but also magnetite, which is shown in Figure 31. The specimen was reduced at 400°C for a minute using pure hydrogen as reactant. The overall electron diffraction pattern includes a strong spotty ring pattern of α-iron and a weak continuous ring pattern of magnetite. Dark field images were taken from these two distinct rings to show the corresponding phases. Obviously the iron phase is dominant and magnetite phase is surrounding the iron. Some magnetite image also appears in Figure 31c since the objective aperture of the microscope is too large to exclude the rings belonging to magnetite. From the appearance of magnetite ring pattern, it is worth noting that single crystal magnetite disrupts its structure before being reduced to iron. A stereo pair of micrographs in Figure 32 shows that the lighter region is fissure, or pore if it is not on an edge. The magnetite specimen has been exposed to 1 torr hydrogen at 330°C for 7 min. On an edge, the specimen is thinner, transformation from magnetite to iron is easier. (e.g. diffusion path lengths to the surface are shorter.) The disruption of magnetite single crystal might be not necessary, instead, oxygen diffused out the surface of magnetite crystal and left iron behind. The bright and dark field images of the same area as Figure 32 after reducing 14 min more at 330°C is shown in Figure 33. The plate-like iron phase is large enough to give a single crystal pattern of α-iron with a [111] zone axis.

Reduction temperature plays an important role in determination of the pore size of iron product. The iron nuclei formed after 10 seconds reducing with 20 torr hydrogen at 350°C, have a size range from 100 Å to 500 Å. Bright and dark field image of the partially reduced magnetite is shown in Figure 34a and 34b. The sample was heated up to 500°C in vacuum for 2 min to check the coalesence of iron nuclei inside the iron cluster. (Figure 34c and 34d) Not only were iron nuclei enlarged, but also the pores were broadened. Under this circumstance the specimen might have been exposed to a slightly reducing environment, since the hydrogen could be the dominant residual gas in the E-cell. From Figure 34(c) and 34 (d), it is noted that the interface of iron/magnetite was broadened. but the iron nuclei had retreated. This might due to the decreasing total volume of pores. A lower magnetication to view the whole iron nuclei is shown on Figure 35. Figure 35(a) and 35(b) are corresponding to Figure 34(a) and 34(c), respectively, but note that Figure 35 should be rotated 90° clockwise in order to match up the direction. The specimen was reduced again at lower temperature, i.e. 300°C, with the same pressure of hydrogen. The reaction rate was much slower but the pore size was larger. The morphology shown in Figure 36e were taken after 2 minutes, and the growth rate along the radial axis was much slower. Turkdogan etal.[30] found a reverse result on pore size measurment. They reported that the reduced iron has a regular pore structure which becomes finer with decreasing reduction temperature.

Pluschkell and Sarma[65] studied metal oxides reduction by hydrogen hot stage microscopy and observed similar results as this study. They explained the larger star-like pores observed at low reducing temperature being brought about by stresses. At more elevated temperatures recovery processes prevent any cleavage of the metal phase. In this temperature range the void volume produced by reduction is stored only in the micropore system.

A typical star-like pore in product iron is shown on Figure 36(a) which was obtained by reducing magnetite specimen with 2 torr hydrogen at 300°C for 13 min and 5 sec. Figure 36(b) obtained under the same condition is showing an interconnetion of two iron cluster. Morphology of reduced magnetite is not as same as reduced hematite, c.f. Figure 36(a) to Figure 15. The nucleation site of magnetite reduction can be located either a edge or inner region.

4.2.2 Reduction with hydrogen/argon mixtures

As in the hematite study, a slower reaction rate has been obtained using a hydrogen/argon as mixture as reducing agent. But the single crystal magnetite is rather stable than hematite which has a radical morphology change after being exposed to 10% H_2/ 90% Ar mixture for a short period of time.

A magnetite specimen which has been partially reduced in pure hydrogen was chosen as a starting material. Before inducing 10% H_2/ 90% Ar gas mixture into the E-cell, the specimen already has iron clusters. After the specimen exposed to a reducing atmosphere, 10 torr 10% H_2/ 90% Ar at 350°C, reaction took place preferentially on several certain directions. In Figure 37, a sequence change of morphology is revealed. Note that the time inserted is in min. The morphology has a similarity with the faceted pits during the early stage of magnetite reduction. Both morphologys have (1) three pairs of paralled boundaries, (2) angles with a value of 60°, 90°, or 120°. The sequence change of the cross section is drawn in Figure 38. It shows that at t=0, only polystalline iron gathered on one side of the surface. When reaction started, iron nuclei coalesced and reduction happened at the magnetite/iron/hydrogen interface which lower the level of metal surface. The reaction front kept moving toward magnetite that made the boundary of metal/oxide to be steep and clear. The contrast between iron pit and matrix magnetite revealed on the microscope screen was getting stronger implied that the iron pit became deeper. The dislocation might play an important role in this reduction. Figure 39 was taken after 3 hours reduction period; the hexagon-like structures might have been dislocation loops before reduction. Cracks also may become reaction sites which can be seen in a series of electron micrographs in Figure 40. In this case a magnetite specimen was reduced by 50 torr 10% H_2/ 90% Ar at 514°C. Pits formed at about 18 minutes, then elongated to be 'channels'. The channels entended following the dislocation lines which can be seen in Figure 41 (the same run) with time indicated by the inserted numbers. The overall picture along the crack before and after the reaction is shown in Figure 42. Edges also contributed reaction sites to the reduction, e.g. in Figure 43, pits occured on the edge and grew toward the matrix.

4.2.3 Summary

An intensive study of magnetite reduction has been carried out with pure hydrogen and hydrogen/argon gas mixture at 300 to 514°C.

Pits form prior to the nucleation of porous iron when a single crystal magnetite specimen is exposed to pure hydrogen at 350°C. Size and shape of the pits change at the initial period and do not change after iron nucleation occurs. The iron nucleation takes place near or right on the pits. The iron grows isotropicly when the reaction rate is fast. Morphology of the reduced magnetite is in a circular shape and implies that the reaction is not necessary to start on an edge. A pronounced slow reaction rate was observed using hydrogen/argon gas mixture. At a low reducing potential, e.g. conducting the reaction with a gas mixture, or during the incubation period, the reaction proceeds preferentially along certain directions.

4.3 Wustite Reduction Studies

Wustite is not a stable compound, it may decompose to magnetite and iron when the conditions are possible from a thermodynamic point of view. It can exist at temperatures below 570°C as a metastable phase and it is the form of the wustite for this study.

No matter how carefully the specimen is prepared, magnetite is always found embedded inside the wustite matrix which is shown in Figure 44b. Once in a while, magnetite fully developed to have a defined region as shown in Figure 44c. It is noted that the zone axis of magnetite nuclei is the same as the parent wustite, e.g. both have $[\bar{1}12]$ direction.

4.3.1 Behaviour in vaccum

The reason to study the change of wustite microstructure in vaccum is that wustite is unstable at temperature below 570°C, it decomposed to magnetite and iron via following reaction:

$$FeO \dashrightarrow \tfrac{1}{4}\,Fe_3O_4 + \tfrac{1}{4}\,Fe \qquad (4.2)$$

There is no kinetics data available for this reaction. It is quite a complicated system, since the products can be formed through another way by either oxidation, i.e. Fe_3O_4, or reduction, i.e. Fe. Controlling of the environment in reaction cell is very important.

The black stuff on the surface of wustite specimen in Figure 45 is contamination deposited during the sample preparation, however, it can act as an on-site marker. The specimen was heated up to 500°C in vacuum. The morphology change was immediately observed especially on the edge of specimen. Presumably there should be some areas with a magnetite rich phase and some areas with an iron rich phase. A piece of magnetite plate was developed after 18 minutes. After about a half hour, the tiny retangular magnetite nuclei occured and grew, which is shown in Figure 46. During this period, the dimension of the specimen did not vary too much. The nucleation and growth of magnetite went on smoothly. Most of the magnetite nuclei were preferentially growing in one direction. By comparing of Figure 46a and 46b, a conclusion could be drawn that the nucleation and the growth of magnetite are not the simultaneous reactions. No new nuclei were found after growth of the nuclei commenced. After an hour at 500°C, the specimen temperature was brought up to 600°C at which wustite can be a stable phase. It is expected to stop the growth of magnetite. Supprisingly, dissolving of magnetite was observed which is disclosed in Figure 46c.

On the first stage of heating, porous structure was formed, which is shown in Figure 47a. This structure was stable during the second stage of heating. Figure 47b was taken after 49 min at 600°C.

4.3.2 Reduction with pure H_2

Magnetite and wustite reduced under similar conditions yield similar morphologies. In Figure 48, at t=0, the wustite specimen surface showed slight evidence of disproportionation, i.e. three small lumps of magnetite are visible. The specimen was reduced with 10 torr hydrogen at 355°C. Neither incubation period nor faceted pit was observed, the iron nucleation took place immediately at the magnetite lumps and on the edge. The iron nuclei grew and expand over the whole surface area. However, coarsening of pore size also happened; such coarsening was not found in magnetite reduction. (note: The pore size enlargement mentioned before was occured during the annealing period, heating up in vacuum, but not in reducing atmosphere.) Carefully examining the SAD pattern (Figure 49) of the new phase, taken from center of Figure 48, it was found that the dominant compounts were iron and magnetite. The intensity of the rings indicates that there is more iron than magnetite. There are three possible reactions:

(1) wustite disproportionation $4FeO \rightarrow Fe_3O_4+Fe$ (4.3)

(2) wustite reduction $FeO+H_2 \rightarrow Fe+H_2O$ (4.4)

(3) wustite oxidation $3FeO+\frac{1}{2}O_2 \rightarrow Fe_3O_4$ (4.5)

The iron phase can come from either reduction or disproportionation and the magnetite can be produced through either oxidation or disproportion. There is impossible to have both reaction (2) and (3) taking place in the system under this experimental condition. If the disproportion was the only reaction occured then the magnetite should be the major component. Definitely it is not true from the information obtained. Reaction (3) then can ruled out since it contributes more magnetite. Therefore, a combination of reaction (1) and (2) should be the case for the reaction of this study.

A kinetic model can be developed from the information obtained. It is reasonable to assume that the disproportionation and reduction of wustite coupling with the magnetite reduction are the major reactions under this circumstance. The schematic and equations of the system are shown as follows:

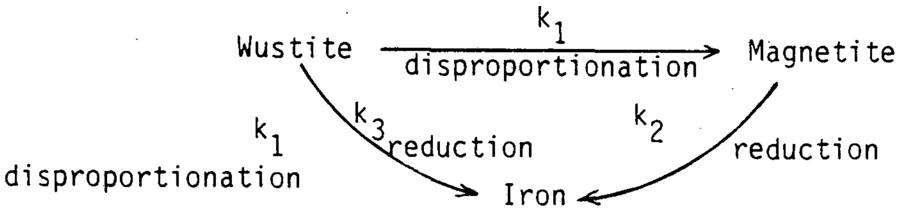

$$FeO \xrightarrow{k_1} \frac{1}{4} Fe_3O_4 + \frac{1}{4} Fe \qquad (4.6)$$

$$Fe_3O_4 + 4\ H_2 \xrightarrow{k_2} 3\ Fe + 4\ H_2O \qquad (4.7)$$

$$FeO + H_2 \xrightarrow{k_3} Fe + H_2O \qquad (4.8)$$

where k_1, k_2, and k_3 are the rate constants of equation 4.6, 4.7 and 4.8, respectively.

Assuming that the reactions are first order, the rate of the mass change for these components is derived as

$$\frac{dM_{FeO}}{dt} = -k_1 M_{FeO} - k_3 M_{FeO} = -(k_1+k_3) M_{FeO} \tag{4.9}$$

$$\frac{dM_{Fe_3O_4}}{dt} = \frac{1}{4} k_1 M_{FeO} - k_2 M_{Fe_3O_4} \tag{4.10}$$

$$\frac{dM_{Fe}}{dt} = \frac{1}{4} k_1 M_{FeO} + 3\, k_2 M_{Fe_3O_4} + k_3 M_{FeO}$$

$$= \left(\frac{1}{4} k_1 + k_3 \right) M_{FeO} + 3\, k_2 M_{Fe_3O_4} \tag{4.11}$$

where M_{FeO}, $M_{Fe_3O_4}$ and M_{Fe} are the amount of wustite, magnetite and iron, respectively.

Integrating Eq. (4.9) gives

$$-\ln \frac{M_{FeO}}{M_0} = (k_1 + k_3)\, t \tag{4.12}$$

where M_0 is the original amount of wustite. Therefore, the amount of wustite M_{FeO} is an exponential function of M_0 which can be shown as

$$M_{FeO} = M_0 \exp\left\{-(k_1+k_3)t\right\} \tag{4.13}$$

Substituting Eq.(4.13) into Eq.(4.10) and integrating it, then get

$$M_{Fe_3O_4} \cdot \exp\{k_2 t\} = \int \frac{1}{4} k_1 M_0 \cdot \exp\{-(k_1+k_3)t\} \cdot \exp\{k_2 t\}\, dt + C$$

$$= \frac{-k_1 M_0}{4(k_1-k_2+k_3)} \cdot \exp\{-(k_1-k_2+k_3)t\} + C \qquad (4.14)$$

Finally,

$$M_{Fe_3O_4} = \frac{-k_1 M_0}{4(k_1-k_2+k_3)} \cdot \exp\{-(k_1+k_3)t\} + C \cdot \exp\{-k_2 t\} \qquad (4.15)$$

Where C is an integral constant.

There is no magnetite at the initial condition, i.e. $M_{Fe_3O_4} = 0$ at $t=0$, therefore, the value of C can be obtained as

$$C = \frac{k_1 M_0}{4(k_1-k_2+k_3)} \qquad (4.16)$$

Then

$$M_{Fe_3O_4} = \frac{-k_1 M_0}{4(k_1-k_2+k_3)} \cdot \left[\exp\{-(k_1+k_3)t\} - \exp\{-k_2 t\}\right] \qquad (4.17)$$

Doing material balance for iron, which is

$$M_0 = M_{FeO} + \frac{1}{3} M_{Fe_3O_4} + M_{Fe} \qquad (4.18)$$

Substituting Eq. (4.13) and (4.17) into Eq. (4.18), the value of M_{Fe} can be shown as follows

$$M_{Fe} = M_0 \left\{ 1 - \left[1 - \frac{k_1}{12(k_1 - k_2 + k_3)} \right] \cdot \exp\left\{-(k_1 + k_3)t\right\} + \frac{k_1}{12(k_1 - k_2 + k_3)} \cdot \exp\left\{-k_2 t\right\} \right\} \tag{4.19}$$

The schematic diagram of M_i vs time is shown as follows

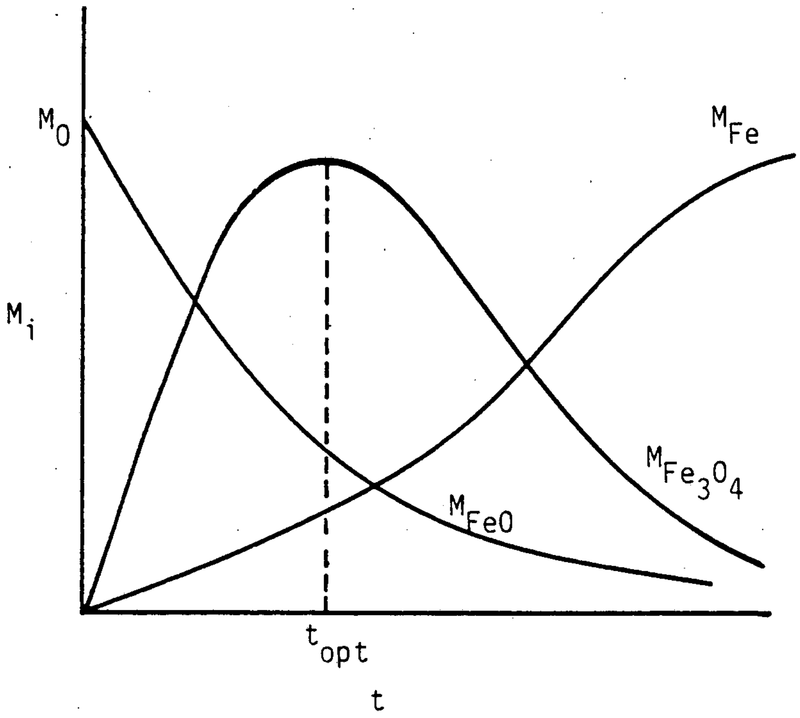

The most amount of magnetite shows up at t_{opt}, when

$$\frac{dM_{Fe_3O_4}}{dt} = 0 = \frac{-k_1M_0}{4(k_1-k_2+k_3)}\left[-(k_1+k_3)\cdot \exp\left\{-(k_1+k_3)t\right\} + k_2\cdot \exp\left\{-k_2t\right\}\right] \quad (4.20)$$

Since the first term in r.h.s. is a constant which is not zero, the second term must be equal to zero.

Then,

$$(k_1+k_3)\cdot \exp\left\{-(k_1+k_3)t\right\} = k_2\cdot \exp\left\{-k_2t\right\}$$

$$\exp\left\{-(k_1-k_2+k_3)t\right\} = \frac{k_2}{k_1+k_3}$$

$$-(k_1-k_2+k_3)t = \ln\frac{k_2}{k_1+k_3} \quad (4.21)$$

Therefore,

$$t_{opt} = \frac{\ln[(k_1+k_3)/k_2]}{k_1-k_2+k_3} \quad (4.22)$$

Case(i) if $k_3 \gg k_1$

$$M_{FeO} \cong M_0\cdot \exp\left\{-k_3t\right\}$$

$M_{Fe_3O_4} \cong 0$, and

$$M_{Fe} \cong M_0\left[1-\exp\left\{-k_3t\right\}\right]$$

Then M_i vs t should appear as

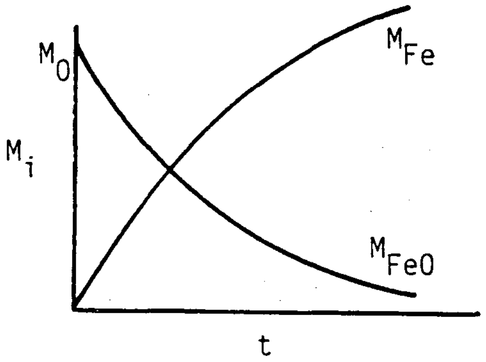

Case (ii) if $k_1 >> k_3$

$$M_{FeO} = M_0 \cdot \exp\{-k_1 t\}$$

$$M_{Fe_3O_4} = \frac{-k_1 M_0}{4(k_1-k_2)} \left[\exp\{-k_1 t\} - \exp\{-k_2 t\}\right]$$

$$M_{Fe} = M_0 \left\{1 - [\ 1 - \frac{k_1}{12(k_1-k_2)}\ ] \cdot \exp\{-k_1 t\}\right.$$

$$\left. + \frac{k_1}{12(k_1-k_2)} \cdot \exp\{-k_2 t\}\right]$$

and the plot is shown as follows,

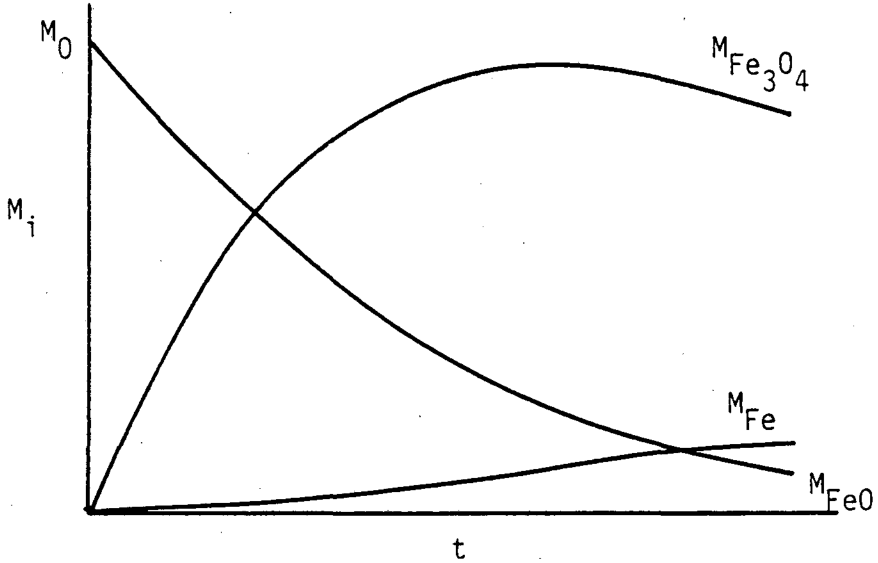

Comparing the kinetics of wustite reduction with pure hydrogen to in vacuum, k_1 greater than k_3 is out of question in this case. Reduction rate is much faster than disproportionation rate. Another method to check in situ is shown on Figure 50. A wustite specimen was reduced partially using 10 torr pure hydrogen at 350°C for 2 min and was re-heated up to 400°C in vacuum for 10 min which is longer than the first stage reducing time. The morphology in Figure 50c can barely see disproportionation at the area pointed by arrows. (c.f. with Figure 45c to see the similarity.) Thereafter, the specimen was reduced under the condition as the first stage for 2 min and its morphology changed to porous iron and magnetite.

Following this model, it is not surprise to see iron, magnetite and wustite coexisting. The electron micrographs in Figure 51 is the other area of the same specimen as before after the first stage reduction. Figure 51 is a bright field image and Figure 51b abd 51c are dark field images corresponding to wustite and iron, respectively.

The structural change was subjected to a low pressure of hydrogen gas. For example, the wustite specimen was reduced using 0.5 torr pure H_2 at 450°C. Figure 52 reveals how the surface morphology changed from a plain to a roughened surface, which has a lots of pits. This was resulted from the disproportionation of wustite. A stereo pair of electron micrographs on Figure 53 reveals the configuration of the pit. Schematic illustration of the formation of pits is shown in Figure 54. Oxygen moved outward to build a lump of magnetite rich region and iron was left behind in the center of the pit. Depending on the kinetic model, both disproportionation and reduction were taking place at the same time as seen in Figure 55. Note that porous iron came in from the left upper corner after 8 minutes. The iron product formed dendritically at the beginning and prolonged to form a porous structure. (Figure 56) The typical product iron under this low pressure condition is shown on Figure 57. The wustite specimen was reduced using ½ torr H_2 at 450°C for 45 seconds.

4.3.3 With hydrogen/argon mixture

The reduction rate is slow using hydrogen/argon as reactant. Instead of reduction, disproportion occured right after a wustite specimen exposed to 50 torr 10% H_2/ 90% Ar at 514°C. In Figure 58, four sequence electron diffraction patterns show that single crystal wustite can epitaxially transform to magnetite then to polycrystal magnetite. The rate of reaction is slow. The porous iron region was found after 2 hour and 25 minute (see Figure 59). The boundaries of the pores are seen to be alignned in certain directions, for example, many pore walls are parallel to the direction indicated by the arrow. This phenomenon is accordant with the other two oxides: preferential reduction is always found under a low reducing potential.

4.3.4 Summary

The reduction of single crystal wustite at temperatures below 570°C occurs in a complex way. Iron can be formed via both disproportion and reduction reactions. A mathematic model to describe the disappearance and appearance of oxides and iron has been presented. At a high reducing potential, the morphology of the reduction products is similar to the case of the reduction of magnetite. On the other hand, disproportion accompanying reduction is observed at a low reducing potential. The results also have shown that (i) on exposure of wustite to vacuum at temperature there is slow disproportionation to iron and magnetite. (ii) on exposure to hydrogen at temperature there is a much more rapid appearance of magnetite and iron and (iii) therefore, disproportionation of wustite is promoted by phenomena occuring during wustite reduction.

CHAPTER 5 CONCLUSIONS

Dynamic experiments in the transmission electron microscope provide an unique technique for study of gas-solid reactions. From the metallurgical point of view, iron oxide reduction by gaseous reactant is of practical importance. However, the exploration of nucleation and growth of iron at atomic level is a relatively new field.

This research looked into three iron oxides and their reduction using pure hydrogen and hydrogen/argon gas mixtures with pressures up to 50 torr at 300 to 610°C. The following conclusions can be drawn from the results of this study:

(1) The reduction rate using hydrogen/argon gas mixtures is at least 2 orders of magnitude slower than when using pure hydrogen. Preferentially reduction was observed only at a low reducing potential, e.g. using gas mixture as reactant, or at the initial stages of reaction.

(2) High pressures and temperatures lead to fast reaction rate when using pure hydrogen. The morphology of product iron grows isotropically for all three oxides.

(3) The reduction of single crystal hematite in pure hydrogen at the temperature below 400°C is via the following path,

Single crystal hematite --> Lath magnetite --> Porous magnetite --> Porous iron

The reaction fronts appear in hemisheric configurations and the reduction proceeds in a topochemical manner. Directional elongated pores form at the interface of lath magnetite and porous magnetite, and spherical pores distribute randomly within the porus magnetite.

(4) Destruction of surface structure happens at first, when magnetite is reduced by pure hydrogen. Iron nucleation occurs at a thinner region and grows isotropically to form a circular shape.

(5) The reduction of single crystal wustite at the temperature below 570°C occurs in a complex manner. Iron was formed via both disproportion and reduction reactions. A mathematic model was derived based on three assumed first order reactions.

(6) Dislocation, crack, edge and thin region provide active interaction sites for the reduction.

ACKNOWLEDGEMENTS

The author wishes to express his thanks to Prof. J. W. Evans for his guidance and support during this study. Deep appreciation is extended to Prof. L. Brewer and Prof. R. Gronsky for their providing helpful discussion and reviewing this manuscript during the holiday. Appreciation is also due to Prof. D. W. Fuerstenau and Dr. E. Peters for their encouragement and assistance in preparation of the qualifying examination.

The kindness of the University of Chicago and Purdue University for providing the single crystal iron oxides used in this study is highly appreciated.

The D. N. Vedensky Scholarship is gratefully acknowledged for his financial support.

Finally, the author would like to thank his family members for their exceptional patience and support, which enabled this work to be carried to completion.

This work was supported by the Division of Materials Science, Office of Basic Energy Science of the U. S. Department of Energy under Contact DE-AC03-76-SF00098.

APPENDIX

Beam heating calculation

A mathematic method for beam heating evaluation is demonstrated and discussed as follows.

Let C = beam current

E = accelerating voltage

R = radius of beam spot on sample

ϕ = fraction of beam absorbed

Assume worst possible case: electron absorption occurs on surface of specimen, negligible conduction into specimen, negligible convection into gas, radiation into cell environment at furnace temperature.

Heat generation rate = ϕCE watts

= heat loss rate by radiation = $\pi R^2 \varepsilon \sigma (T_{surf}^4 - T_{furn}^4)$

where ε = emissivity of surface of specimen (guess 0.5)

σ = Stefan-Boltzmann constant

T_{surf} = surface temperature (to be calculated)

T_{furn} = furnace temperature

Typical values of the parameters are as follows,

$C = 15\mu A = 0.000015$ amp

$E = 500$ kV $= 500000$ volts

$\varepsilon = 0.5$

$\sigma = 1.355 \times 10^{-12}$ cal/sec/cm^2/°K^4

T_{surf} can be calculated for various values of R, ϕ and T_{furn}. The result is shown in following tables.

(i) R = 1 mm

	ϕ = 0.5%	0.1%	0.05%	0.01%
T_{furn}=300	T_{surf}=809	T_{surf}=551	T_{surf}=473	T_{surf}=358
(°K) 400	(°K) 817	575	510	429
500	834	618	568	516
600	861	680	643	609
700	901	754	728	706
800	954	838	819	804
900	1018	927	914	902
1000	1091	1020	1010	1002

(ii) R = 2 mm

	ϕ = 0.5%	0.1%	0.05%	0.01%
T_{furn}=300	T_{surf}=580	T_{surf}=413	T_{surf}=369	T_{surf}=317
400	601	463	436	407
500	640	537	519	504
600	696	623	611	602
700	766	714	707	701
800	847	810	805	801
900	934	907	903	900
1000	1025	1005	1002	1000

From the calculated results, it is noted that the radius of beam spot on sample plays an important role to the heating effect. In practice, a focus beam on a sample should be avoided.

REFERENCE

1. J. Szekely, J. W. Evans and H. Y. Sohn, Gas-Solid Reactions, Academic Press, New York, 1976.
2. R. L. Stephenson, in Direct Reduced Iron, R. L. Stephenson (ed.), AIME, Warrendale, PA, 1980, p.160.
3. T. Rosenqvist, Principles of Extractive Metallurgy, 2nd ed., McGraw-Hill, New York, 1983, p.239.
4. H. E. McGannon, ed., The Making, Shaping and Treating of Steel, 9th ed., USS, Herbick and Held, Pittsburgh, 1971, p.403.
5. T. E. Dancy, Met. Trans., 8B, 201 (1977).
6. H. W. Paxton, Met. Trans., 10B, 461 (1979).
7. G. Poferl, K. Primas and S. Zeller, I & SM, Mar. 1981, p.25.
8. J. O. Edstrom, J. Iron & Steel Inst., 175, 289 (1953).
9. J. O. Edstrom and G. Bitsianes, AIME Trans., 203, 760 (1955).
10. H. K. Kohl and H. J. Engell, Arch. Wiss., 34, 411 (1963).
11. H. Brill-Edwards, B. L. Daniell and R. L. Samuel, J. Iron & Steel Inst., 203, 361 (1965).
12. P. K. Strangway and H. U. Ross, Trans. AIME, 242, 1981 (1968).
13. R. G. Olsson and W. M. Mckewan, Met. Trans., 1, 1507 (1970).
14. W. Pluschkell and H. Yoshikoshi, Arch. Eisenhuttenw., 41, 715 (1970).
15. Y. K. Rao, Met. Trans., 10B, 243 (1979).
16. A. V. Bradshaw and A. G. Matyas, Met. Trans., 7B, 81 (1976).
17. P. C. Hayes and P. Grieveson, Met. Trans., 12B, 579 (1981).
18. A. Unal and A. V. Bradshaw, Met. Trans., 14B, 743 (1983).
19. N. J. Themelis and W. H. Gauvin, AIChE J., 8, 437 (1962).
20. E. T. Turkdogan and J. V. Vinters, Met. Trans., 2, 3175 (1971).
21. E. T. Turkdogan and J. V. Vinters, Met. Trans., 3, 1561 (1972).
22. T. G. Cox and F. R. Sale, Ironmaking and Steelmaking, No.4, 234 (1974).

23. U. Finnstrom, in Electron Microscopy 1974, Vol.I, Australian Academy of Science, Canberra, 1974, p.164.

24. U. Finnstrom, Scand. J. Met., 5, 134 (1976).

25. J. Szekely and C. Karatas, Met. Trans., 9B, 147 (1978).

26. S. K. El-Rahaiby and Y. K. Rao, Met. Trans., 10B, 257 (1979).

27. D. H. St. John and P. C. Hayes, Met. Trans., 13B, 117 (1982).

28. M. Moukassi, P. Steinmetz, B. Dupre and C. Gleitzer, Met. Trans., 14B, 125 (1983).

29. R. D. Doherty, K. M. Hutchings, J. D. Smith and S. Yoruk, Met. Trans., 16B, (1985).

30. M. Moukassi, M. Gougeon, P. Steinmetz, B. Dupre and C. Gleitzer, Met. Trans., 15B, 383 (1984).

31. Y. Suzuki, M. Yamamoto, T. Kotanigawa and K. Nishida, Met. Trans., 12B, 691 (1981).

32. Y. K. Rao and M. Moinpour, Met. Trans., 14B, 711 (1983).

33. M. M. Al-Kahtany and Y. K. Rao, Ironmaking & Steelmaking, 7, 49 (1980).

34. P. R. Swann and N. J. Tighe, Met. Trans., 8B, 479 (1977).

35. J. R. Porter and P. R. Swann, Ironmaking & Steelmaking, 5, 300 (1977).

36. J. R. Porter and L. C. DeJonghe, Met. Trans., 12B, 299 (1981).

37. L. S. Darken and R. W. Gurry, J. Am. Chem. Soc., 68, 798 (1946).

38. J. M. Larrain and H. H. Kellogg, in Calculation of Phase Diagrams and Thermochemistry of Alloy Phases, Y. A. Chang and J. F. Smith (eds.), AIME, Warrendale, 1979, p.130.

39. R. P. Goel, H. H. Kellogg and J. Larrain, Met. Trans., 11B, 107 (1980).

40. L. Bogdandy and H. J. Engell, The Reduction of Iron Ores, Springer-Verlag, Berlin, 1971.

41. E. R. Jette and F. Foote, J. Chem. Phys., 1, 29 (1933).

42. F. Koch and J. B. Cohen, Acta Cryst., B25, 275 (1969).

43. S. Iijima, in Thirty-Second Annual EMSA Meeting, 1974, p.352.

44. S. Nagakura, T. Ishiguro and Y. Nakamura, in the Proc. of the Seventh Inter. Conf. on HVEM, Berkeley, 1983, p.59.

45. W. M. Stobbs, D. J. Smith and S. B. Newcomb, in The Proc. of the Seventh Inter. Conf. on HVEM, Berkeley, 1983, p.63.

46. M. Tokuda, H. Yoshikoshi and M. Ohtani, Trans. ISIJ, 13, 350 (1973).

47. J. W. Evans and C. H. Koo, in Rate Processes in Extractive Metallurgy, M. E. Wadsworth and H. Y. Sohn (ed.), Plenum Press, New York, 1979.

48. L. von Bogdandy and W. Janke, Z. Electrochem. Ber. Runsenges. Phys. Chem., 61, 1146 (1957).

49. J. M. Quets, M. E. Wadsworth and J. R. Lewis, Trans. TMS-AIME, 218, 545 (1960).

50. W. K. Lu and G. Bitsianes, Can. Met. Q., 7, 3 (1968).

51. R. H. Spitzer, F. S. Manning and W. O. Philbrook, Trans. TMS-AIME, 236, 726 (1966).

52. B. B. L. Seth and H. U. Ross, Trans. Met. Soc. AIME, 233, 180 (1965).

53. J. Feinman and T. D. Drexler, AIChE J., 7, 584 (1961).

54. S. K. El-Rahaiby and Y. K. Rao, Trans. ISIJ, 20, 287 (1980).

55. C. H. Koo, Ph.D. Dissertation, U. C. Berkeley, 1977.

56. R. Skorski, Nature Phys. Sci., 240, 15 (1972).

57. I. Svare, Nature Phys. Sci., 244, 78 (1973).

58. C. T. Peters, Nature Phys. Sci., 244, 79 (1973).

59. M. W. Rowe, S. M. Lake and R. Fanick, Nature, 266, 612 (1977).

60. E. T. Turkdogan, R. G. Olsson and J. V. Vinters, Met. Trans., 2, 3189 (1971).

61. P. Baguley, D. H. St. John and P. C. Hayes, Met. Trans., 14B, 513 (1983).

62. J. I. Goldstein and H. Yakowitz (eds.), Practical Scanning Electron Microscopy, Plenum Press, New York, 1975.

63. J. A. Little, J. W. Evans and K. H. Westmacott, Met. Trans., 11B, 519 (1980).

64. D. J. Coates, J. W. Evans and K. H. Westmacott, LBL-13704 (1982).

65. W. Pluschkell and B. V. S. Sarma, Arch. Eisenhuttenwes., 45, 23 (1974).

66. R. A. Rapp, Met. Trans., 15A, 765 (1984).

67. R. T. K. Baker and P. S. Harris, J. Phys. E., 5, 793 (1972).

68. E. P. Butler and K. F. Hale, Dynamic Experiments in the Electron Microscope, (Practical methods in electron microscopy: V.9), Elsevier/North-Holland, New York, 1981.

69. H. M. Flower, J. Microscopy, 97, 171 (1973).

70. D. F. Parsons, V. R. Matricardi, R. C. Moretz and J. N. Turner, in Advances in Biological and Medical Physics,Vol.15, J. H. Lawrence and J. W. Gofman (ed.), Academic Press, New York, 1974, p.161.

71. D. L. Allinson, in Principles and Techniques in Electron Microscopy, Biological Applications, Vol.5, M. A. Hayat (ed.), Van Nostrand Reinhold, New York, 1975, p.52.

72. P. R. Swann and N. J. Tighe, Jernkont. Ann., 155, 497 (1971).

73. M. E. Hall, M.S. Thesis, U. C. Berkeley, 1985.

74. J. S. Bates and M. J. Goringe, in Electron Microscopy and Analysis, (inst. Phys. Conf. Ser. 52), 1979, p.321.

75. W. Thoni, P. L. Gai and P. B. Hirsch, Phil. Mag., 35, 781 (1977).

76. P. L. Gai and M. J. Goringe, Kristall und Technik, 14, 1385 (1979).

77. P. L. Gai, C. J. Humphreys, A. E. Webb, D. R. Pike and J. C. J. Bart, in Electron Microscopy and Analysis, (Inst. Phys. Conf. Ser. 52), 1979, p.317.

78. T. Gabor and J. M. Blocher, J. Vac. Sci. Technol., 6, 815 (1969).

79. H. Hashimoto, S. Urai, H. Yotsumoto and J. Sawamori, in Proc. 7th Int. Congr. Electron Microscopy, Grenoble, 2, 1970, p.399.

80. P. R. Swann, in Electron Microscopy and Structure of Materials, G. Thomas, R. Fulrath and R. M. Fisher (eds.), U. C. Berkeley, 1972, p.878.

81. H. R. Harrison and R. Aragon, Mat. Res. Bull., 13, 1097 (1978).

82. H. R. Harrison, R. Aragon and C. J. Sandberg, Mat. Res. BULL., 15, 571 (1980).

83. G. Thomas and M. J. Goringe, in Transmission Electron Microscopy of Materials, John Wiley & Sons, New York, 1979, p.24.

84. J. M. Quets, M. E. Wadsworth and J. R. Lewis, Trans. TMS-AIME, 221, 1186 (1961).

85. M. G. Kim, private communication, U. C. Berkeley.

Table 1 Properties of iron and its oxides

	Fe	FeO	Fe_3O_4	Fe_2O_3
Curie-point (°C)	769	---	627	777
Melting point (°C)	1536	1377	1597	---
Density (gm/cm^3)	7.87	5.70	5.18	5.24
Crystal structure	bcc	cubic	cubic	rhombohedral
Lattice parameter a_o (Å)	2.86	4.307	8.396	5.4228
	---	---	---	55°16'

Table 2 The reactions of the reduction of iron oxides by hydrogen

Reaction	ΔH°_{298} (cal/mole)	ΔG°_T (cal/mole)
$3Fe_2O_3 + H_2 = 2Fe_3O_4 + H_2O$	-2800	720 - 20.52 T
$Fe_3O_4 + H_2 = 3FeO + H_2O$	+18500	15720 - 16.80 T
$FeO + H_2 = Fe + H_2O$	+5700	3150 - 1.85 T
$\frac{1}{4}Fe_3O_4 + H_2 = \frac{3}{4}Fe + H_2O$	+8900	6292 - 5.59 T

Note: The values of ΔH°_{298} and ΔG°_T are from Ref. 2.

Table 3 Characteristics of the E-cell designed by Swann and Tighe

Maximum operating pressure	760 torr
Aperture size	100 μm
Aperture spacing	515 mm
Temperature capability	up to 1000°C
Tilt	single ± 20°

Table 4 Data of the gas mixtures

	Type	Grad	Supplier
(1)	H_2	$H_2 > 99.99\%$	Matheson
(2)	5% H_2/95% Ar	Ar > 99.98% & $H_2 > 99.99\%$	Pacific Oxygen
(3)	10% H_2/90% Ar	"	"
(4)	20% H_2/80% Ar	"	"

FIGURE CAPTIONS

Figure 1. Phase diagram for the iron-oxide system illustrating non-stoichiometric nature of compounds. From Ref.37.

Figure 2. Ellingham diagram for oxides of interest in iron oxide reduction.

Figure 3. Equilibrium gas compositions versus temperature diagram for the iron-hydrogen-oxygen system. From Ref.40.

Figure 4. Schematic diagram of 'environmental cell'. Note that the electron beam passes through four 100μm apertures.

Figure 5. Partial pressure of constituent gases inside pure hydrogen (a) and 10%H_2/90%Ar gas mixture (b) cylinders as recorded by a mass spectrometer.

Figure 6. Schematic diagram of specimen hot stage.

Figure 7. Diversity of temperatures between the furnace and the specimen. A higher heating temperature has a larger variation.

Figure 8. Temperature-heater current calibration curves for the hot stage depicted in Figure 6 operating in the E-cell of Figure 4, under various gaseous environments.

Figure 9. Schematic diagram of experimental set-up. The flow meter was disconnected when the flowrate-pressure calibration has been accomplished.

Figure 10. Flowrate-pressure calibration curve for 10%H_2/90%Ar gas mixture passing through the E-cell at 25°C.

Figure 11. A distribution of magnetite precipitate on the surface of hematite specimen before reduction. The inserted electron diffraction pattern showing a group of magnetite rings overlapping a hematite single crystal pattern.

Figure 12. Electron micrographys of hematite specimen before (a) and after (b) reducing in 2 torr pure hydrogen at 387°C for 3 min and 40 sec. The product phases include porous iron (right), polycrystalline magnetite (center) and pores (left).

Figure 13. Typical electron diffraction pattern for (a) the center part of the region in Figure 12 showing that only polycrystalline magnetite exists, and (b) to the right of the region revealing that porous iron coexists with polycrystalline magnetite.

Figure 14. Sequence electron micrographs revealing the development of pores during hematite reduction by 2 torr pure hydrogen at 387°C. The numbers inserted are the reducing time in second.

Figure 15. Typical configuration of reaction zones for hematite reduction using pure hydrogen. The specimen was reduced by 2 torr H_2 at 387°C for 14 min and 40 sec.

Figure 16. Selected area diffraction patterns from diffrerent reaction zones. Corresponding structures are porous iron (a), polycrystalline magnetite (b) and (c), and lath magnetite (d). The hematite specimen was reduced by 2 torr pure H_2 at 387°C for 14 min and 40 sec and stored in a non-sealed specimen box over one month after reduction.

Figure 17. Schematic diagram of the cross-section of the specimen illustrating five different structures corresponding to Figure 16.

Figure 18. Electron micrographs of porous iron obtained from reducing hematite with 2 torr pure hydrogen at 417°C for 3 min (a) and 14 min (b). Note that the large portion of the morphology is unchanged except the area near the marker 'X', the retraction of the residual magnetite and the enlargement of pore size can be seen.

Figure 19. Morphology of a partially reduced hematite apecimen obtained under the same reducing conditions as Figure 12(b). The lath magnetite is not found as its transition is rapid.

Figure 20. Sequence of electron micrographs showing magnetite nucleation and growth on the hematite specimen surface at a location without exposing to the electron beam except taking pholographys. The specimen was reduced by 5 torr pure hydrogen at 530°C for 10 (a), 16 (b) and 22 (c) minutes.

Figure 21. Electron micrograph of the morphology of a hematite specimen reduced by 40 torr 10%H_2/90%Ar gas mixture at 610°C for 5 min and 20 sec. The original flat surface has changed to a granular structure.

Figure 22. Stereo pair of electron micrographs revealing the crystalline morphology of hematite after 8 min reducing period under the same condition as Figure 21. Note that no pores were developed.

Figure 23. Bright (a) and dark (b) field images of magnetite product after 10 min duration time under the same reducing condition as above. Diffraction patterns of (c) and (d) corresponding to $[\bar{1}22]$ and $[\bar{1}11]$ zone axis of magnetite single crystal patterns were taken from the center and the tip of (a), respectively.

Figure 24. Bright (a) and dark (b) field images of point defects on the surface of magnetite specimen prior to reduction. Electron diffraction pattern (c) shows that the defects are coherent with matrix. A small tilting angle, (1.1°), can reduce the contrast of the defect image.

Figure 25. Sequence electron micrographs showing the proceeding of the reduction of magnetite. The specimen was reduced by 2 torr pure hydrogen at 300°C. Numbers inserted are the reducing time in second. It took about 4 minutes to start a visiable disconstruction of oxide surface. Iron nucleated right at the facted pits on the surface of specimen and then the iron nuclei grew isotropically. Note that facted pits stopped forming after iron nuclei appeared and the iron nuclei didn't occur sintering.

Figure 26. Overview of the region of Figure 25 before (a) and after (b) reduction. The arrows indicating the thinner region of the specimen, which might be the favor site for nucleation of iron phase.

Figure 27. Bright and dark field images of facted pits showing a close relationship between the pits and the parent magnetite matrix.

Figure 28. Schematic diagram illustrating the development of the facted pit. The facted appear to be $\{111\}$ planes and their hexagonal configuration formed due to the different reducing velocities between $\langle 110 \rangle$ and $\langle 100 \rangle$ directions.

Figure 29. Electron micrographs showing the development of faceted pits on partially reduced magnetite. The specimen was brought back to room temperature after the first stage reduction by 2 torr pure hydrogen at 300°C for 14 min, then was reduced again at the same temperature for 2 (a) and 3 (b) minutes.

Figure 30. Bright and dark field images of retained pits.

Figure 31. (a) Bright field image of porous iron formed in reducing magnetite with 10 torr pure hydrogen at 400°C for 1 min. (c) and (d) are corresponding dark field images from A and B reflections indicated in the electron diffraction pattern (b). (c) reveals iron clusters and (d) reveals residual magnetite.

Figure 32. Stereo pair of electron micrographs revealing fissures and pores on the reduced magnetite surface. The specimen has been exposed to 1 torr hydrogen at 330°C for 7 min.

Figure 33. Bright and dark field images of the same area as on Figure 32 after reducing 14 min more showing a plate-like iron product.

Figure 34. (a) Bright and (b) dark field images of porous iron formed by reducing a magnetite specimen in 20 torr pure hydrogen at 350°C for 10 seconds. The iron nuclei were sintered by heating the partially reduced specimen up to 500°C for 2 min in vacuum and their bright and dark field images are shown in (c) and (d), respectively. The same specimen was further reduced at lower temperature, i.e. 305°C, for 2 min with 20 torr pure hydrogen and its bright field image (d) reveals that the size of either iron nuclei or pore is larger than the size of (a).

Figure 35. Lower magnefication micrograph viewing the whole iron nuclei which was shown on Figure 34. Bright field images of (a) and (b) are corresponding to Figure 34(a) and 34(c), respectively.

Figure 36. (a) Typical star-like pores in product iron. (b) Pores formed in one iron cluster only when two iron nuclei grow closely. The magnetite specimen was reduced by 2 torr hydrogen at 300°C for 13 min and 5 sec.

Figure 37. Reduction occurs on several preferential directions with a low reducing potential gas mixture, $10\%H_2/90\%Ar$. The morphology shown in t=0 is an iron cluster which was pregrown isotropically in a pure hydrogen atmosphere. The partially reduced magnetite then was exposed to 10 torr $10\%H_2/90\%Ar$ at 350°C. The morphology of iron cluster changes during reaction. The number inserted is the reducing time in minute.

Figure 38. Schematic illustrating the development of iron cluster under low reducing potential.

Figure 39. Dislocation loops provide the interaction sites for reduction under low reducing potential. The magnetite specimen was reduced at 350°C for 3 hr and 12 min using 10 torr $10\%H_2/90\%Ar$.

Figure 40. Crack provides the interaction site for reduction under low reducing potential. The magnetite specimen was reduced at 514°C using 50 torr $10\%H_2/90\%Ar$. The numbers inserted are the reducing time in minute.

Figure 41. Channels growing along the dislocation lines. The reaction under the same condition as Figure 40.

Figure 42. Overall picture along the crack before (a) and after (b) the reaction. The reaction was stopped after 114 minutes.

Figure 43. Edge contributes reaction site to the reduction. Pits occured on the edge and grew toward the matrix. The magnetite specimen was reduced using 50 torr 10%H_2/90%Ar at 514°C for 59(a),88 (b), 107(c) and 114(d) minutes.

Figure 44. Magnetite is embedded inside wustite matrix (b) and occasionally is found to have a clear colony (to the right of (a)). The diffraction pattern (c) shows epitaxial growth of magnetite cluster in the matrix.

Figure 45. Transformation of wustite at 500°C in vacuum. The numbers inserted are the duration time in minute.

Figure 46. (a) Retangular magnetite nuclei occured after heating the wustite in vacuum at 500°C for 40 minutes. (b) The magnetite nuclei grew preferentially in one direction. Note that the nucleation and the growth of magnetite are not simultaneous reactions. (The electron micrograph was taken after 56 min.) (c) The magnetite nuclei were dissolved back into matrix after the heating temperature was brought up to 600°C for 36 minutes.

Figure 47. (a) Porous structure was developed after heating a wustite specimen at 500°C in vacuum for an hour, and (b) this structure was stable during the second stage of heating at 600°C.

Figure 48. Sequence electron micrographs showing the reduction of wustite using 10 torr pure hydrogen at 350°C for the time inserted in minute. Morphological change is simular to that of magnetite reduction, however, there is no incubation period on facted surface observed.

Figure 49. Typical diffraction pattern taken from iron nuclei showing that only iron and magnetite coexisting.

Figure 50. (a) Magnetite lump existing in a wustite specimen before reduction which became a nucleation site for iron formation after exposing to 10 torr pure hydrogen at 350°C for 2 min. (see (b)). (c) The specimen was heating at 400°C without hydrogen for 10 min. The iron nuclei didn't grow but a disproportionation occured at iron-wustite boundaries which are pointed by arrows. (d) The specimen was reduced under the condition as the first stage for 2 min and its morphology changed to porous iron and magnetite.

Figure 51. (a) Bright field image of a partially reduced wustite. Dark field images of (b) and (c) are corresponded to FeO and Fe, respectively.

Figure 52. Sequence electron micrographs showing the structural changes of a wusitite specimen under a low reducing potential. The surface morphology changed from a plain to a roughened surface, which has a lots of pits. The specimen was reduced using 0.5 torr pure hydrogen at 450°C. The numbers inserted are the reducing time in seconds.

Figure 53. Stereo pair of electron micrographs revealing the configuration of the pits.

Figure 54. Schematic illustrating the formation on pit. Oxygen moves outward to build a lump of magnetite rich region and iron is left behind in the center of the pit.

Figure 55. Electron micrographs of wustite reduction following Figure 52. Disproportionation and reduction occured simultaneously.

Figure 56. Dentritic iron product formed at first and grew to form a porous structure. The number inserted is the reducing time in seconds.

Figure 57. Typical dentritic iron phase in wustite reduction under a moderate reducing potential atmosphere, e.g. 0.1 torr pure hydrogen at 450°C for 5 min and 45 sec in this case.

Figure 58. Electron diffraction patterns showing the transformation of single crystal wustite -> epitaxial crystal magnetite -> polycrystalline magnetite. The specimen was reduced using 50 torr 10%H_2/90%Ar at 514°C for 0(a), 14(b), 30(c) and 160 (d) minutes, respectively.

Figure 59. Porous iron formed in a wustite specimen after reducing at 373°C for 105 min using 5%H_2/90%Ar.

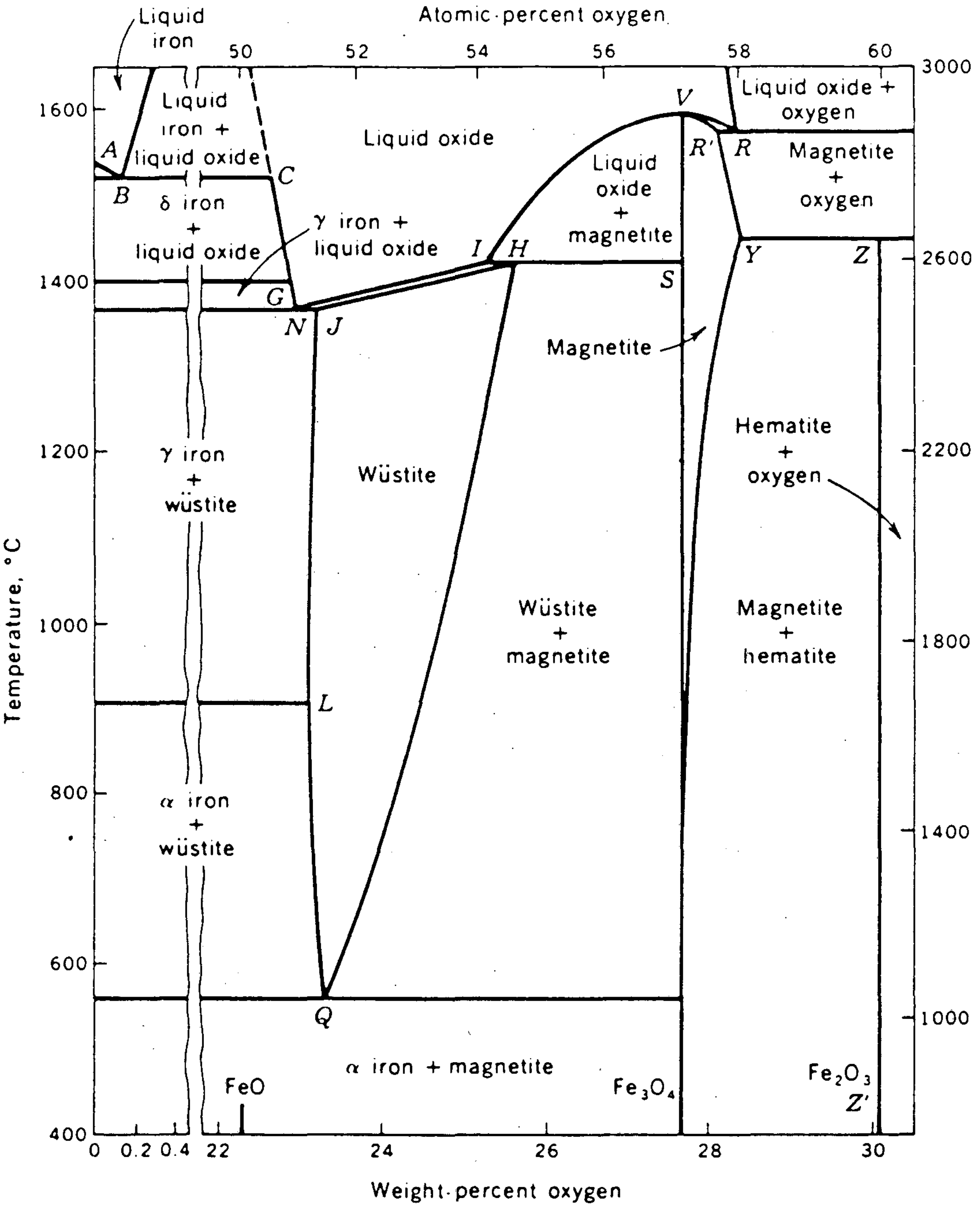

Figure 1.

XBL 8412-5448

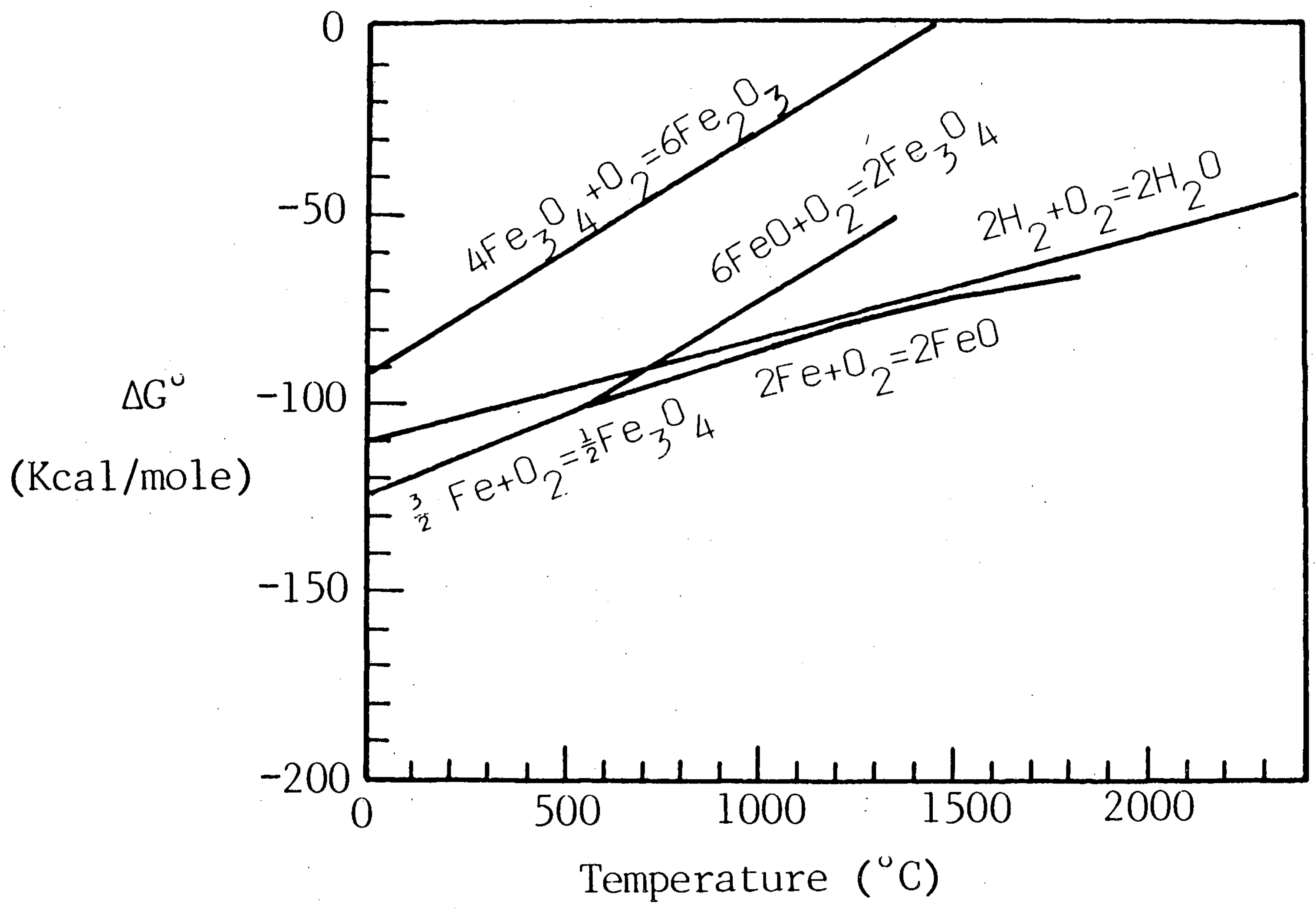

XBL 8412-5446

Figure 2.

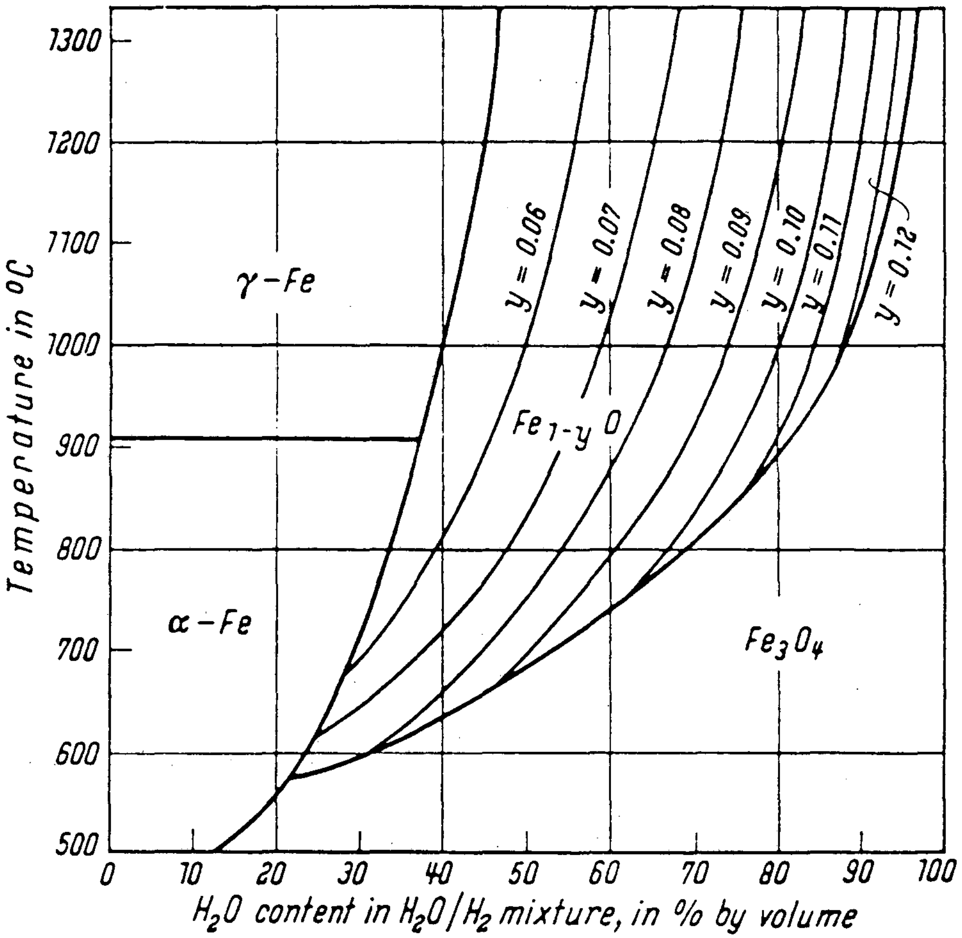

XBL 8412-5447

Figure 3.

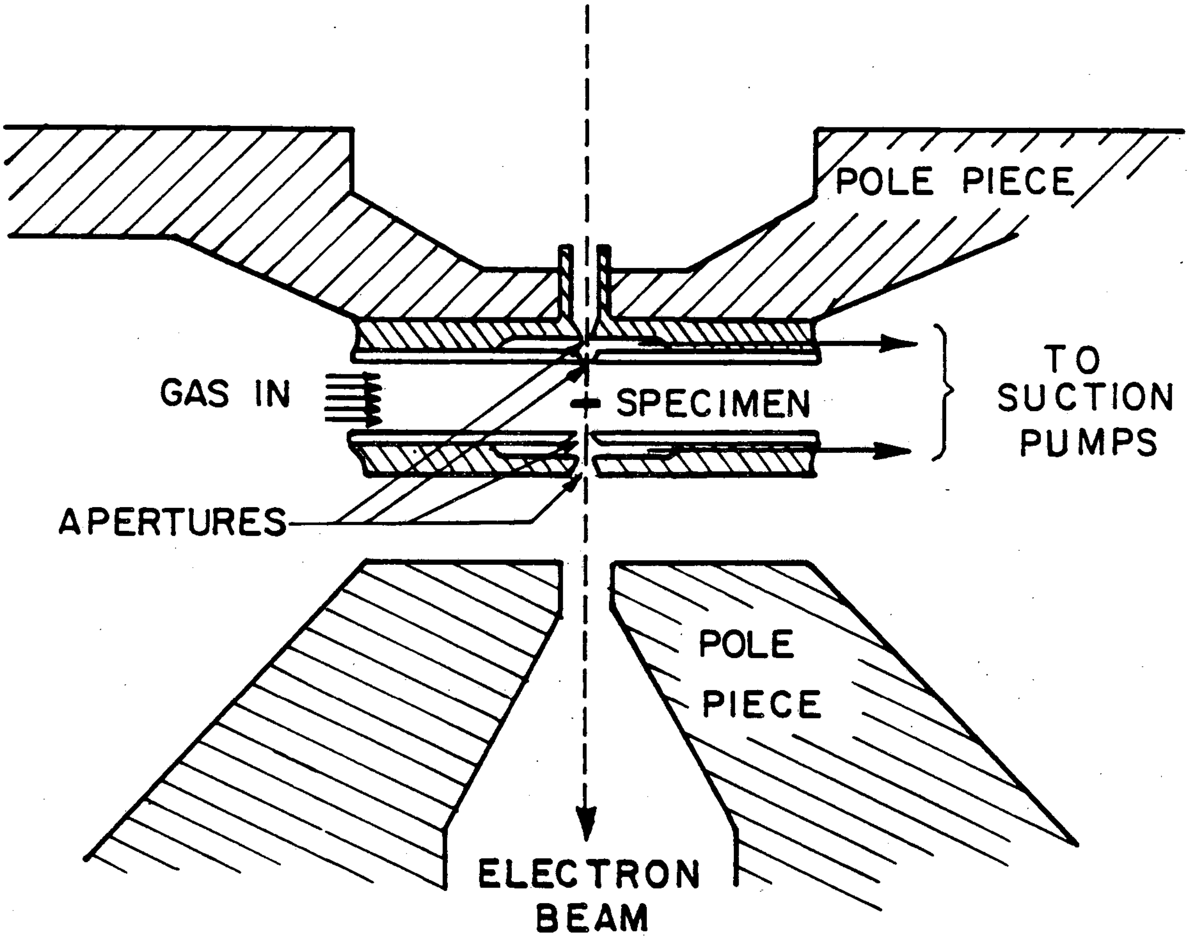

XBL 791-5538

Figure 4.

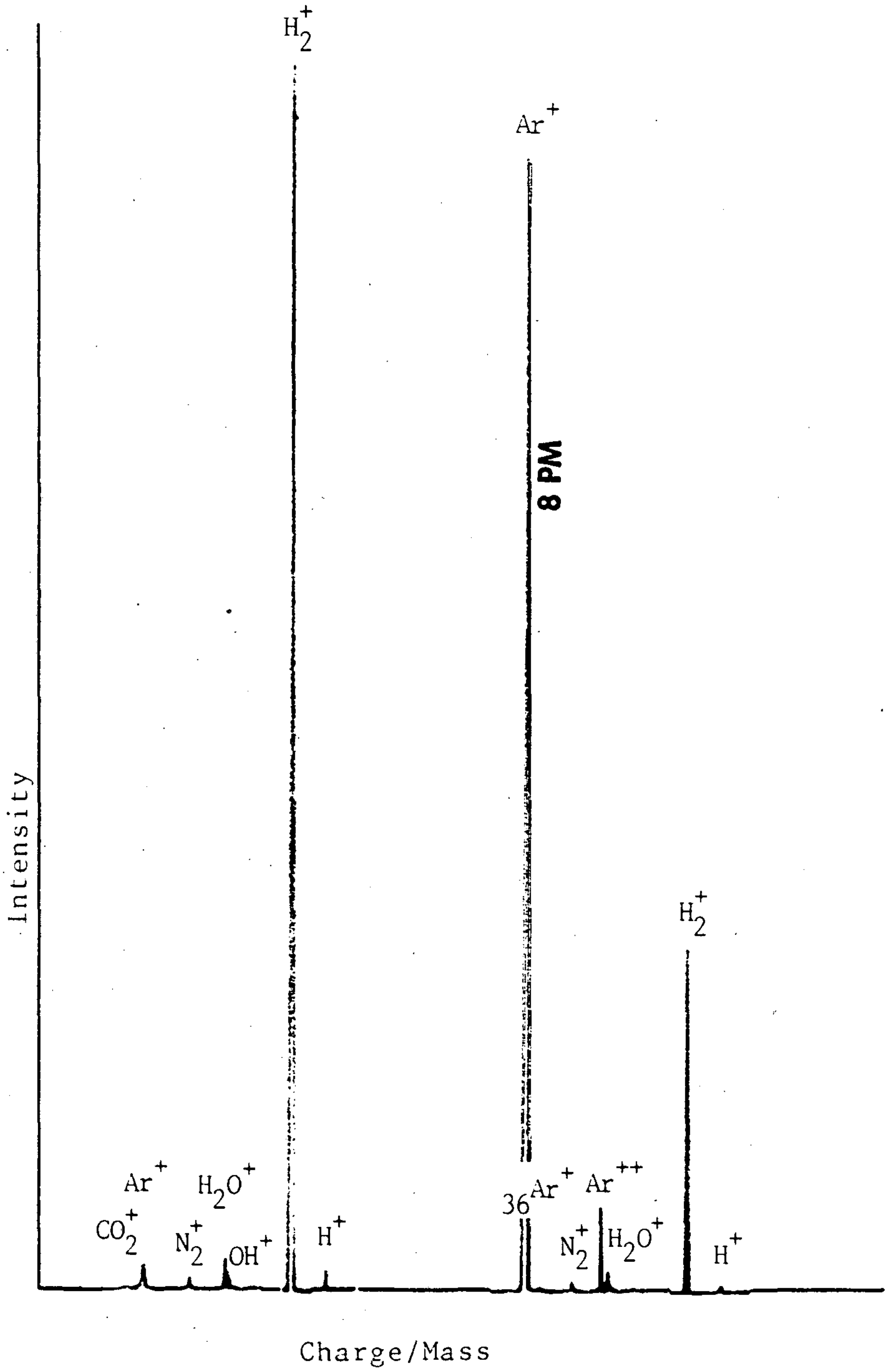

(a)
pure H_2 cylinder

(b)
10%H_2/90%Ar cylinger

XBL 8412-5453

Figure 5.

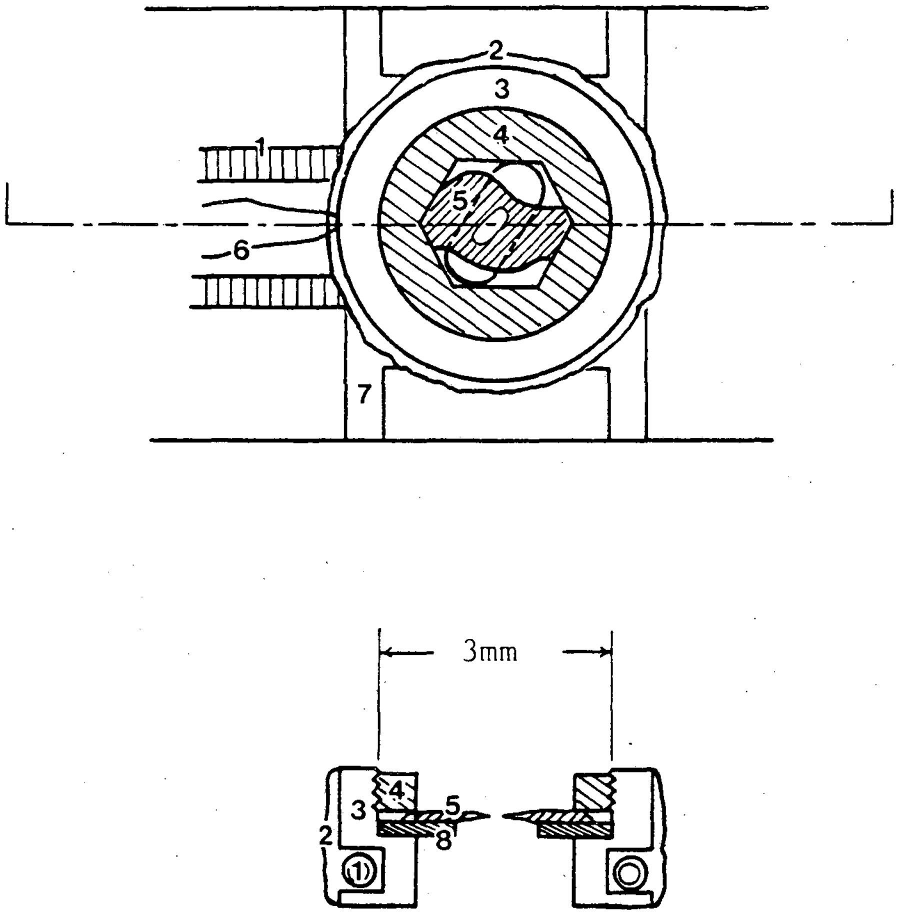

1. heating wire
2. insulating ceramic
3. furnace
4. screw
5. specimen
6. thermocouple
7. support
8. nickel grid

XBL 8412-5452

Figure 6.

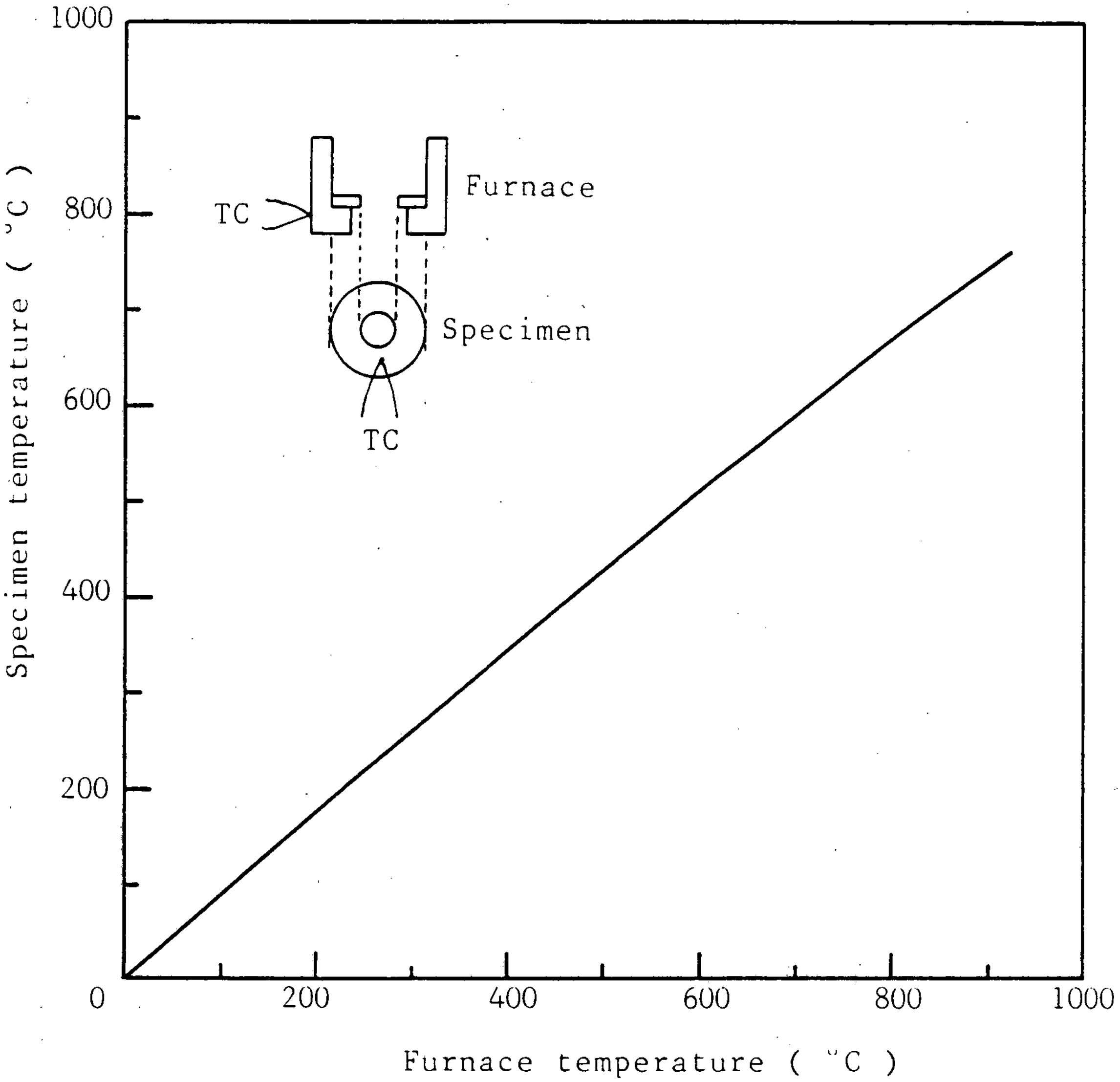

XBL 8412-5451

Figure 7.

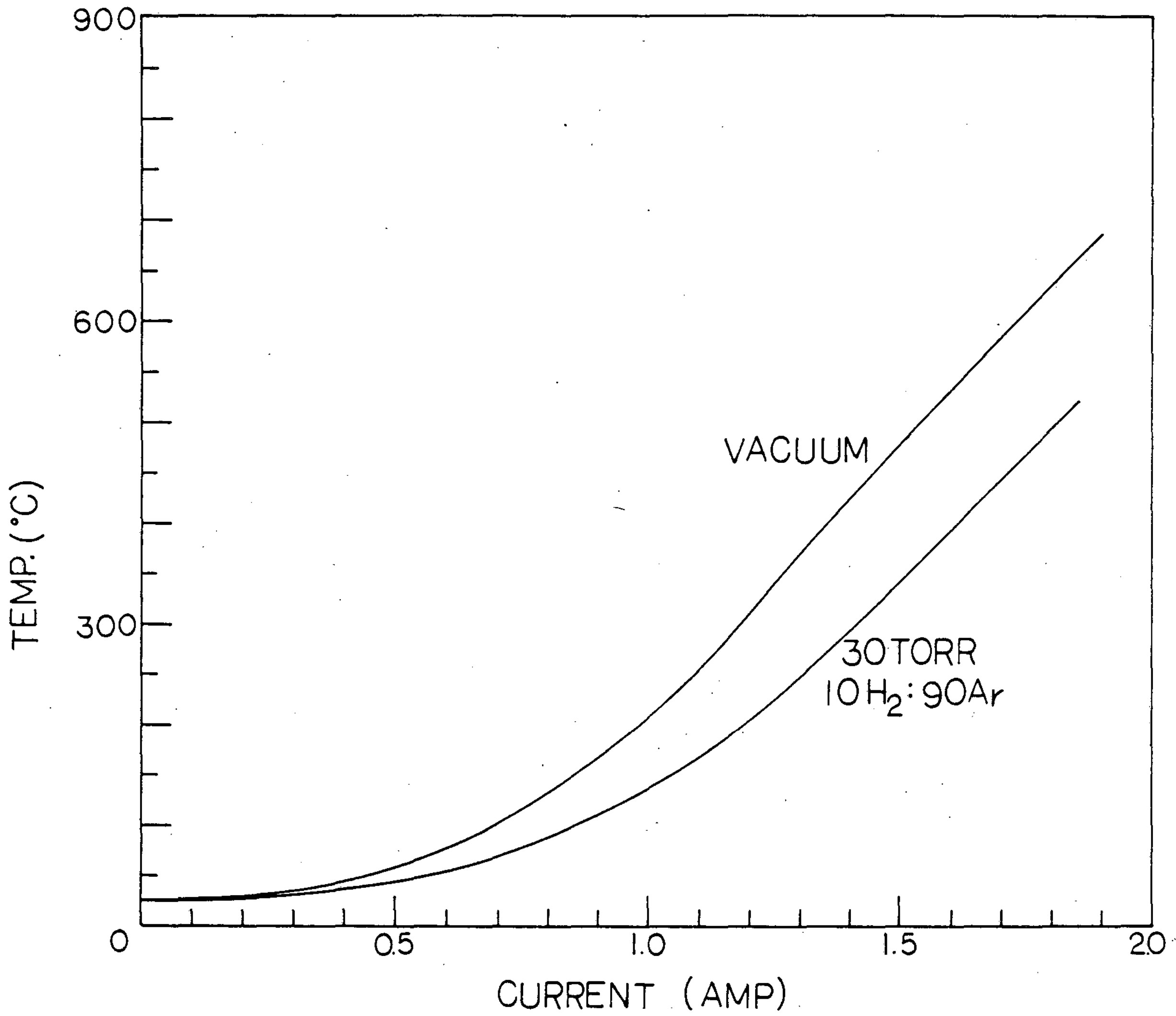

XBL 8412-5454

Figure 8.

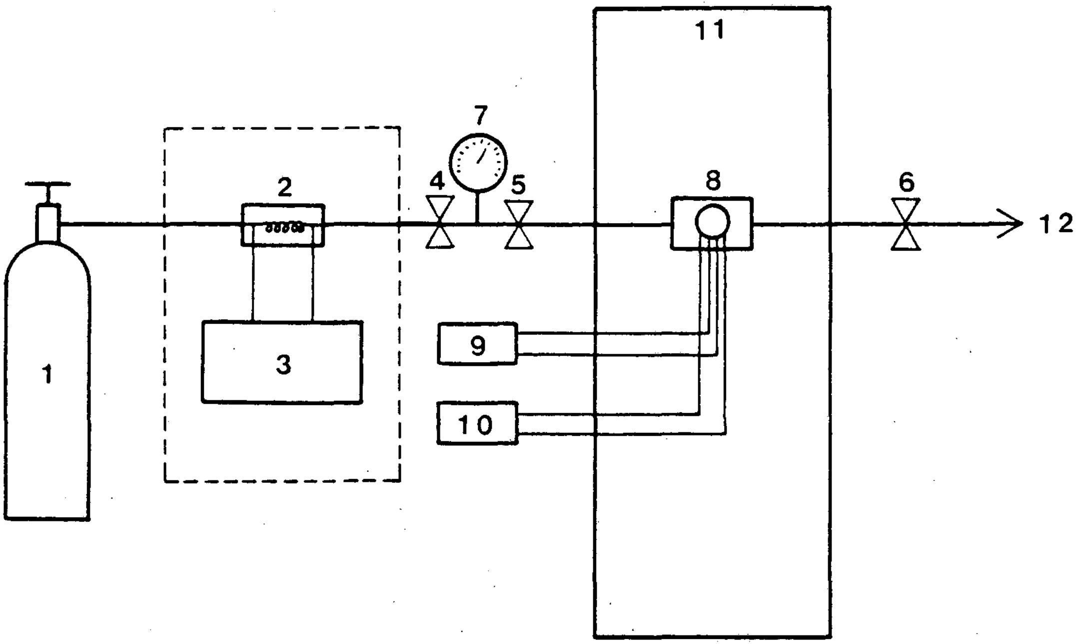

1. gas mixture
2. transducer
3. digital flowmeter
4. gate valve
5. needle valve
6. gate valve
7. pressure gauge
8. E-cell
9. thermocouple
10. power supply
11. HVEM
12. to mechanical pump

XBL 8412-5450

Figure 9.

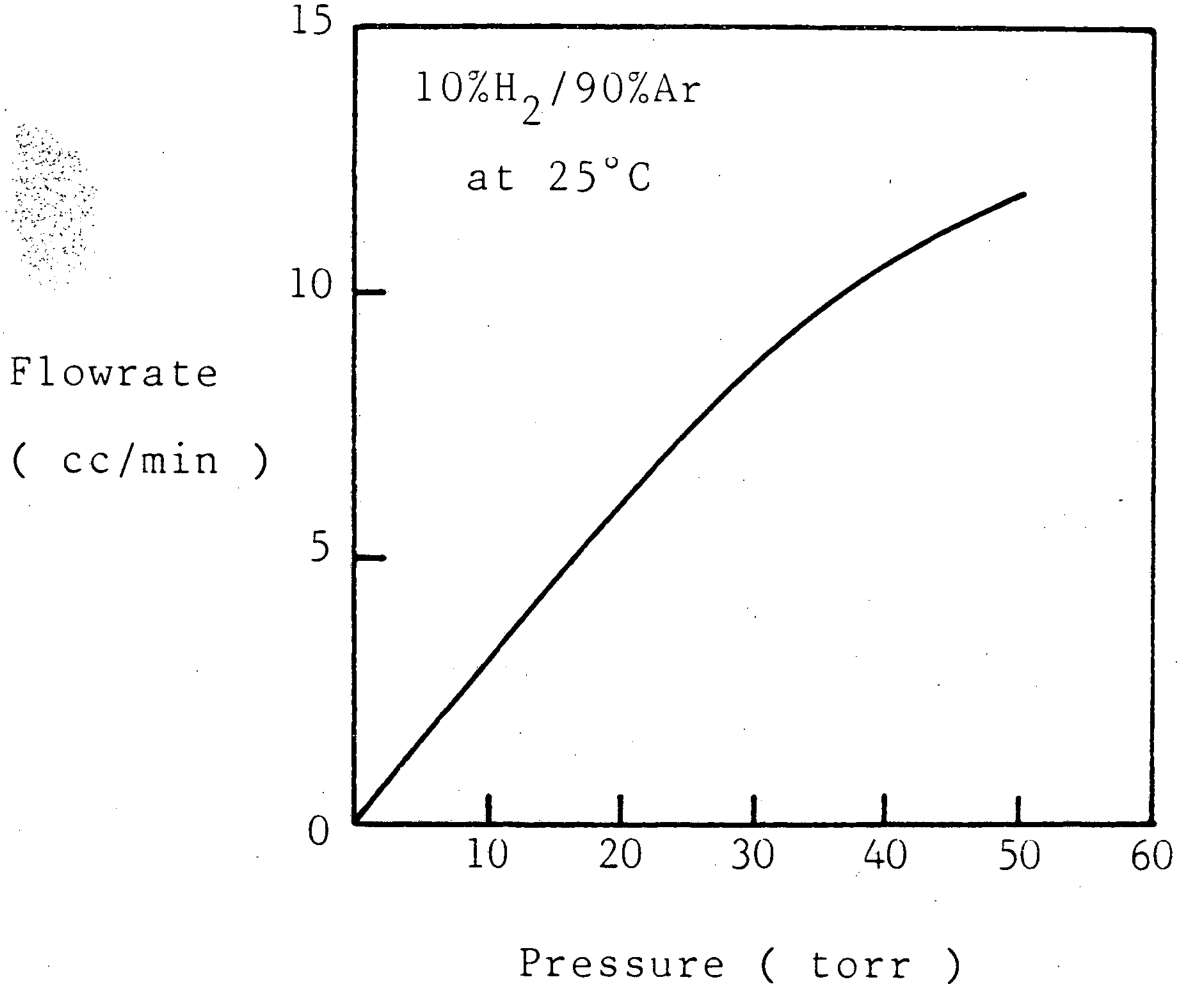

Figure 10.

XBL 8412-5444

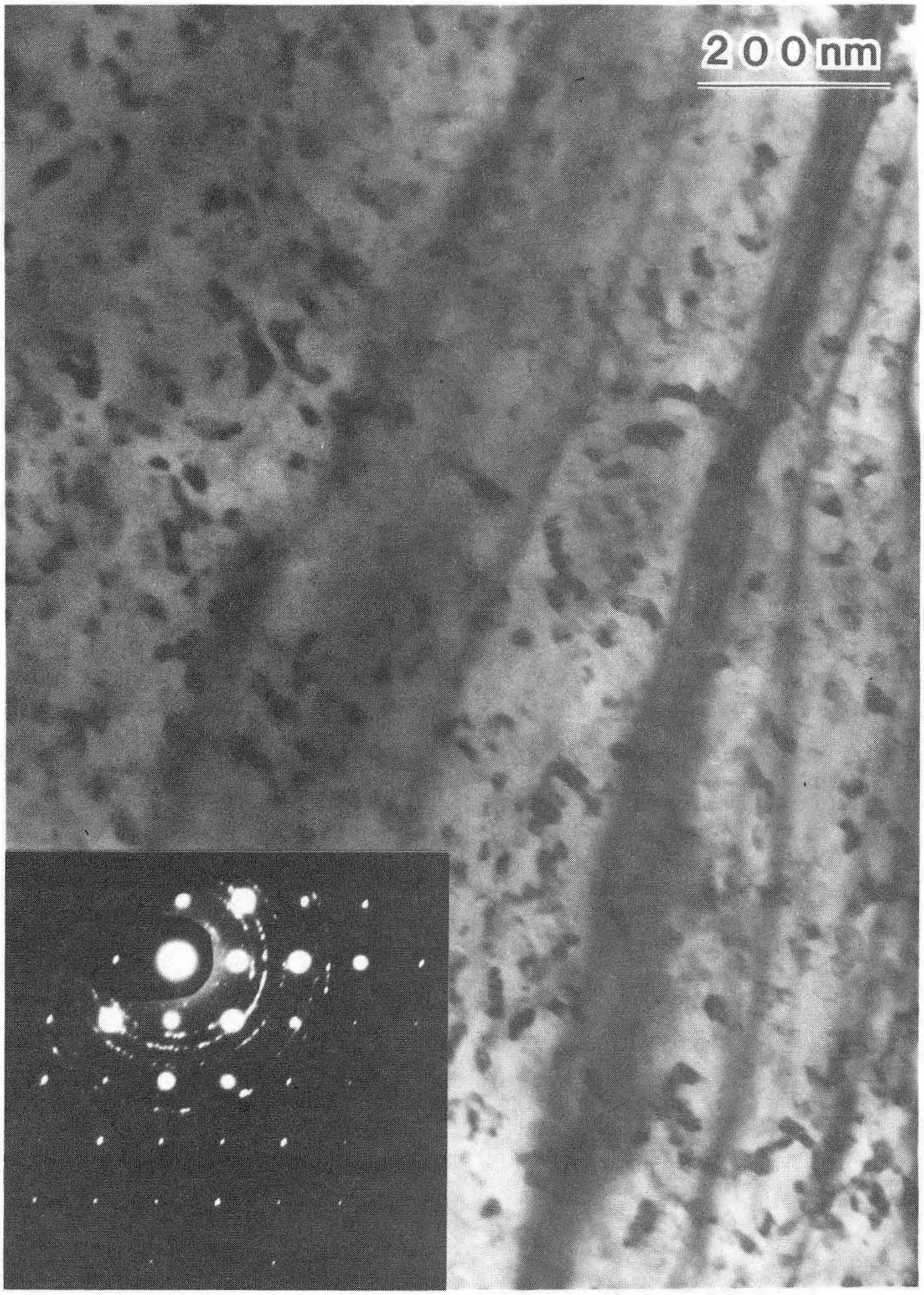

XBB 840-9622

Figure 11.

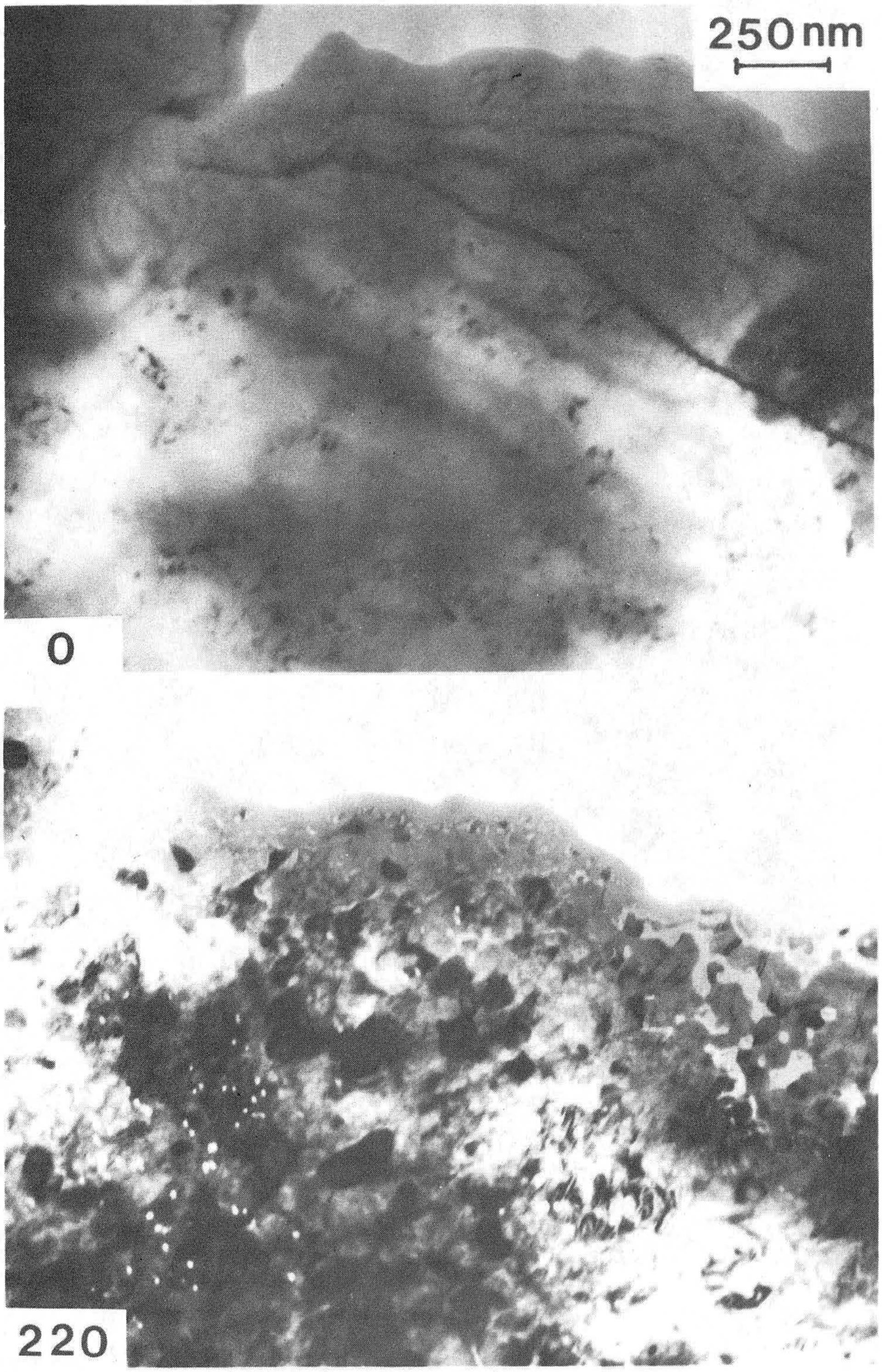

XBB 840-9182

Figure 12.

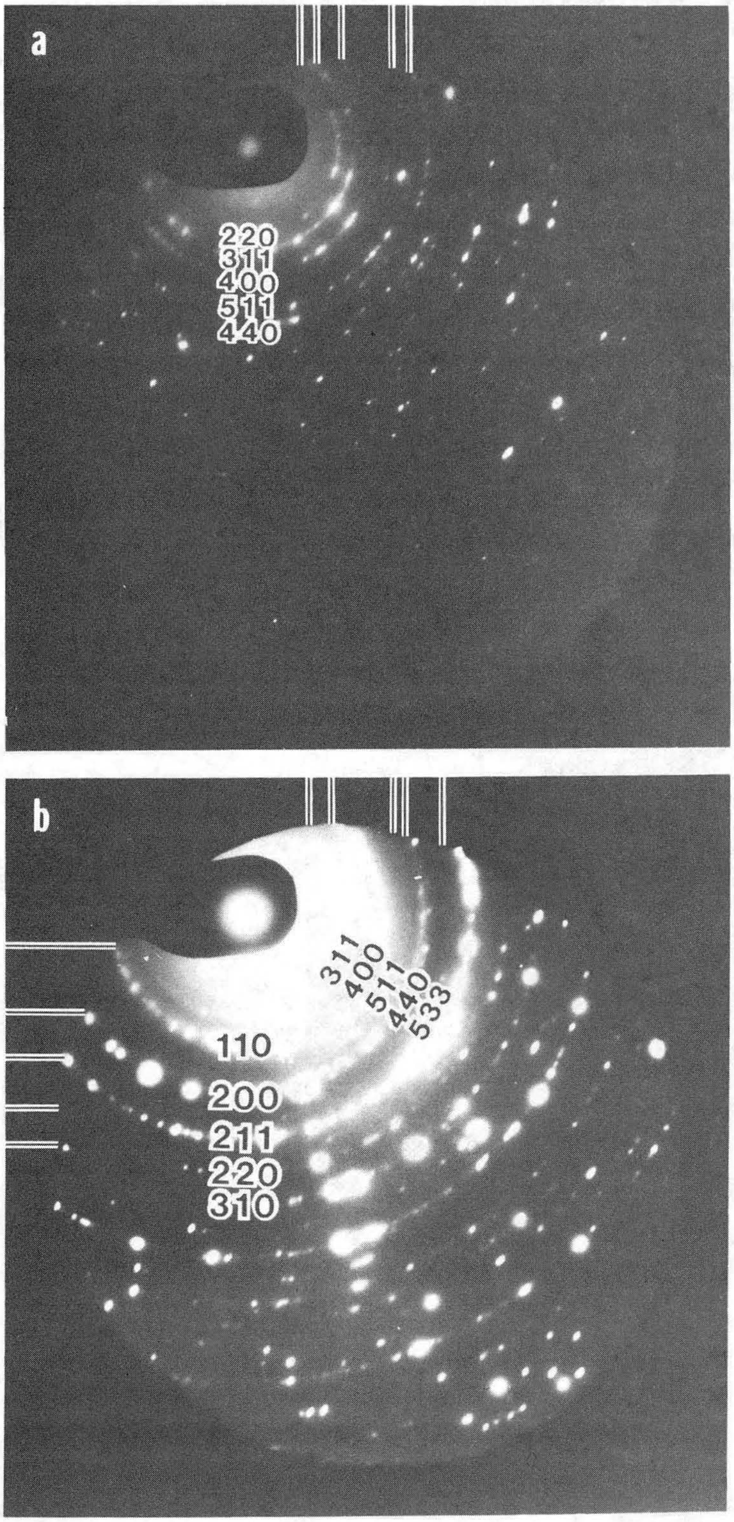

XBB 840-9598

Figure 13.

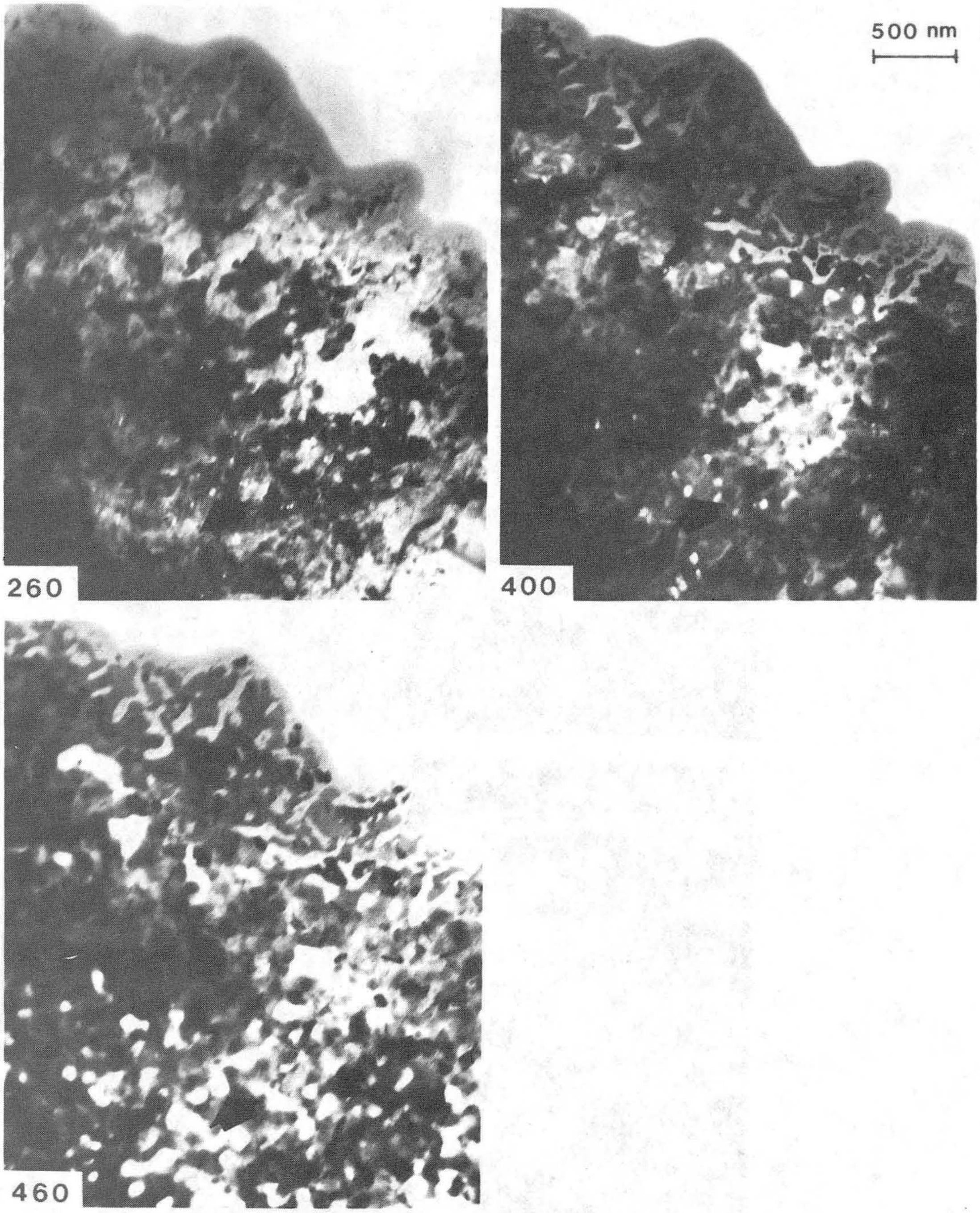

XBB 840-9599

Figure 14.

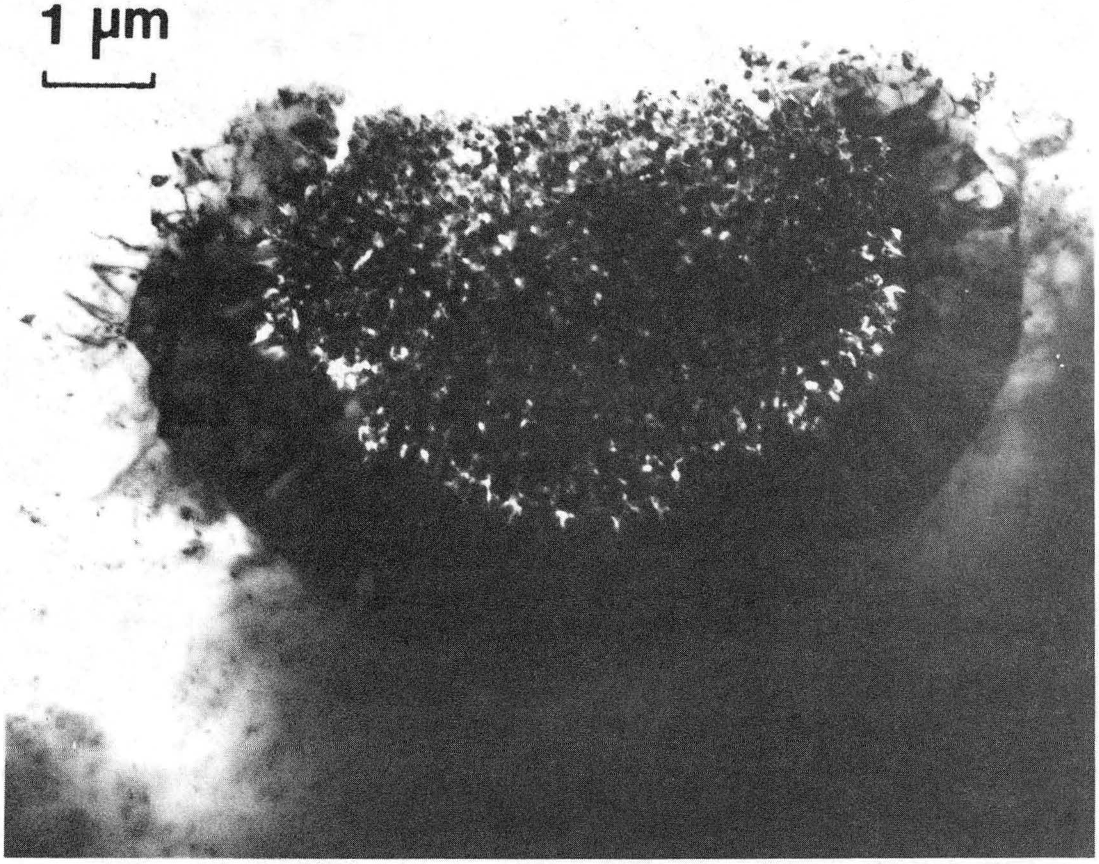

XBB 840-9600

Figure 15.

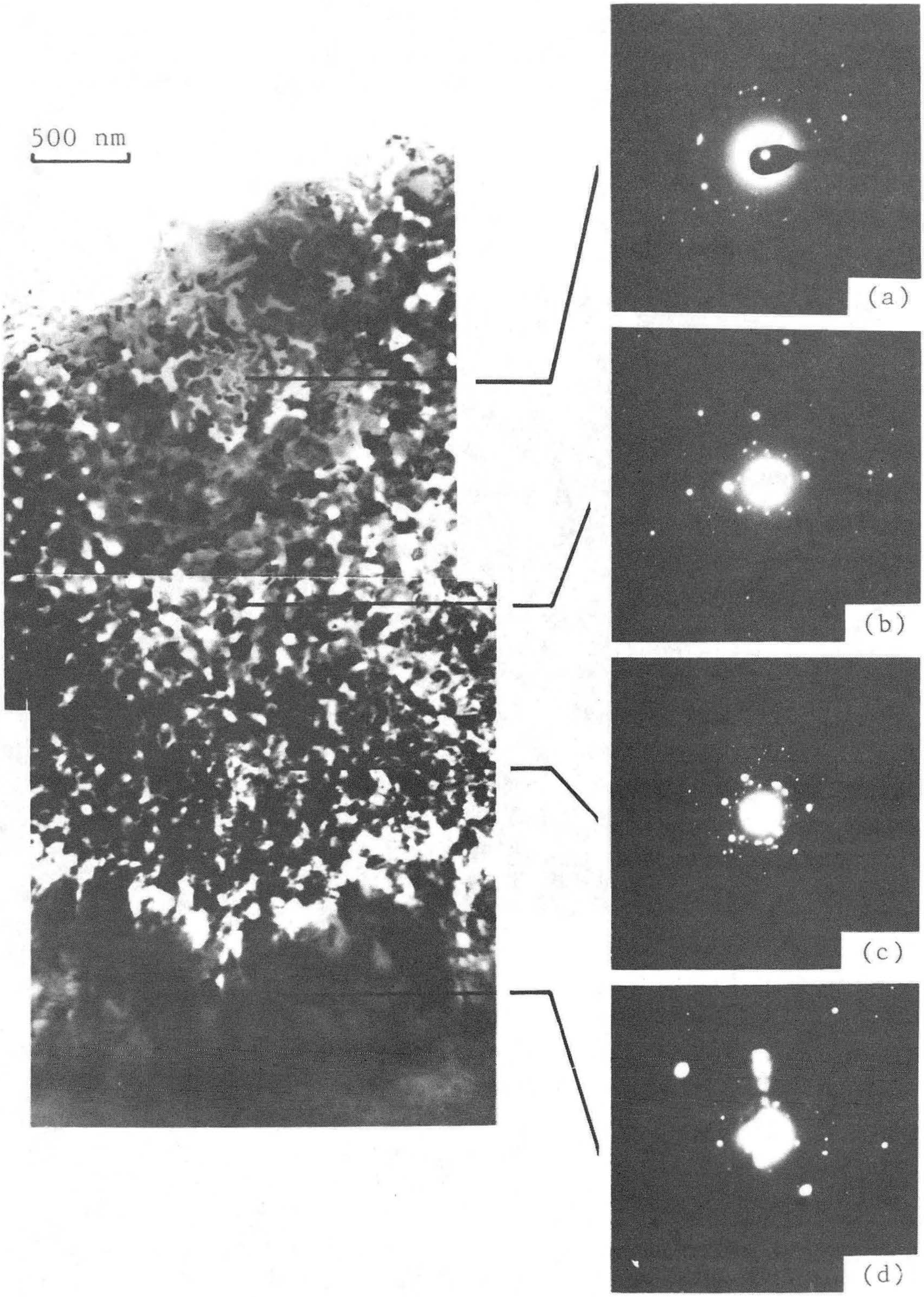

XBB 840-9585

Figure 16.

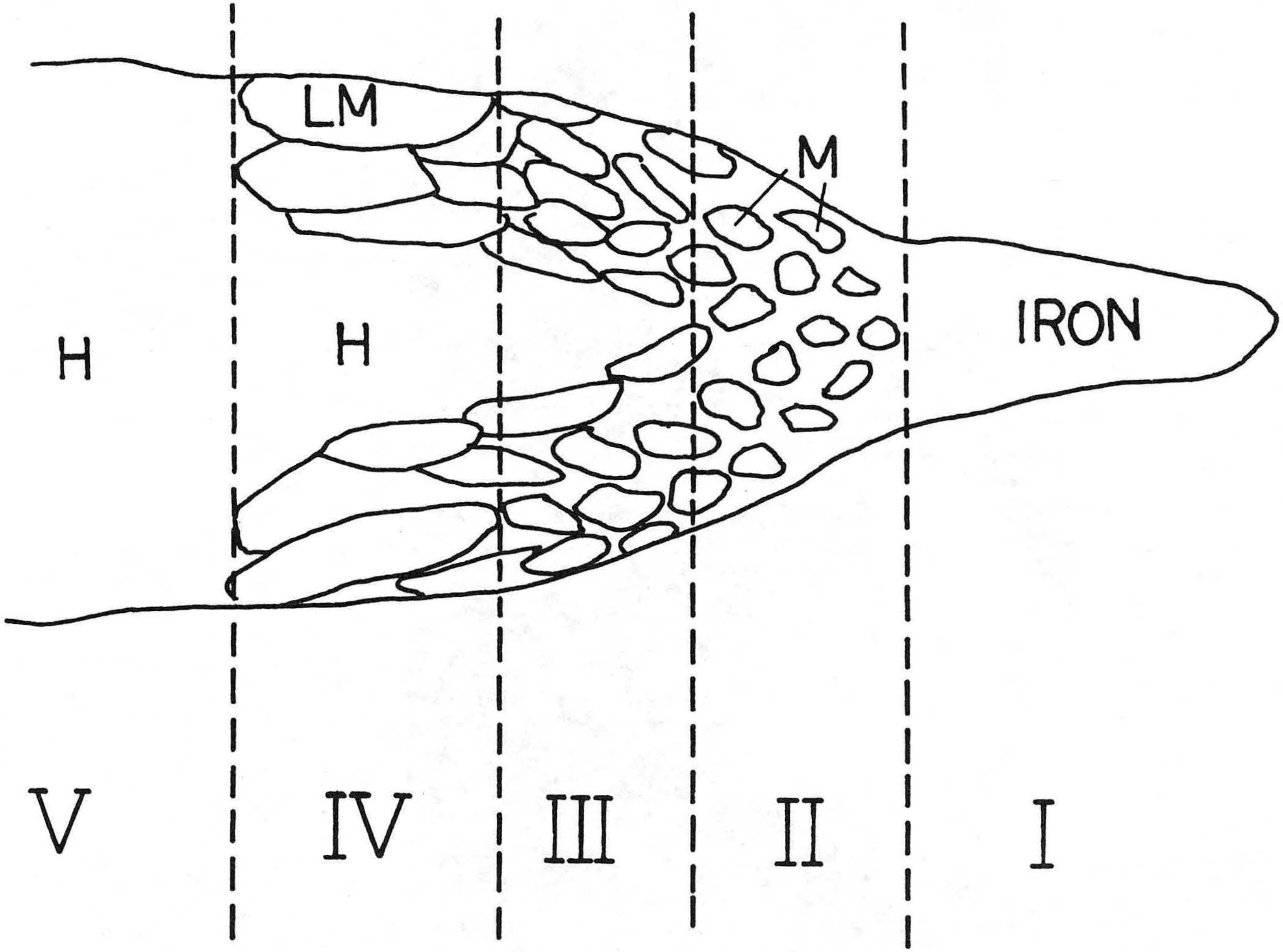

Figure 17.

XBL 8412-5449

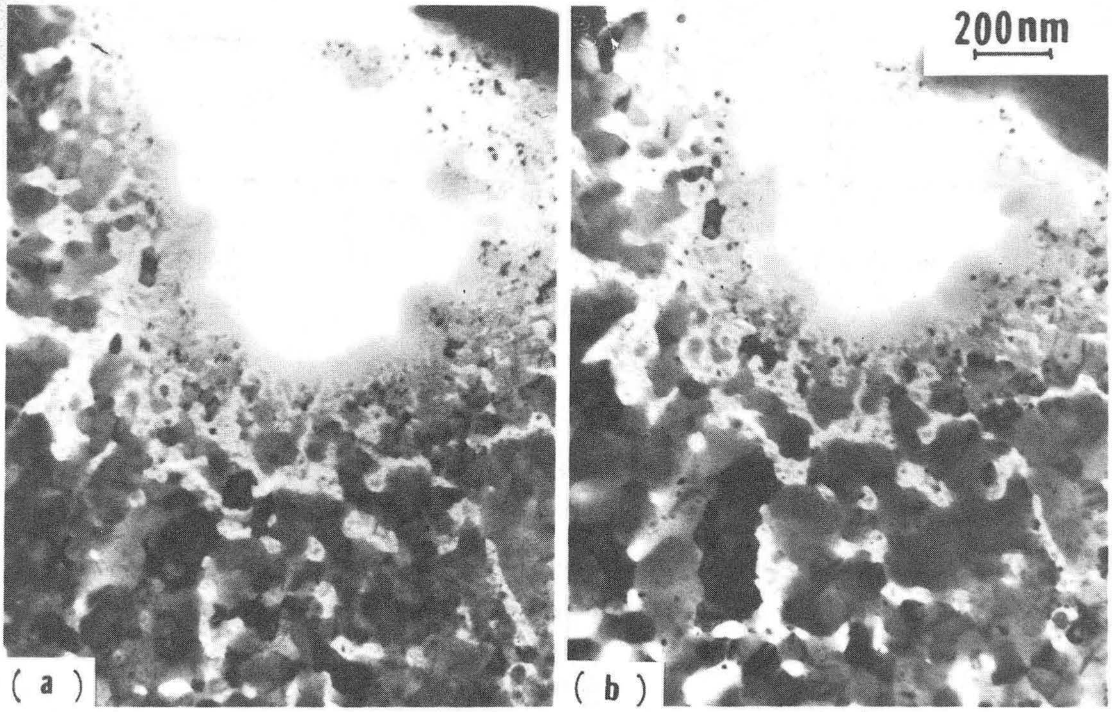

XBB 840-9596

Figure 18.

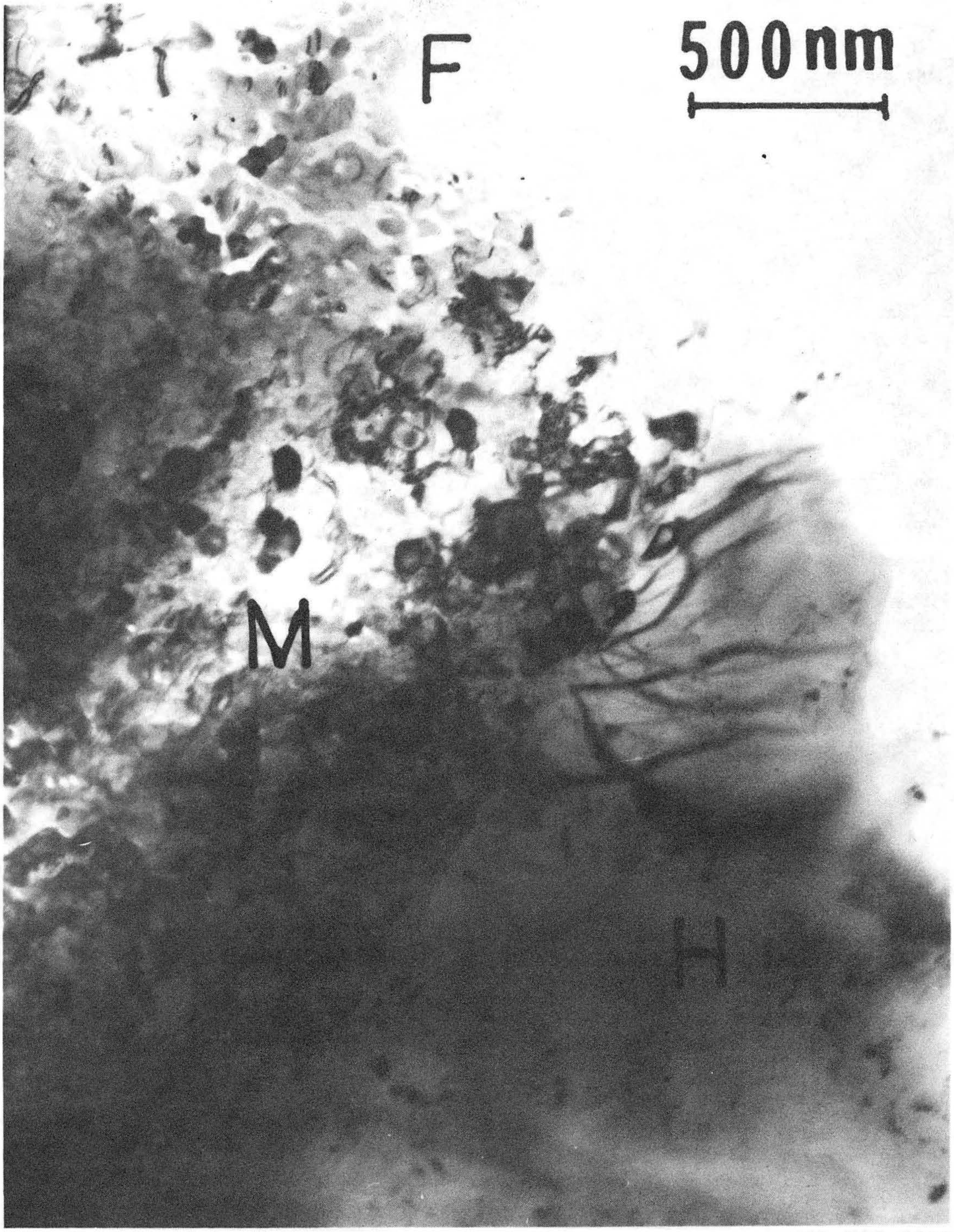

XBB 840-9583

Figure 19.

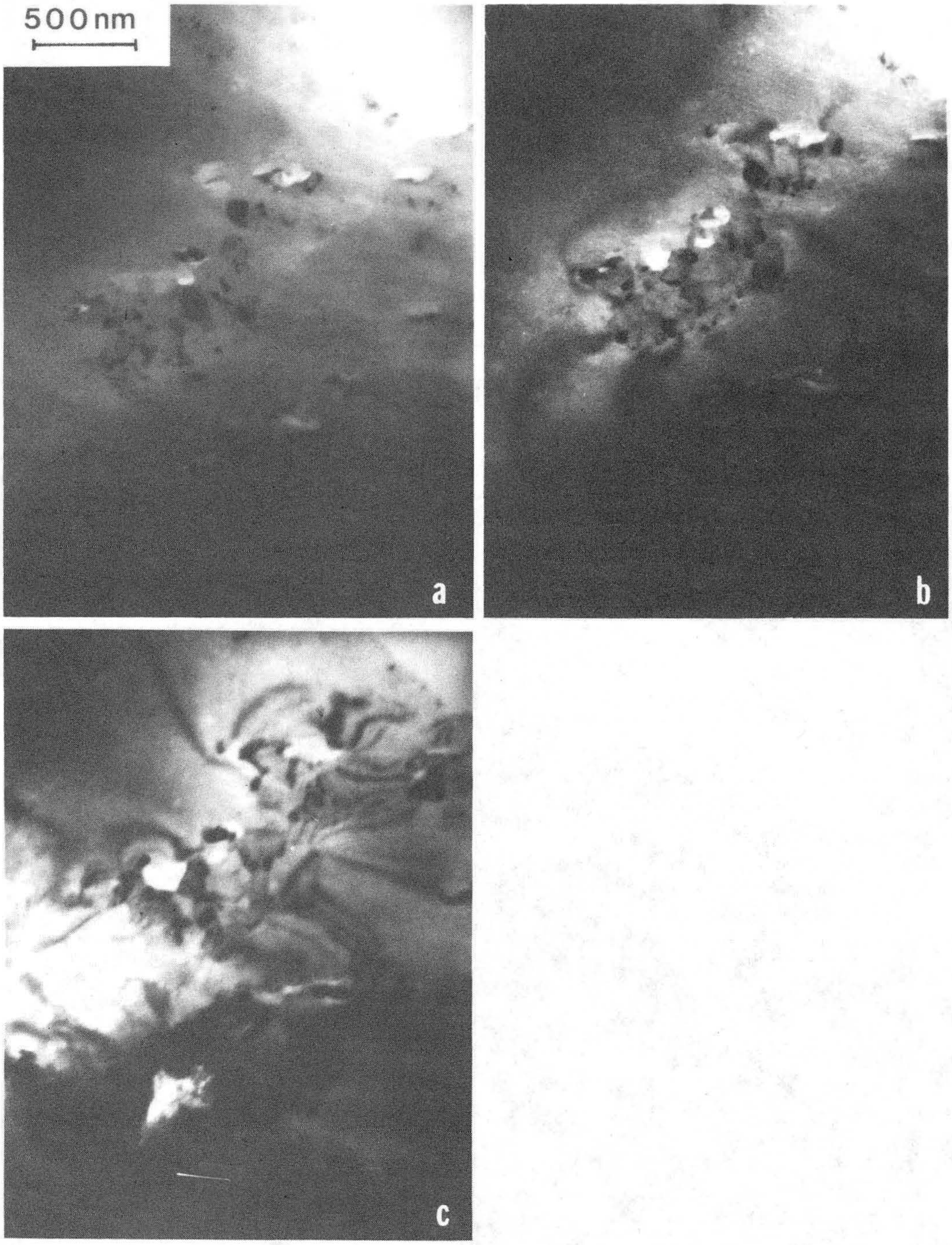

XBB 840-9623

Figure 20.

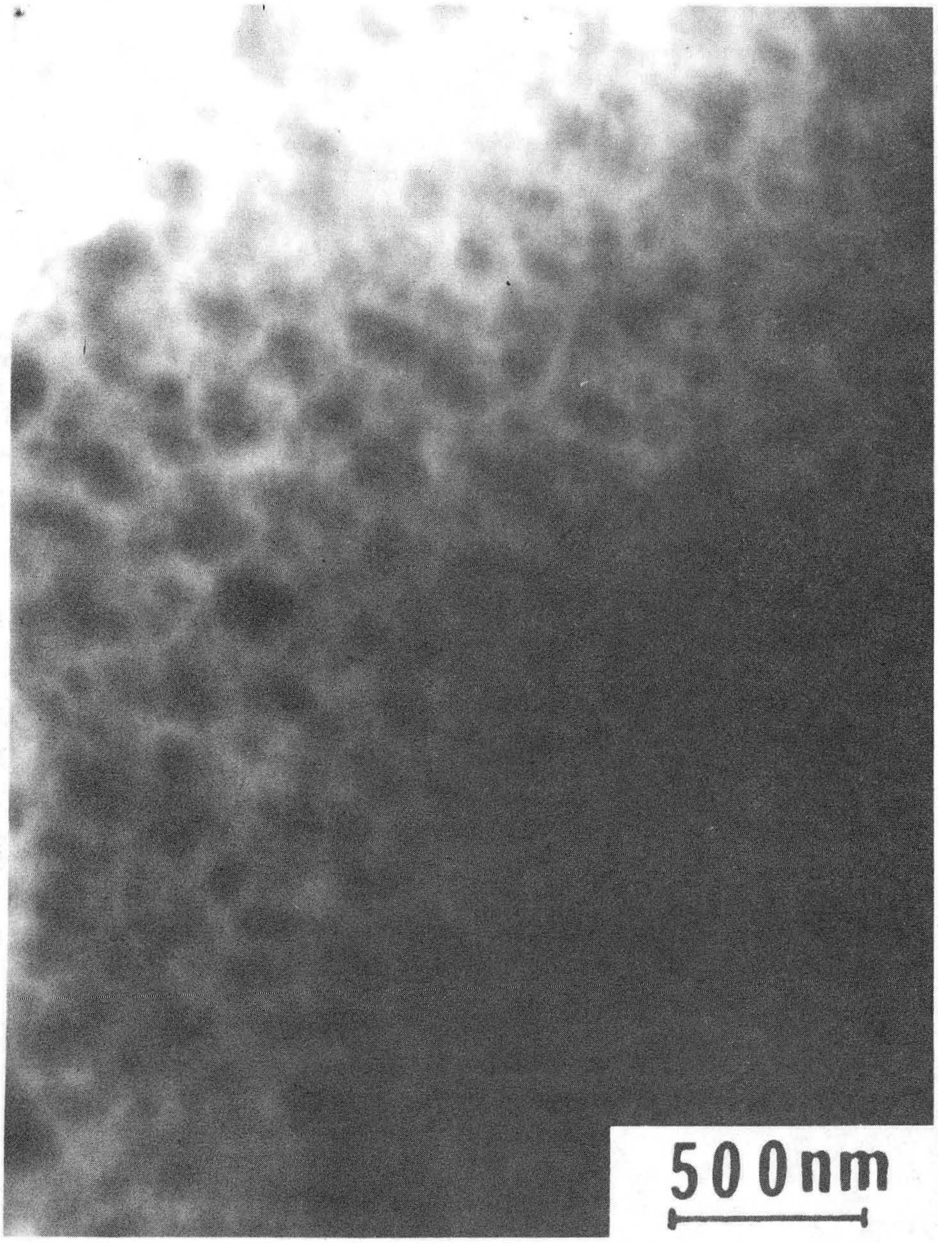

XBB 840-9594

Figure 21.

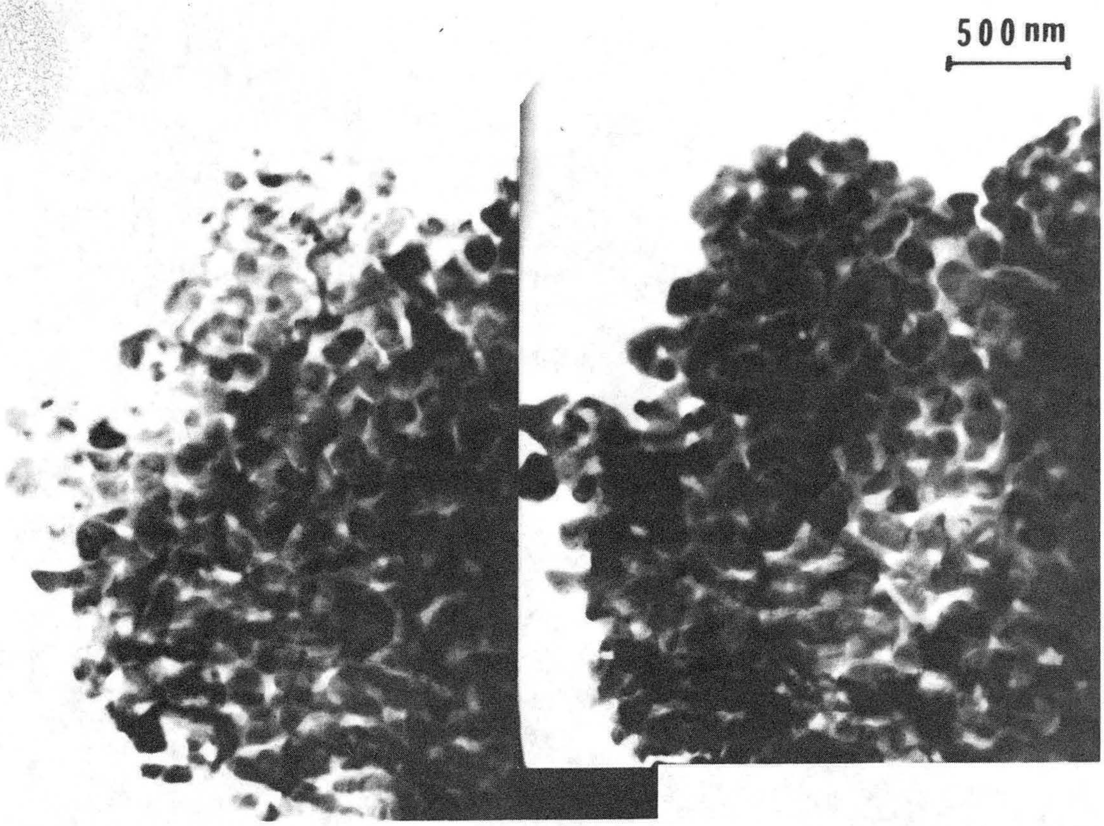

XBB 840-9587

Figure 22.

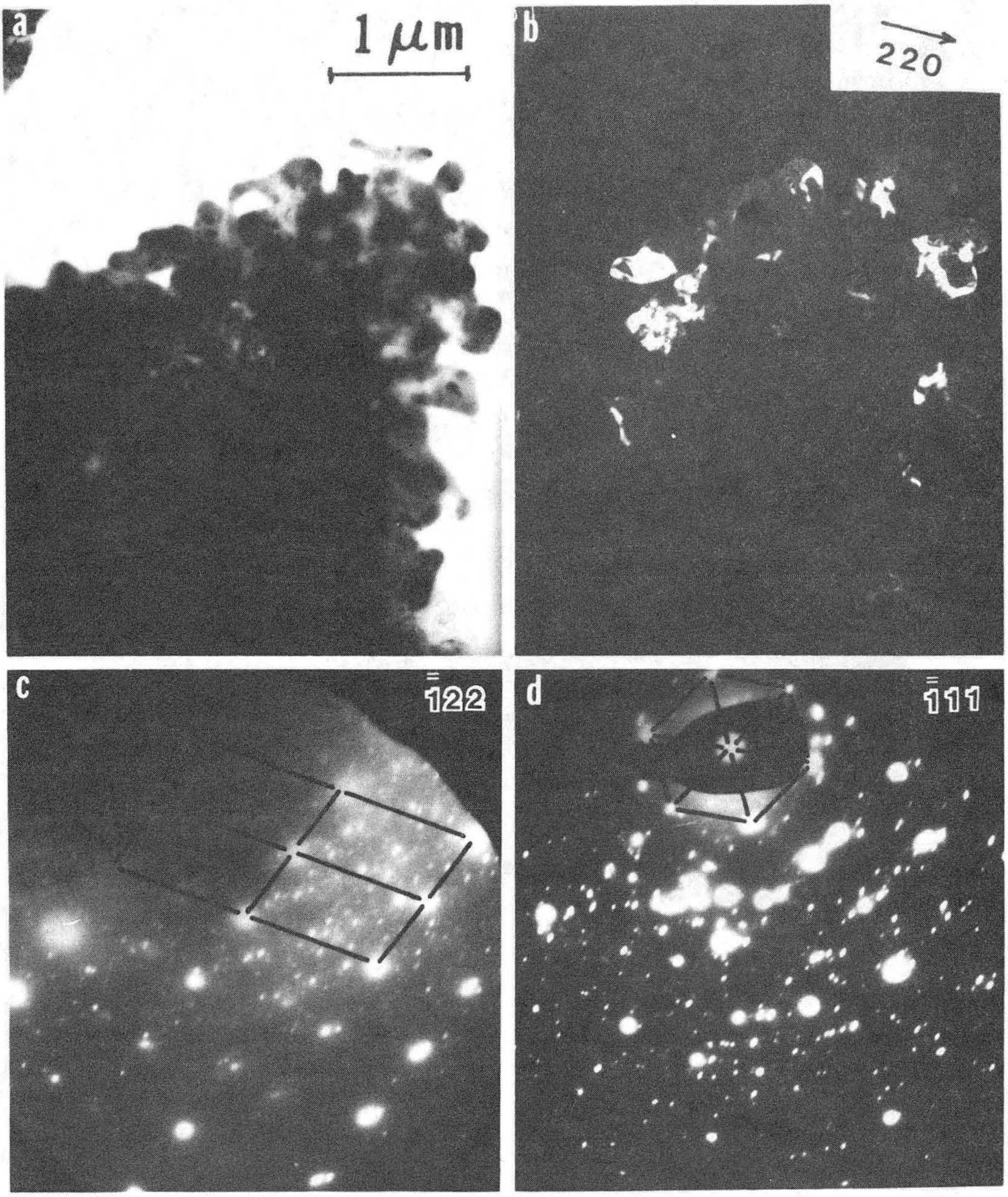

XBB 840-9624

Figure 23.

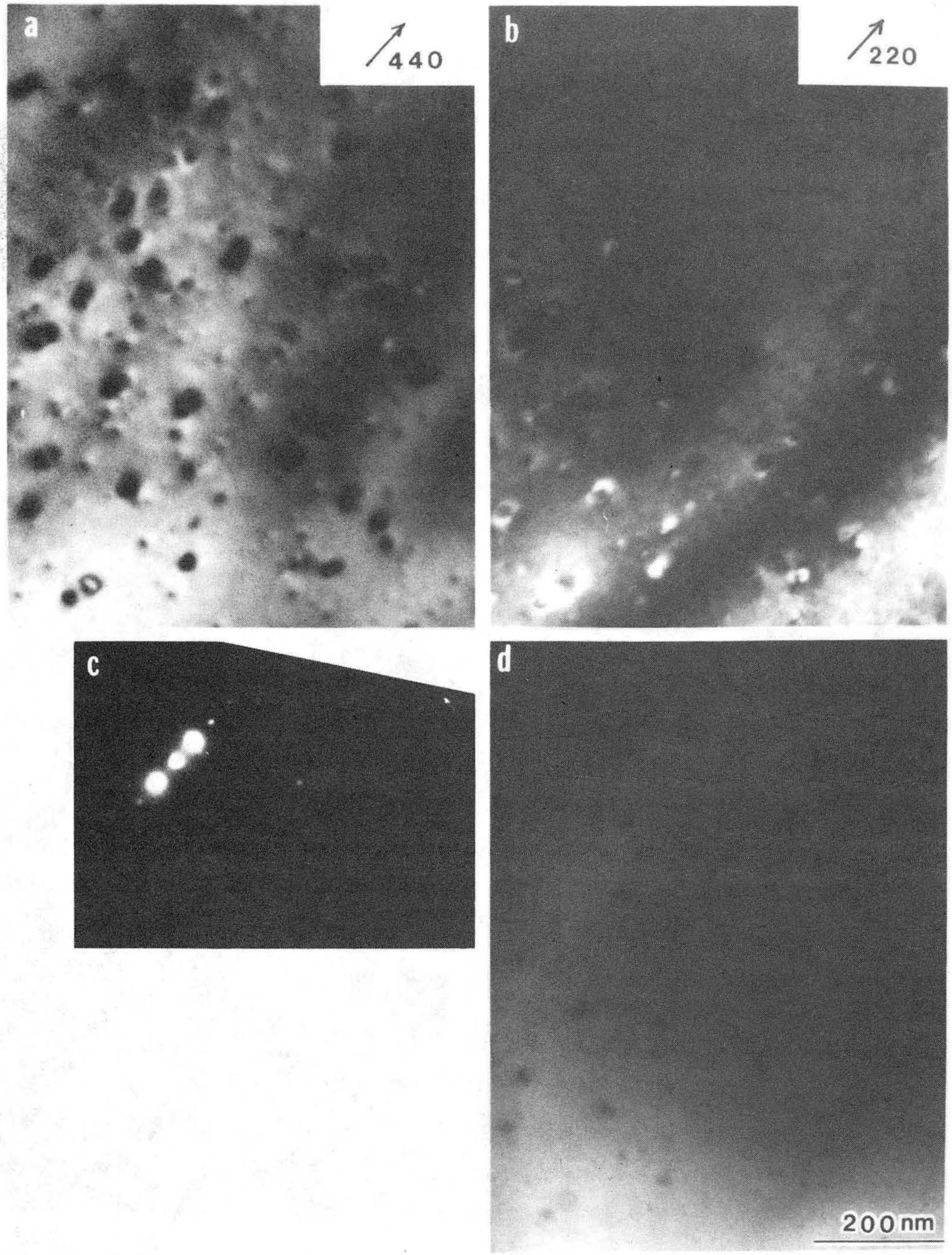

XBB 840-9625

Figure 24.

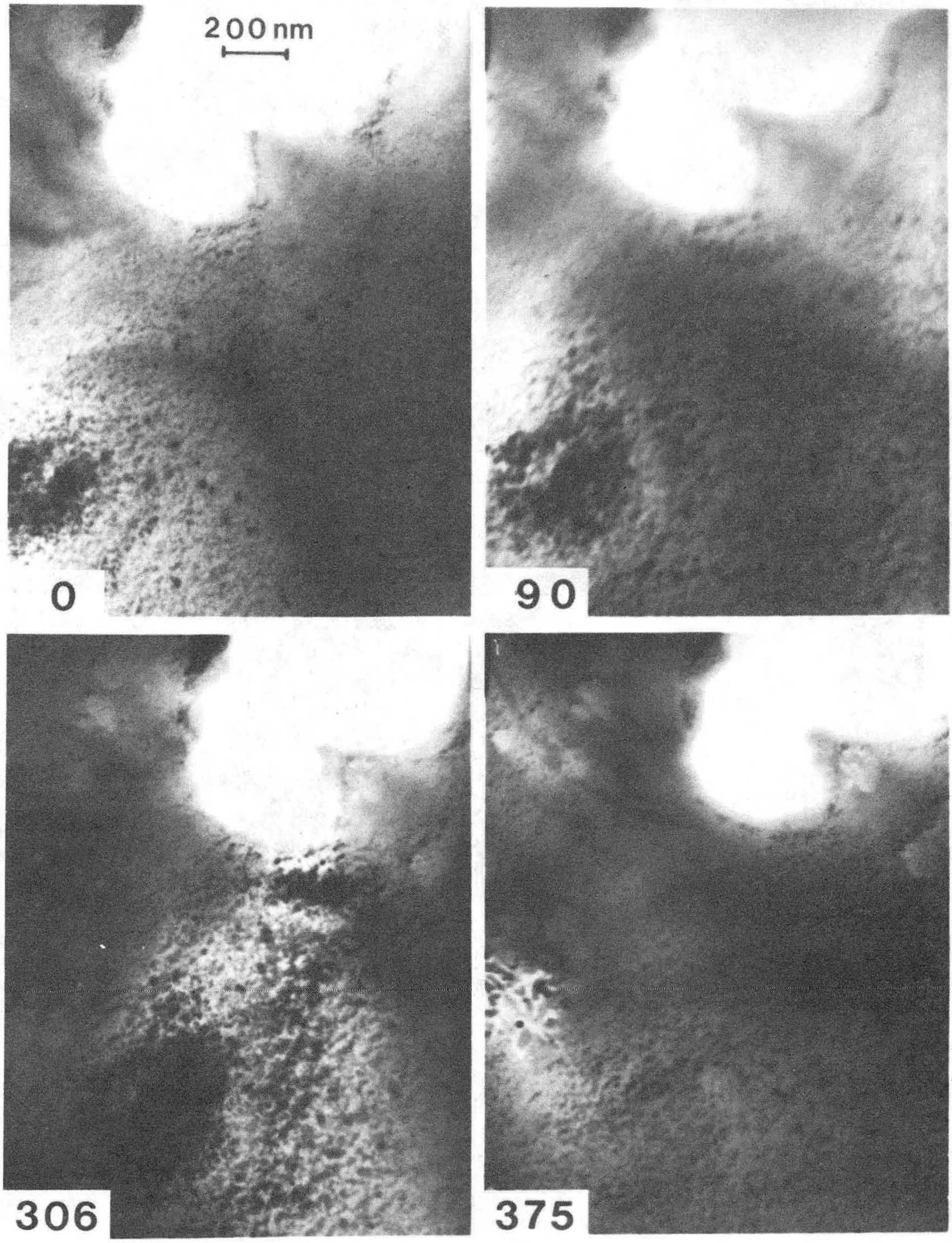

XBB 840-9194

Figure 25(a).

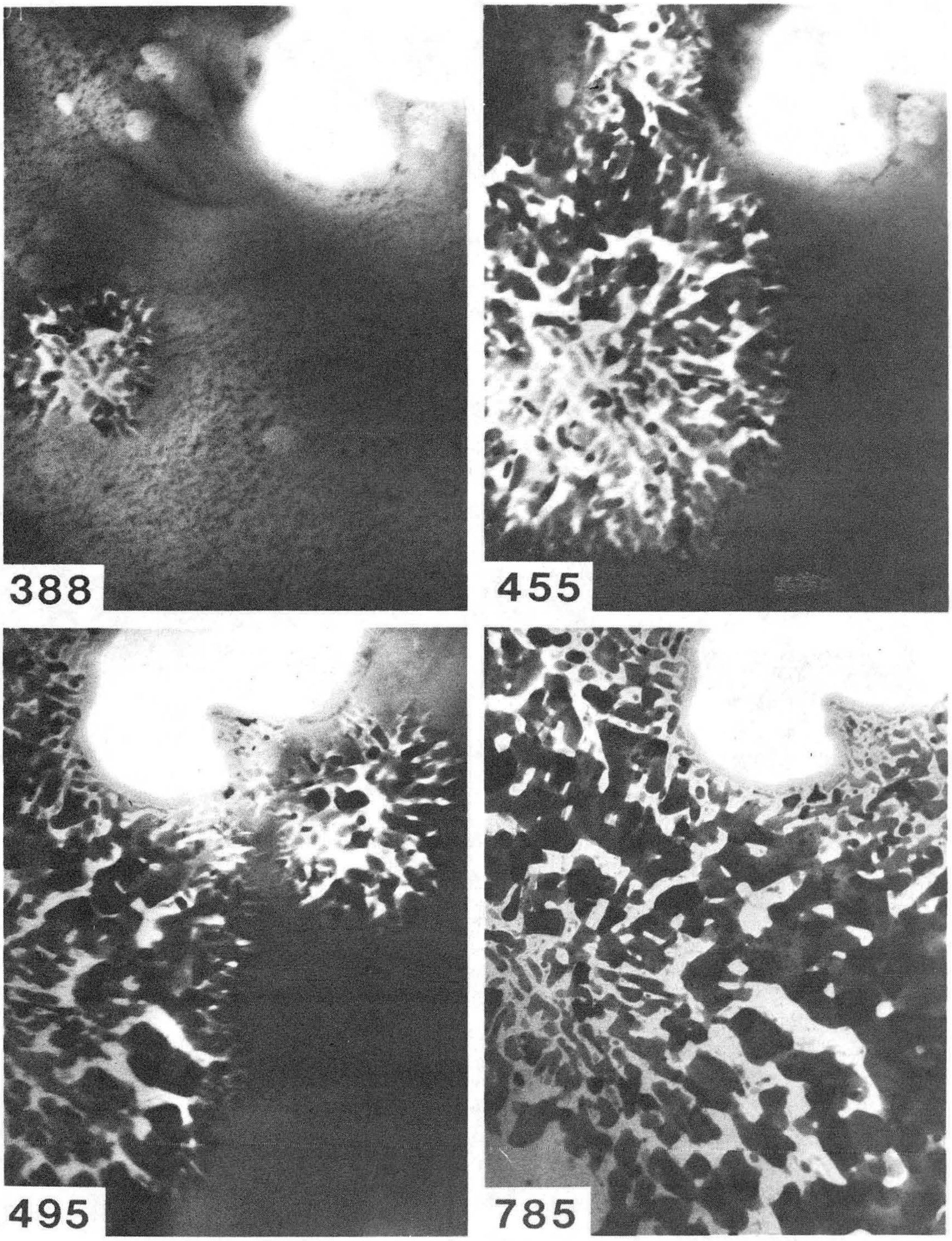

XBB 840-9193

Figure 25(b).

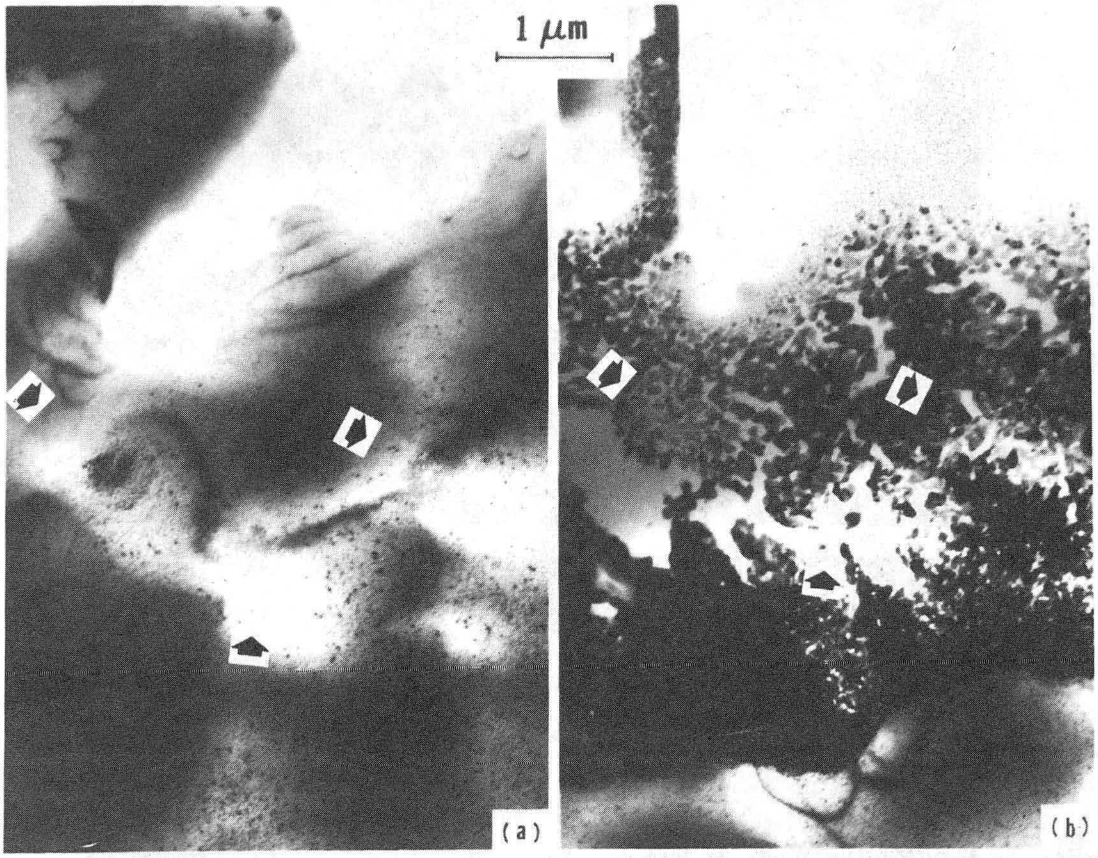

XBB 840-9184

Figure 26.

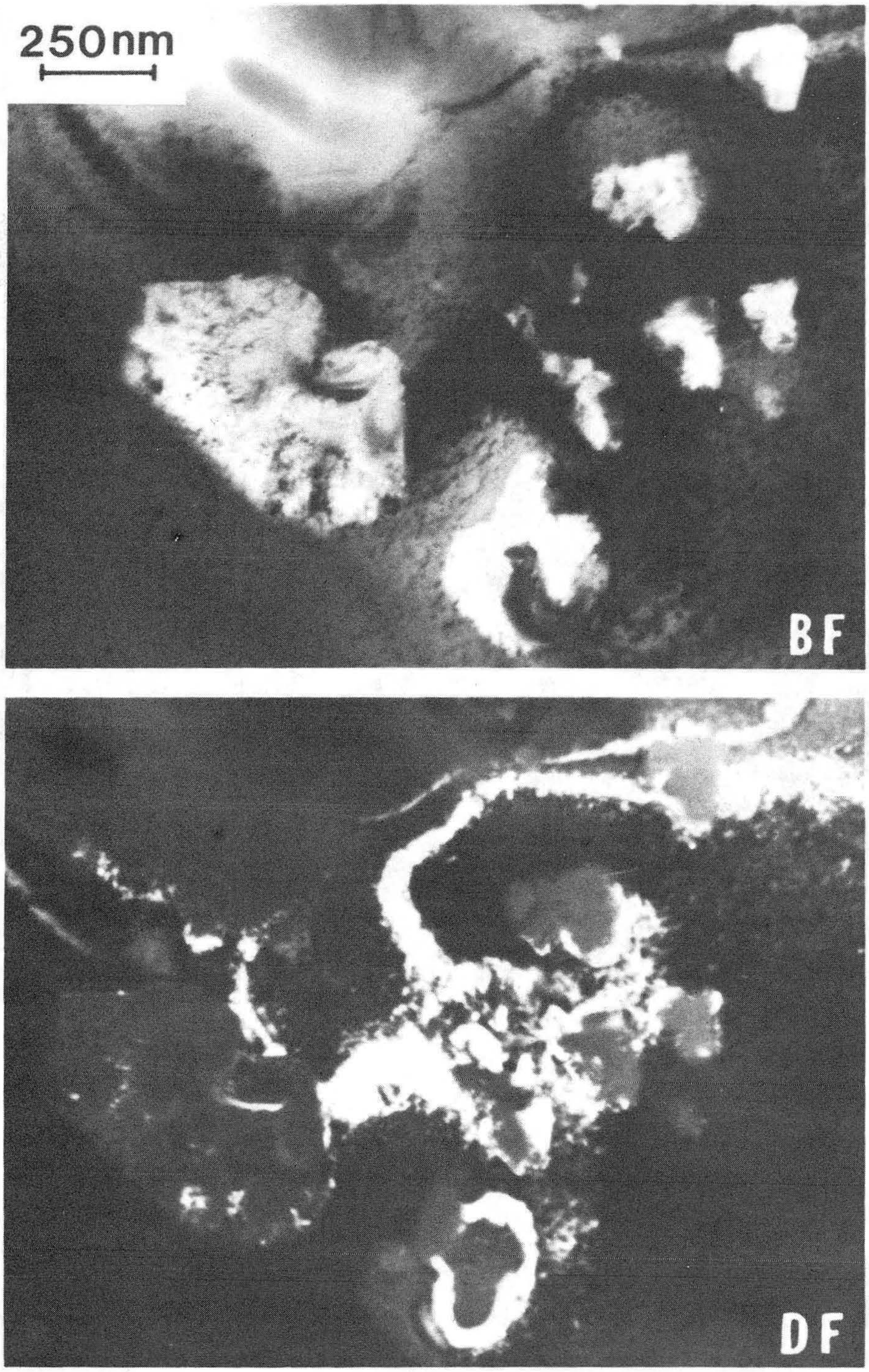

XBB 840-9192

Figure 27.

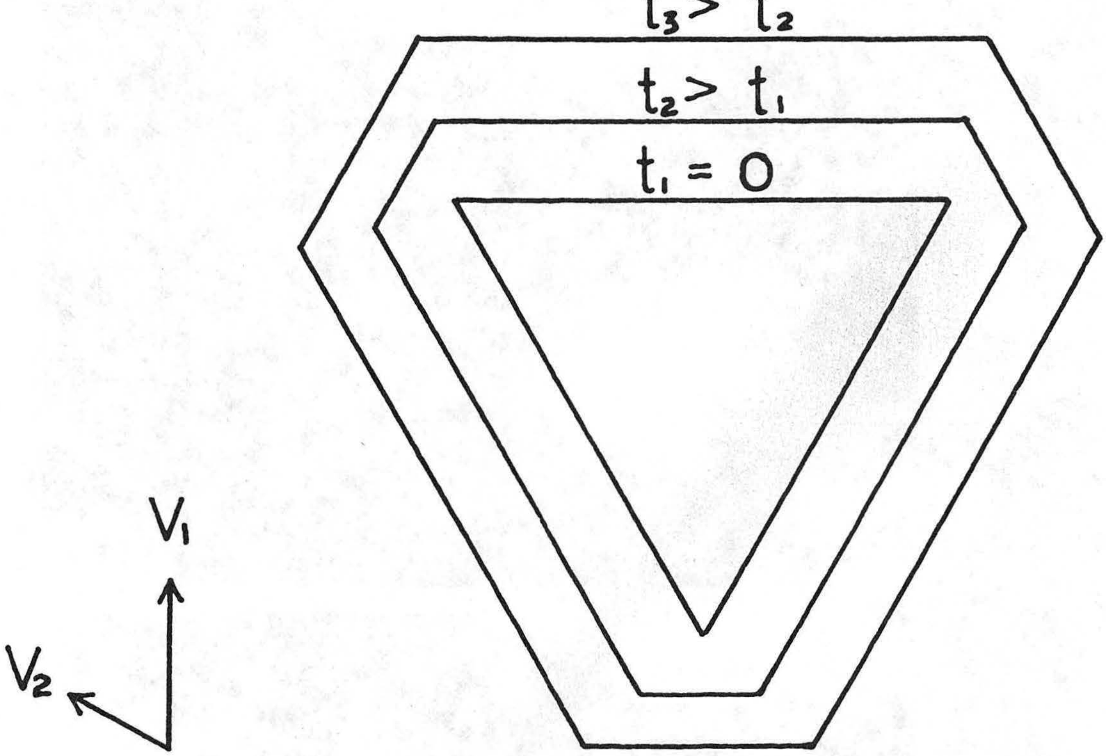

XBL 8412-5442

Figure 28.

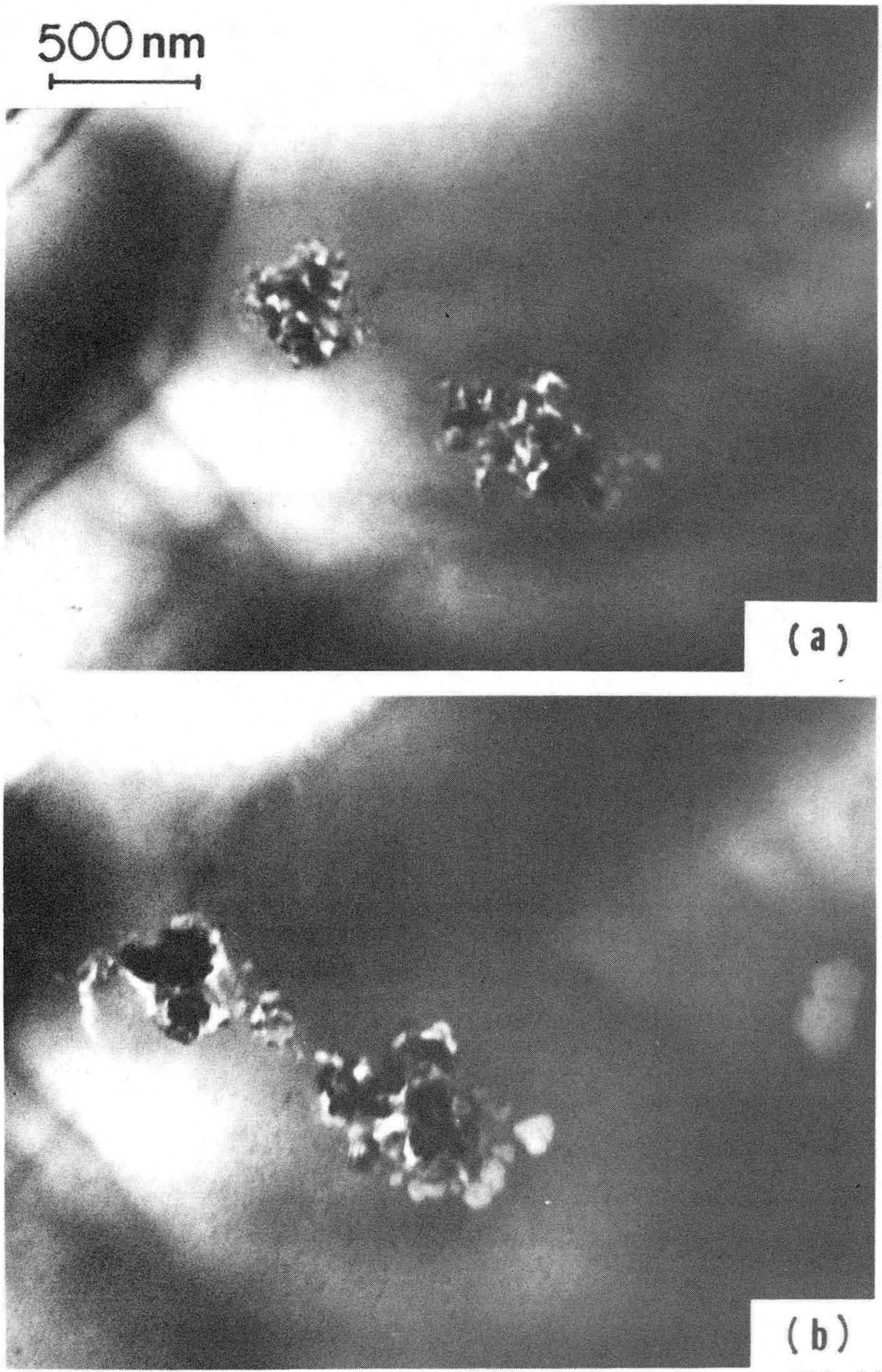

XBB 840-9191

Figure 29.

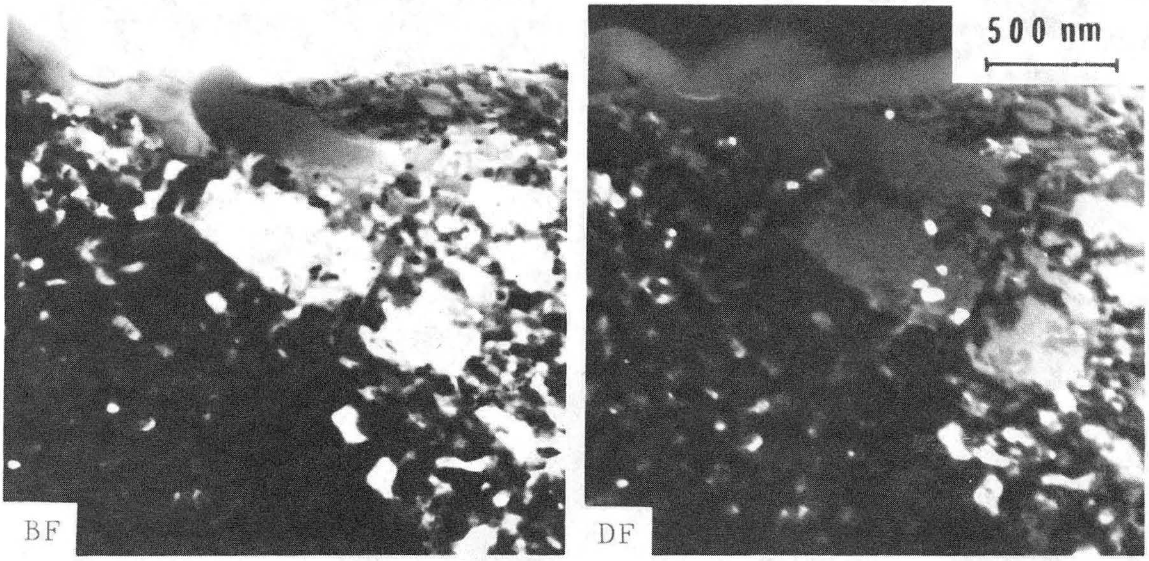

XBB 840-9593

Figure 30.

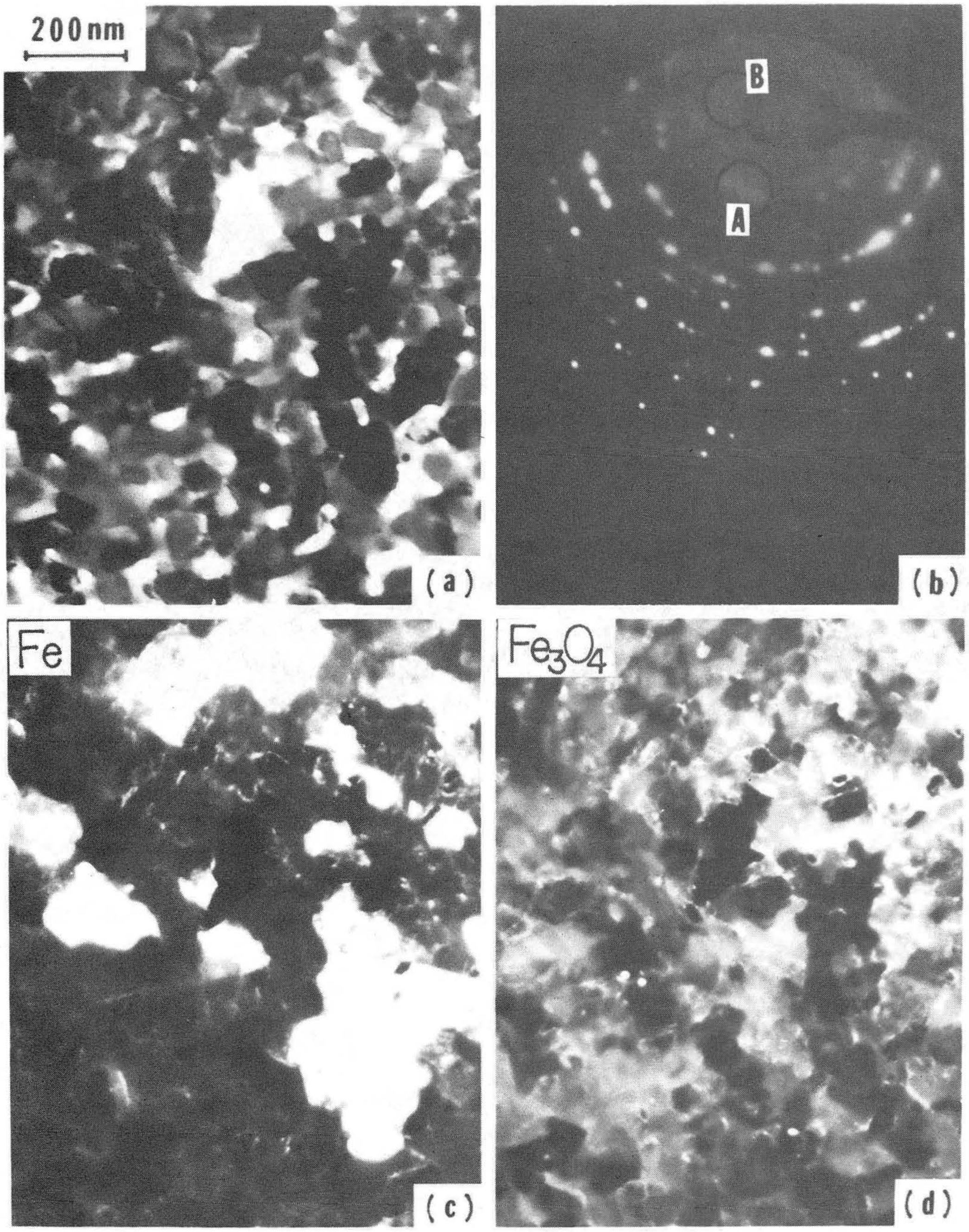

XBB 840-9604

Figure 31.

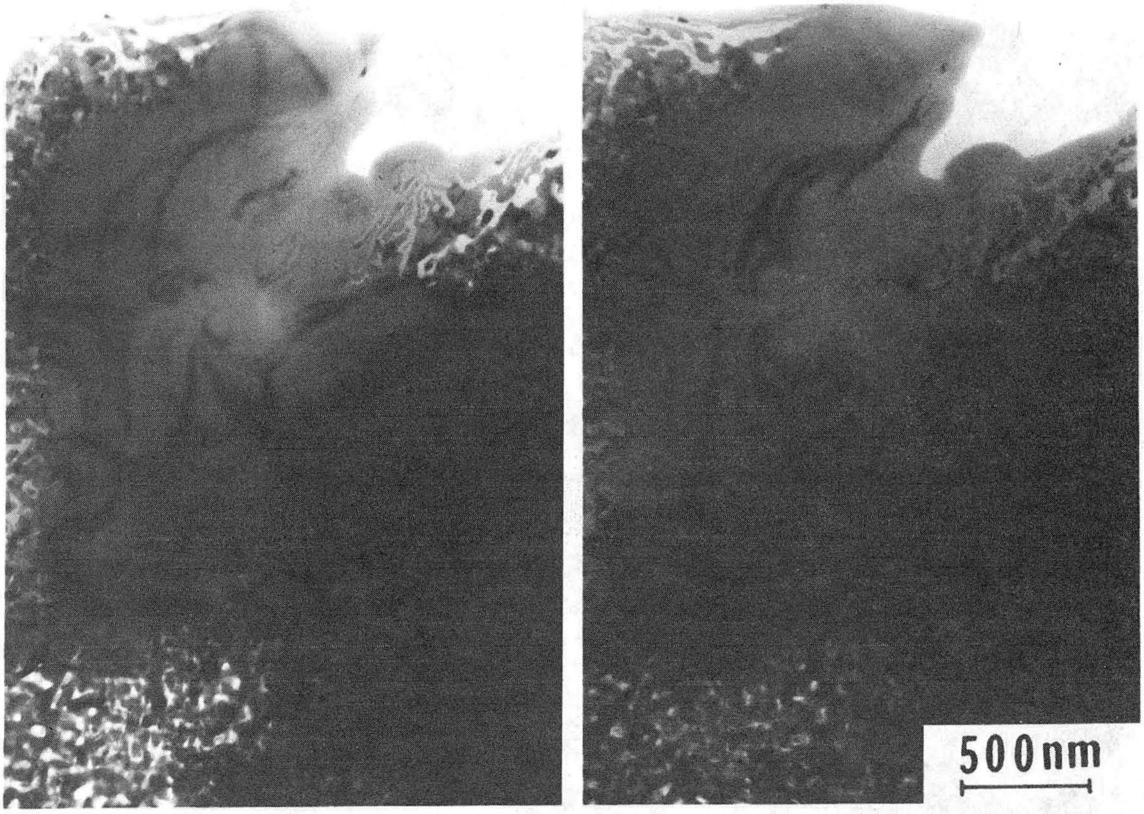

XBB 840-9595

Figure 32.

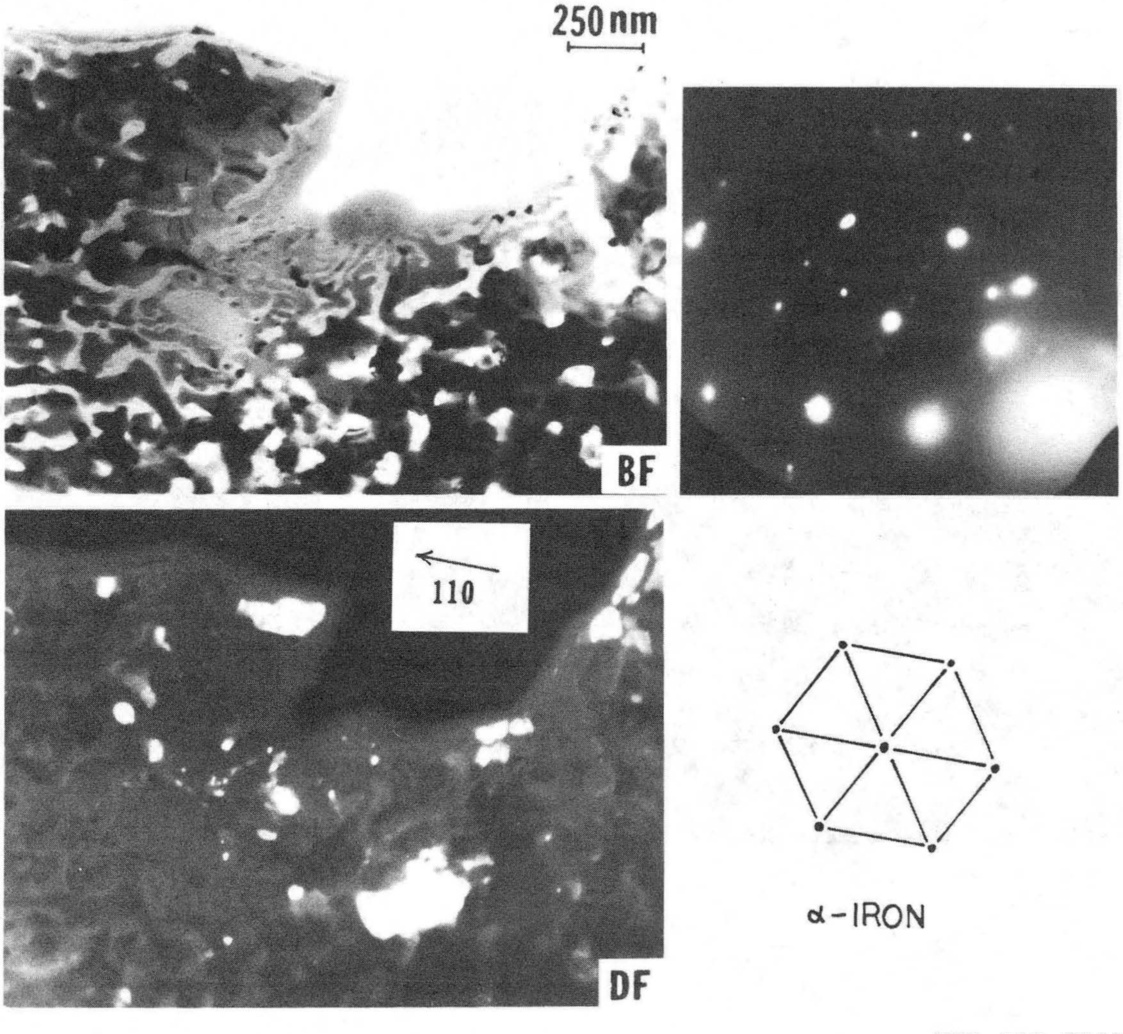

XBB 840-9584

Figure 33.

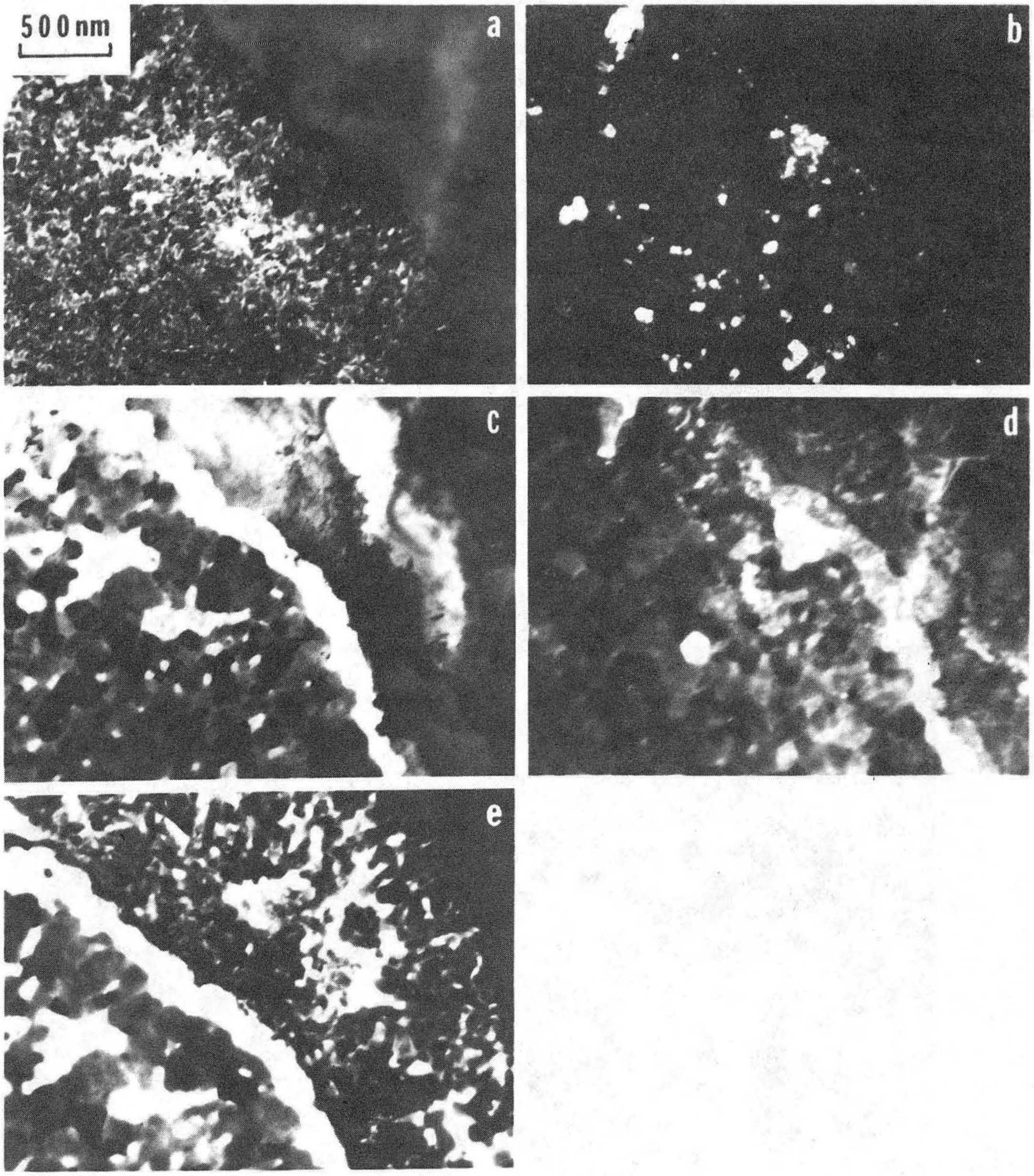

XBB 840-9603

Figure 34.

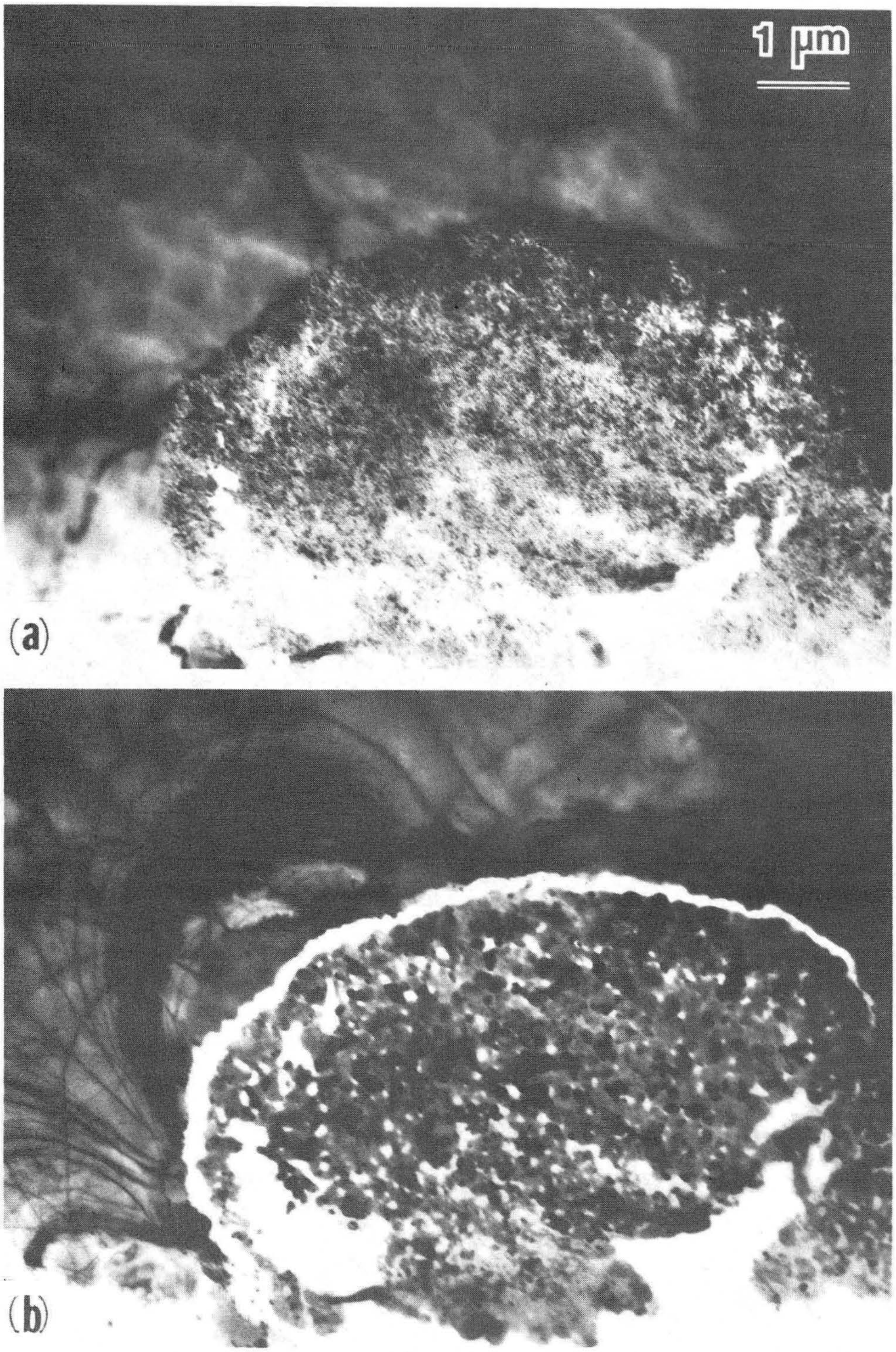

XBB 840-9602

Figure 35.

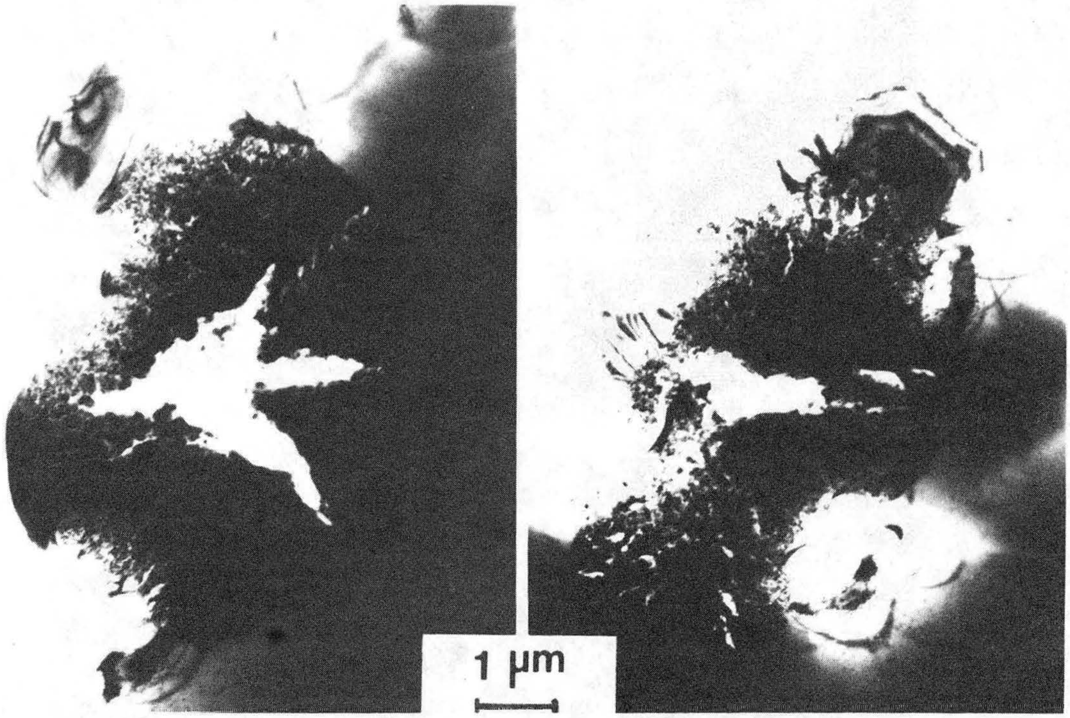

XBB 840-9185

Figure 36.

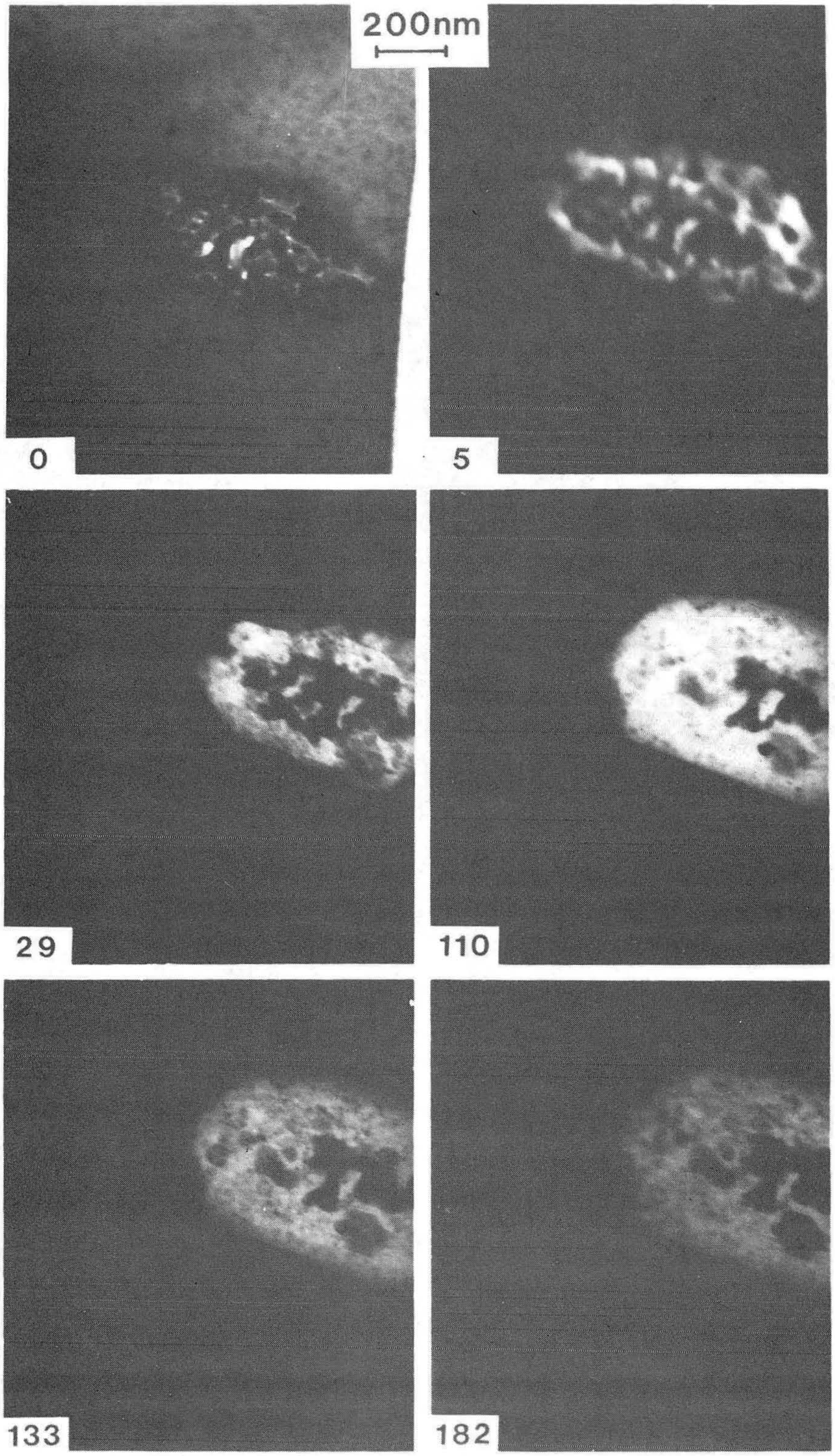

XBB 840-9183

Figure 37.

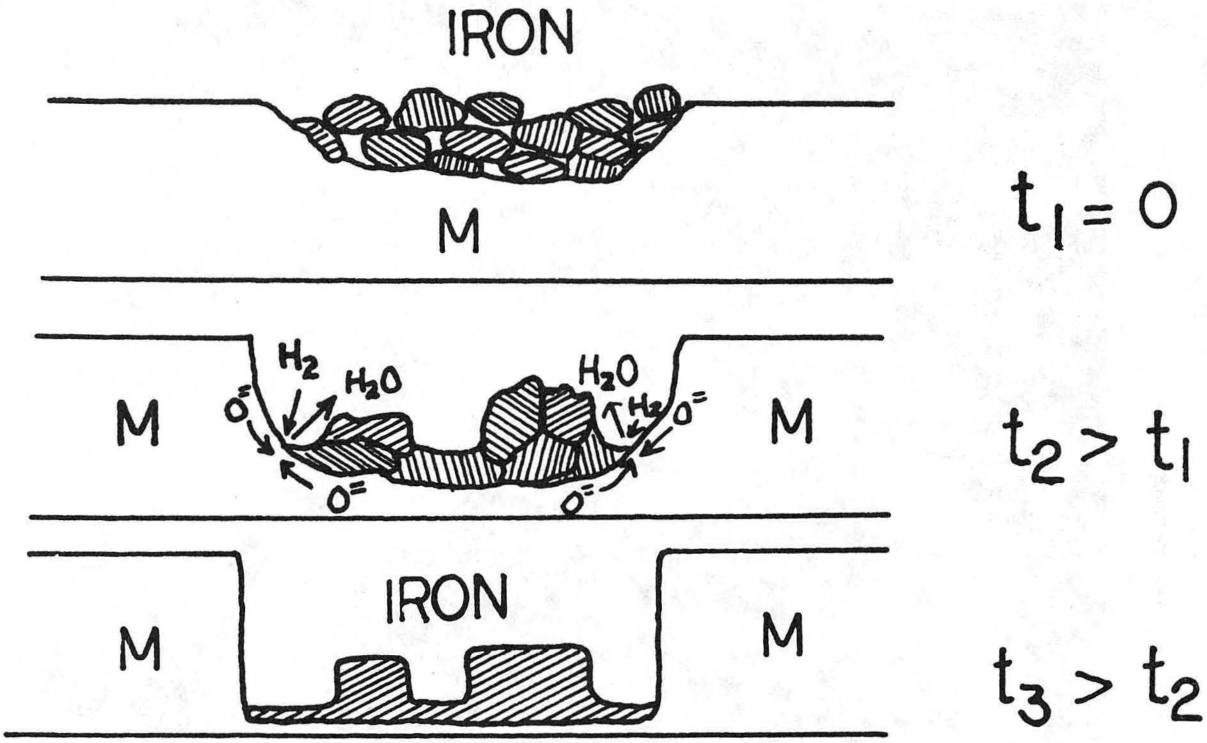

XBL 8412-5443

Figure 38.

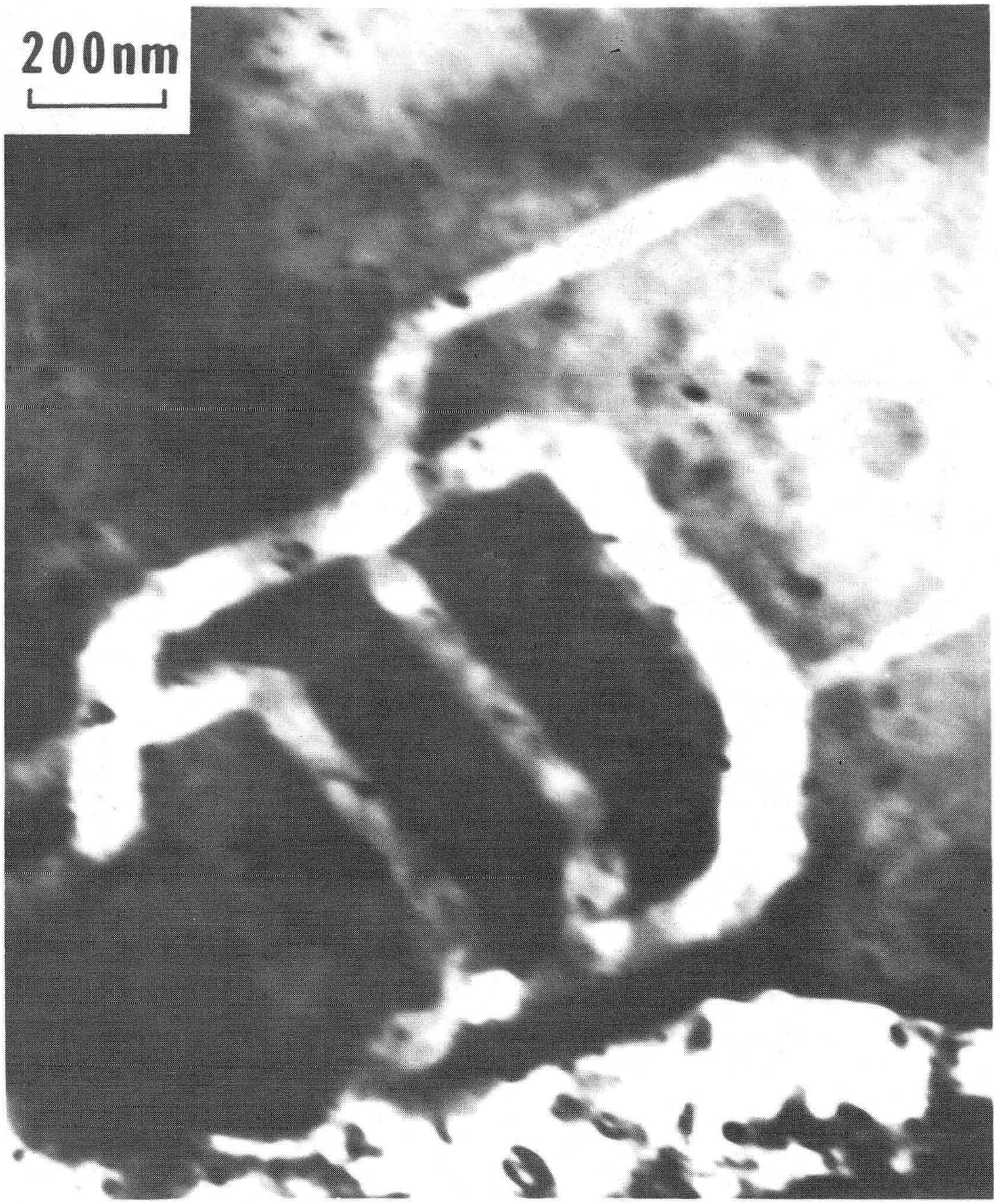

XBB 840-9190

Figure 39.

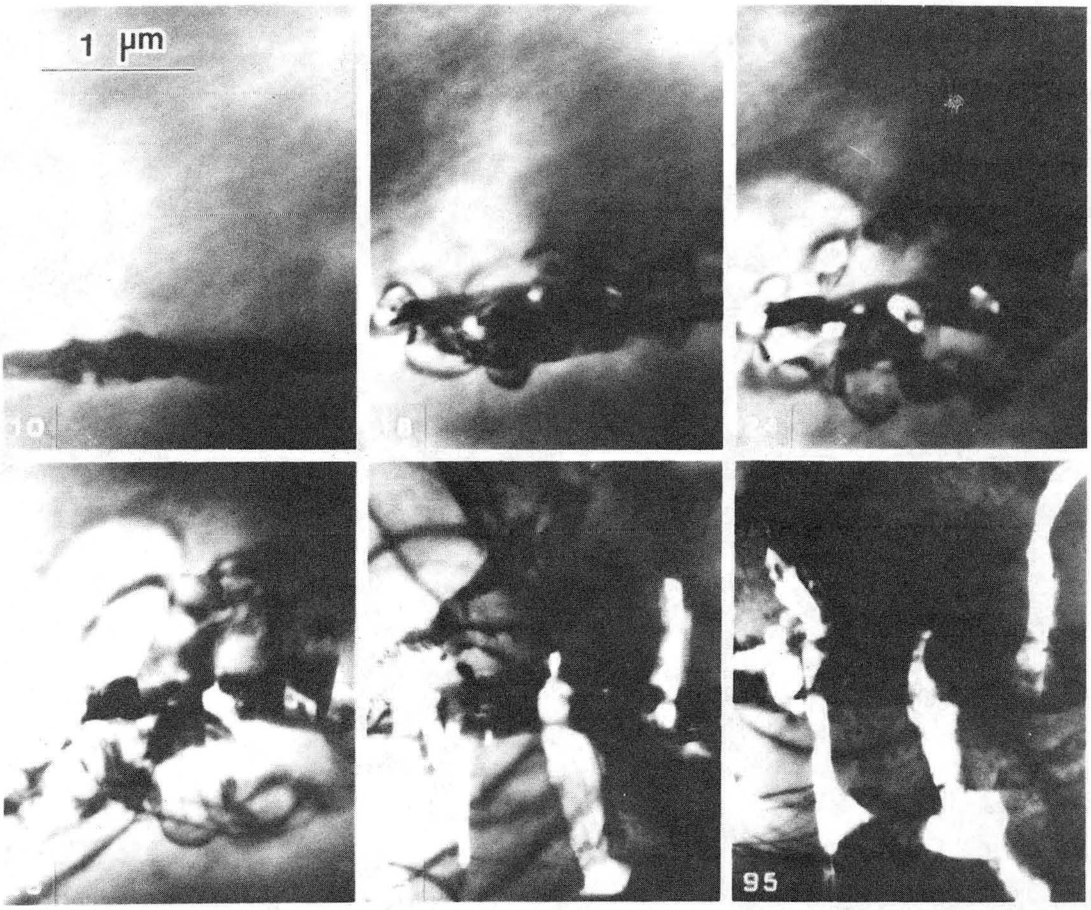

XBB 830-10290

Figure 40.

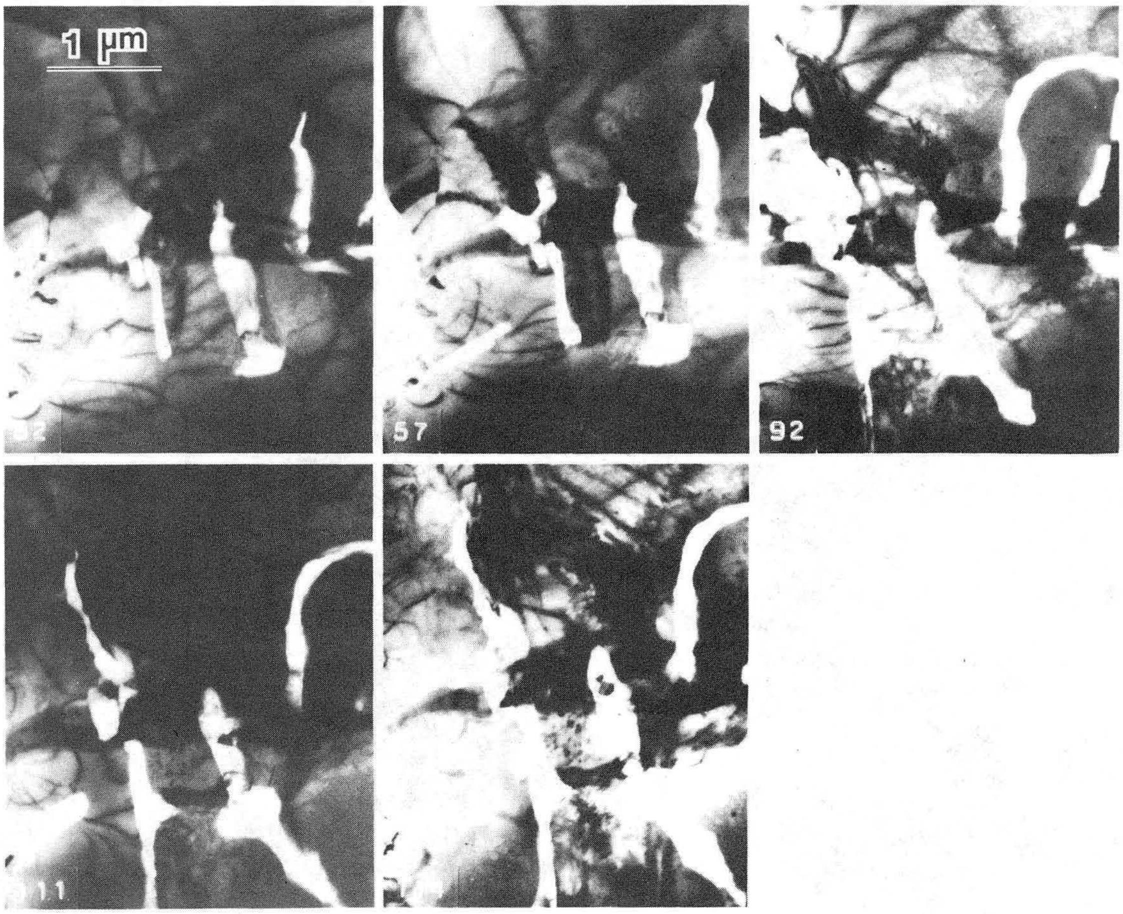

XBB 830-10291

Figure 41.

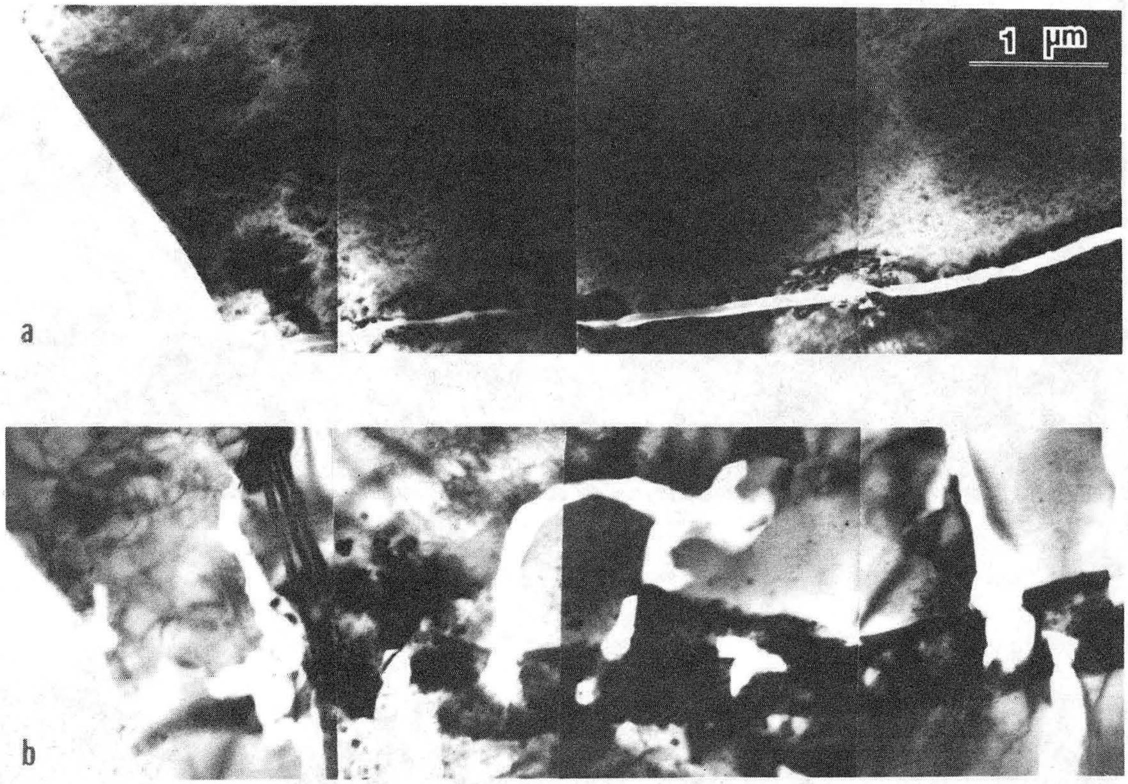

XBB 830-10289

Figure 42.

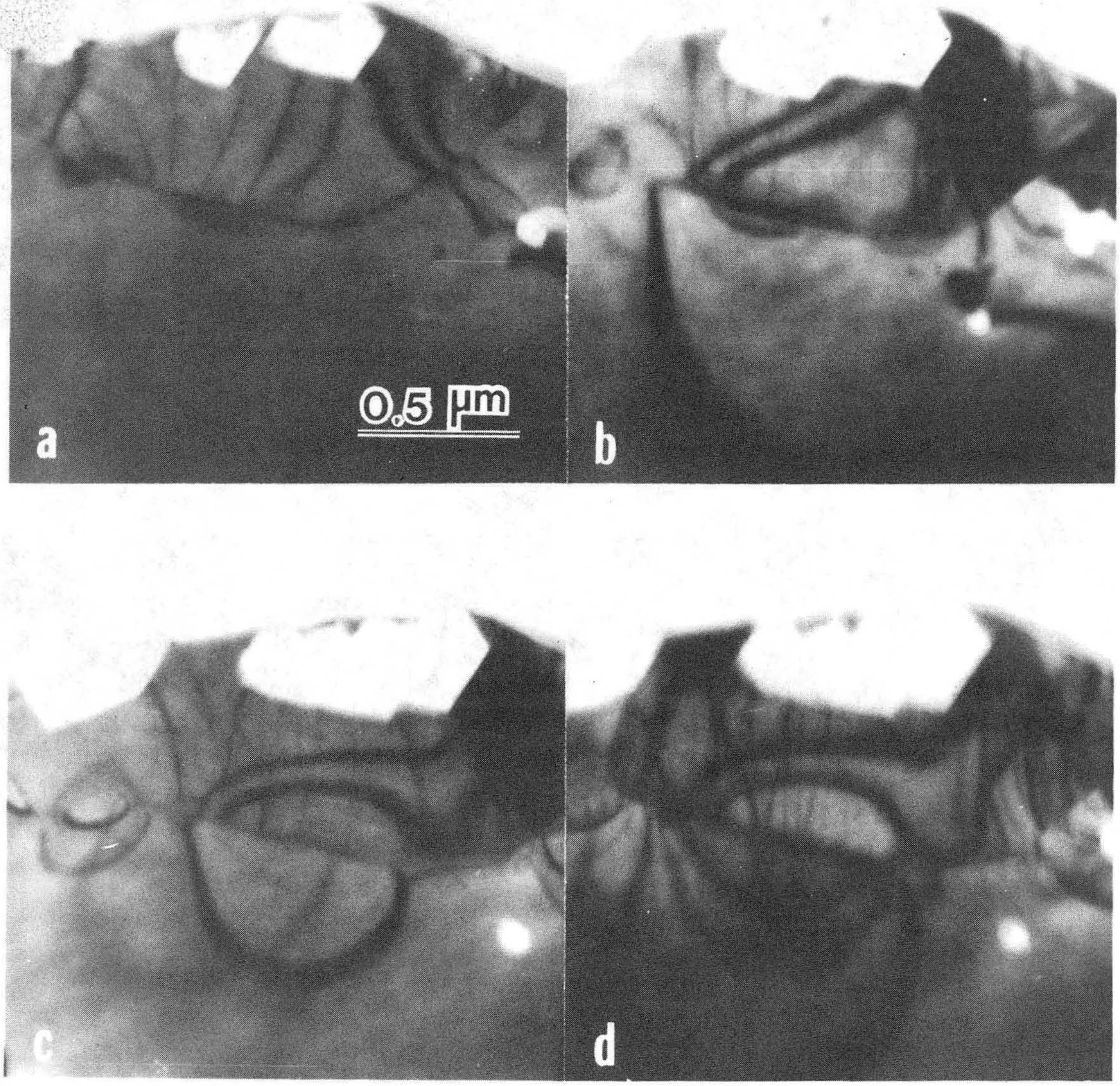

XBB 830-10295

Figure 43.

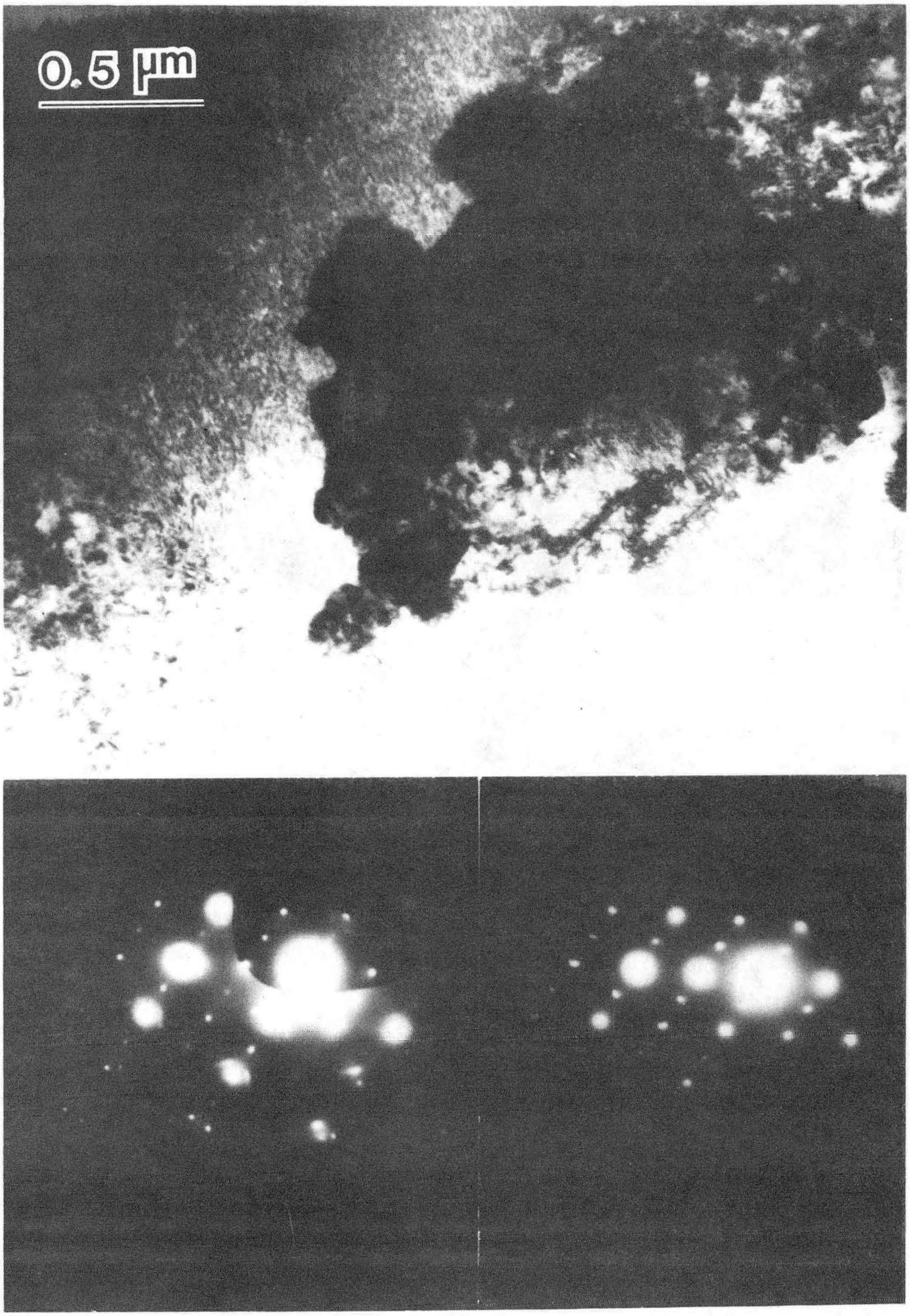

XBB 840-10299

Figure 44.

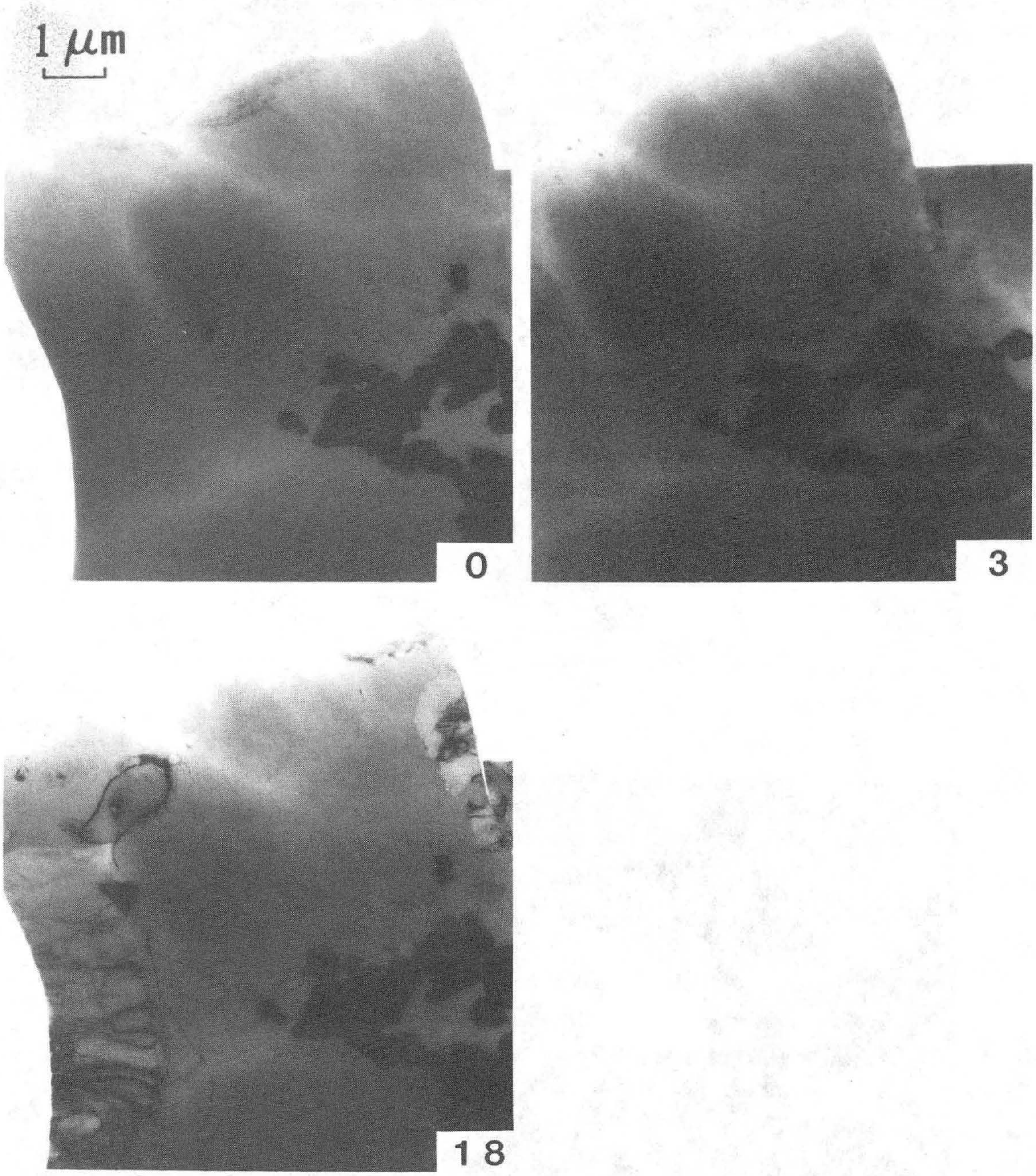

XBB 840-9592

Figure 45.

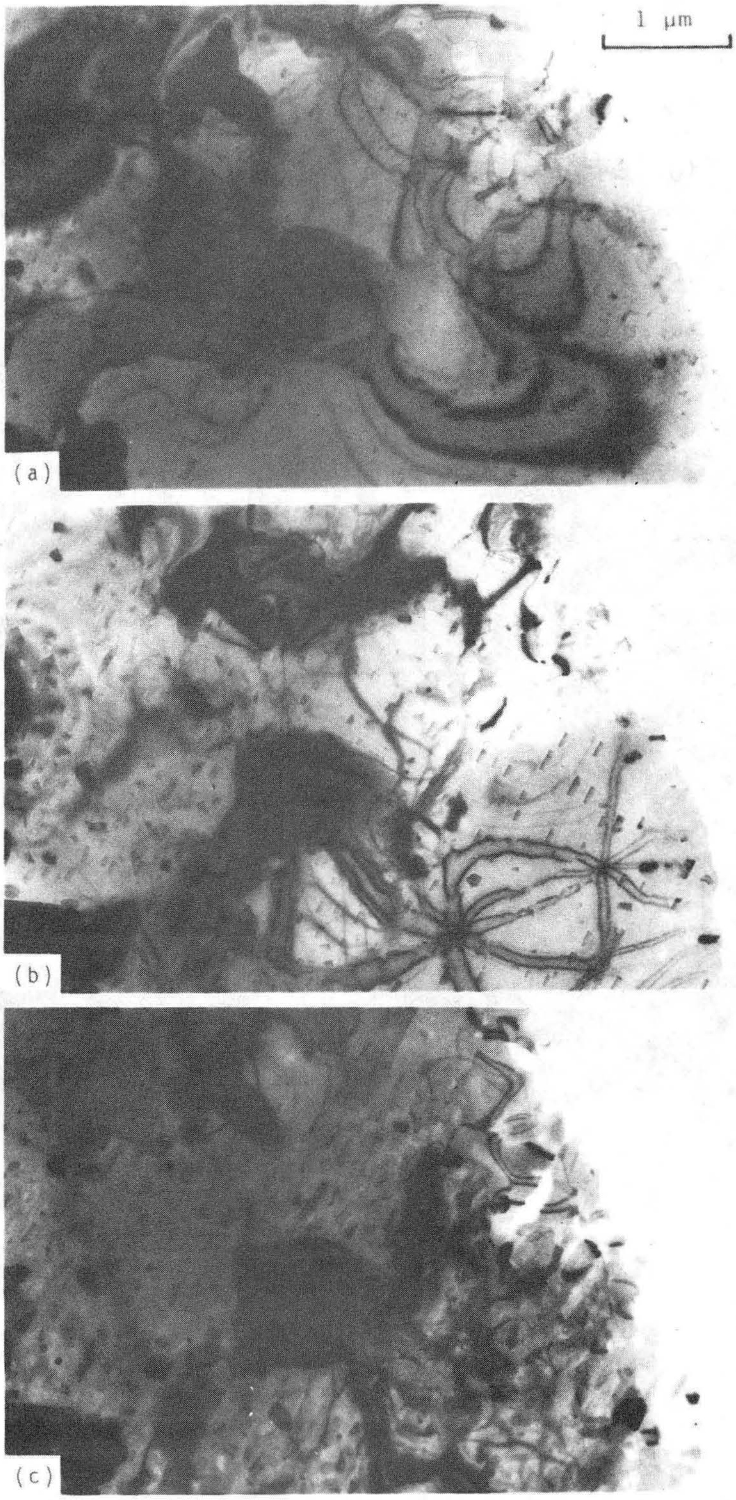

XBB 840-9181

Figure 46.

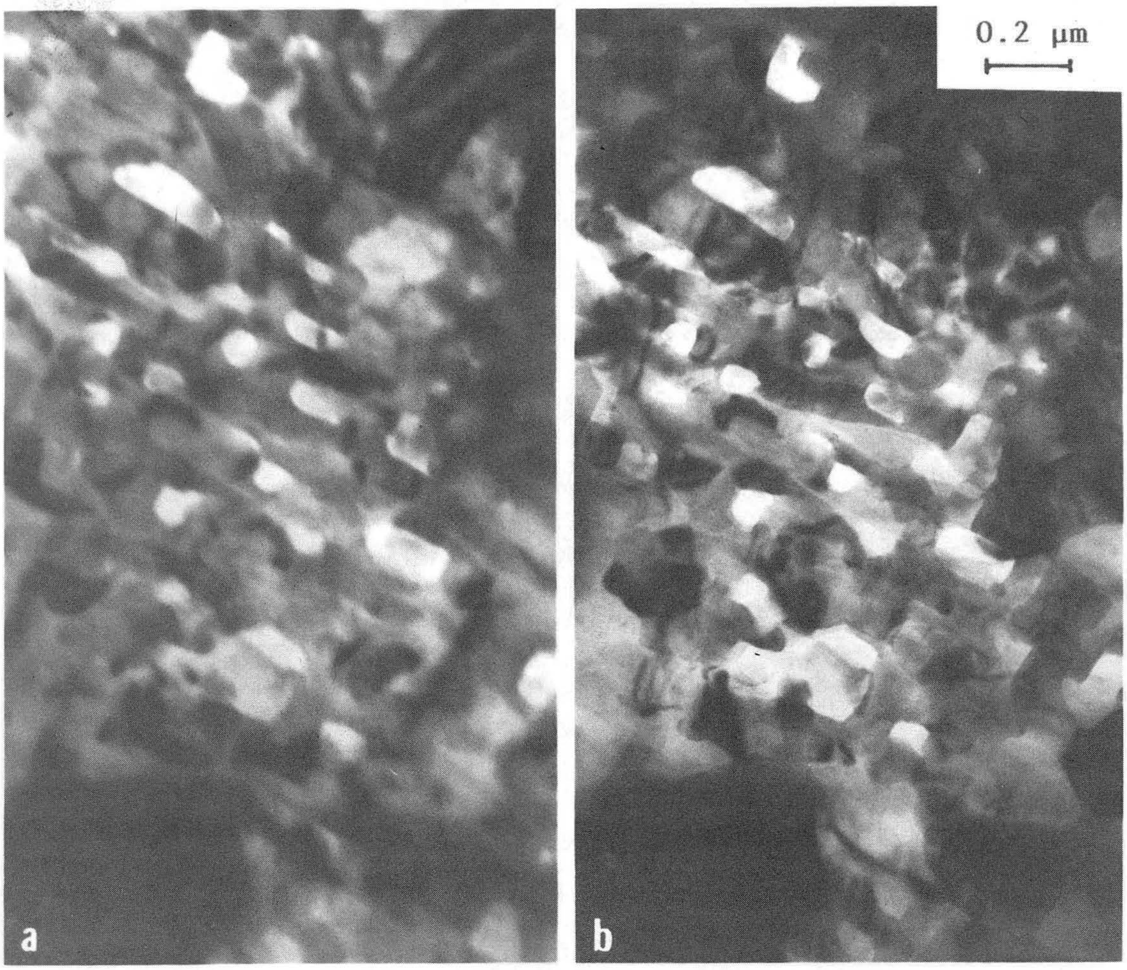

XBB 840-9590

Figure 47.

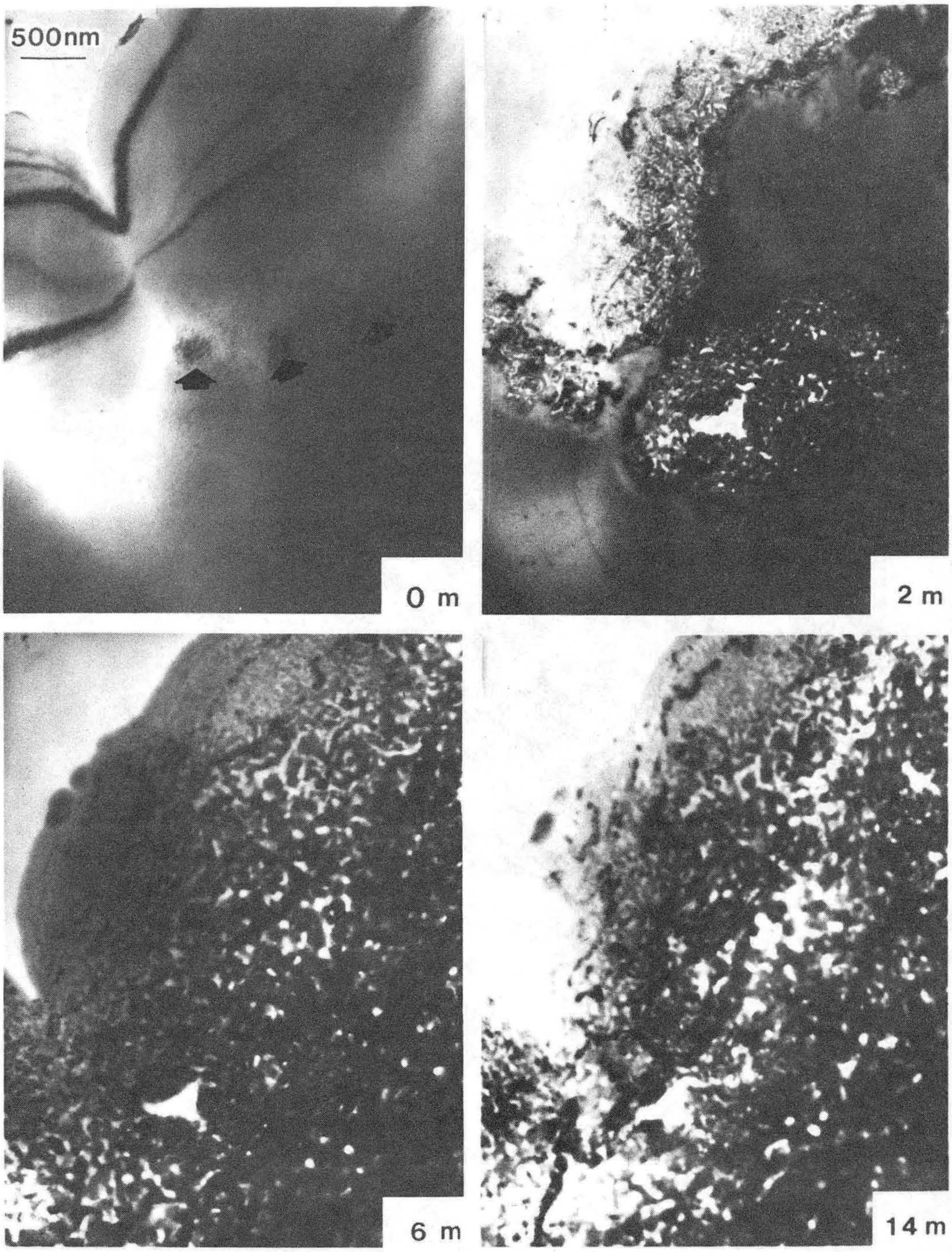

XBB 840-9189

Figure 48.

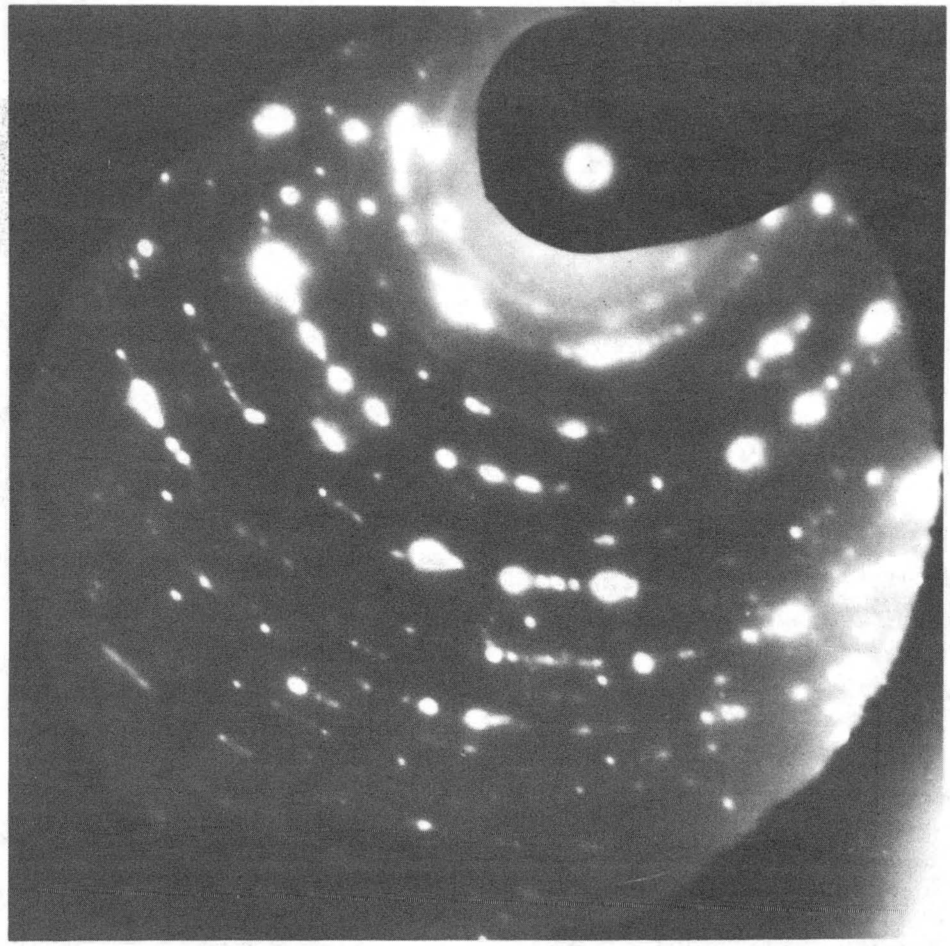

XBB 840-9601

Figure 49.

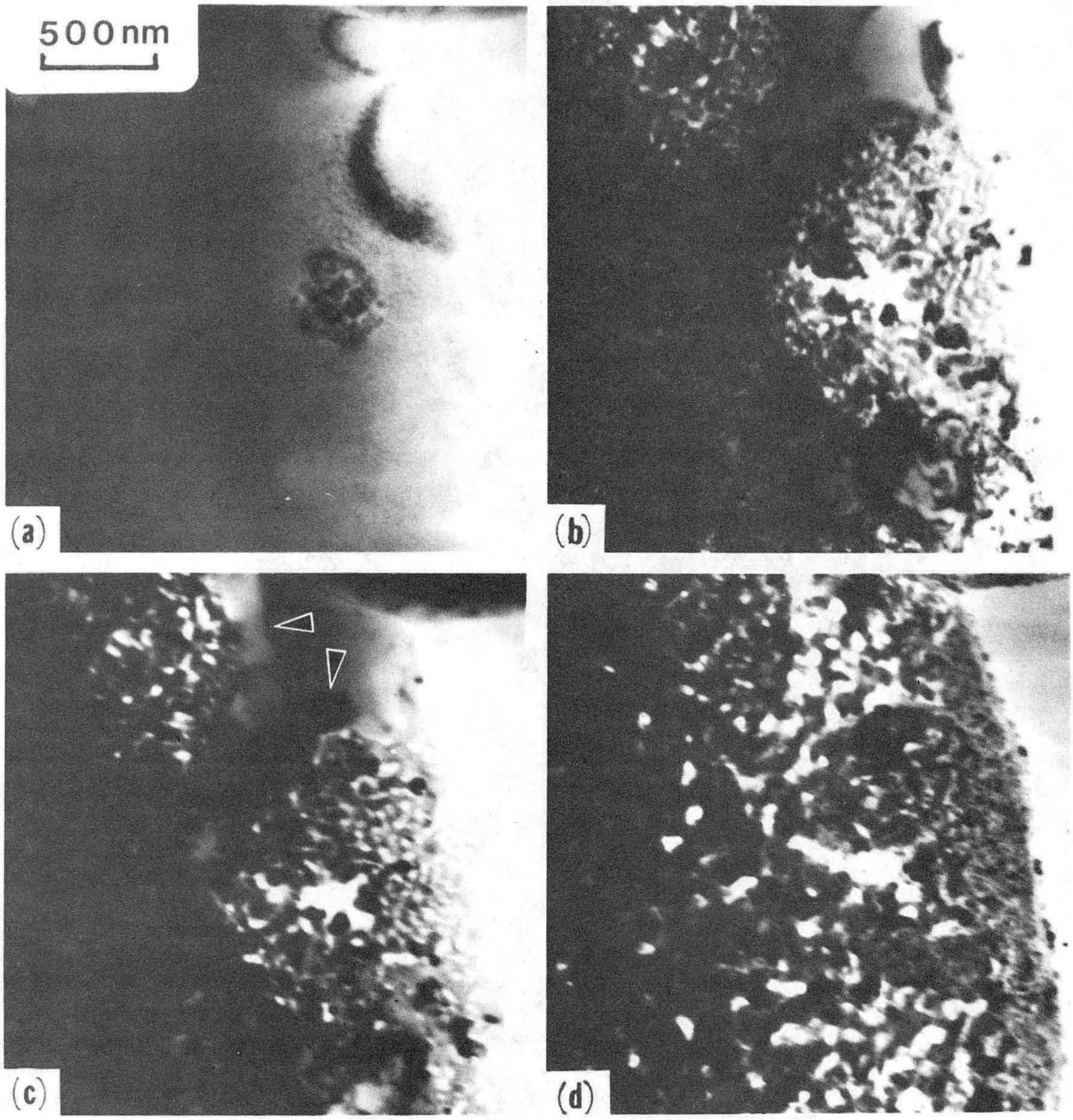

XBB 840-9586

Figure 50.

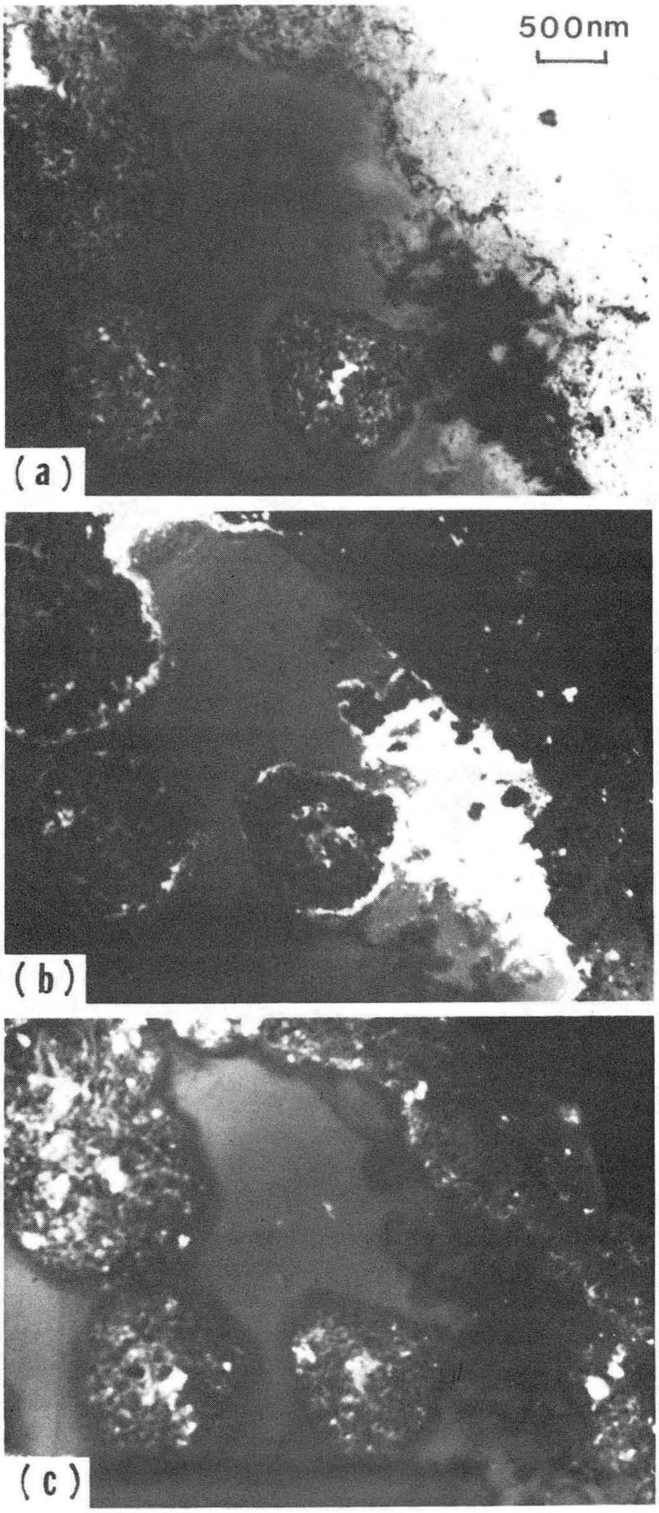

XBB 840-9591

Figure 51.

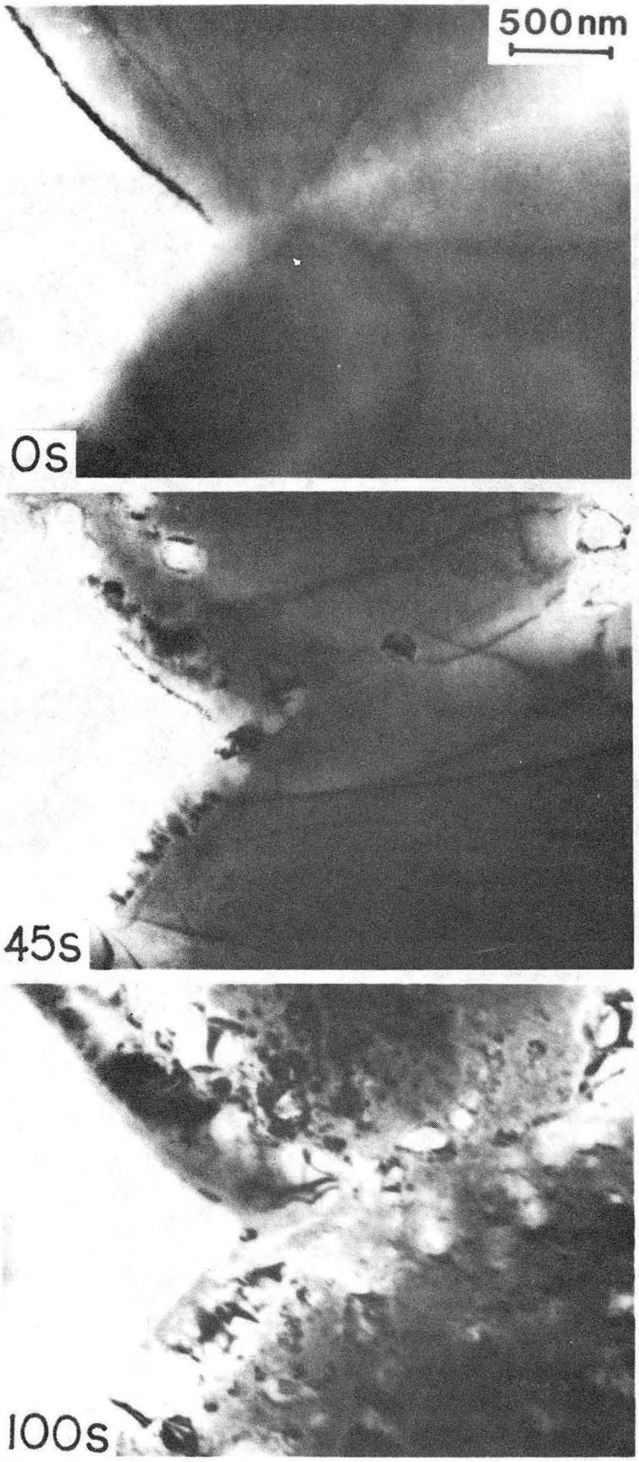

XBB 840-9188

Figure 52.

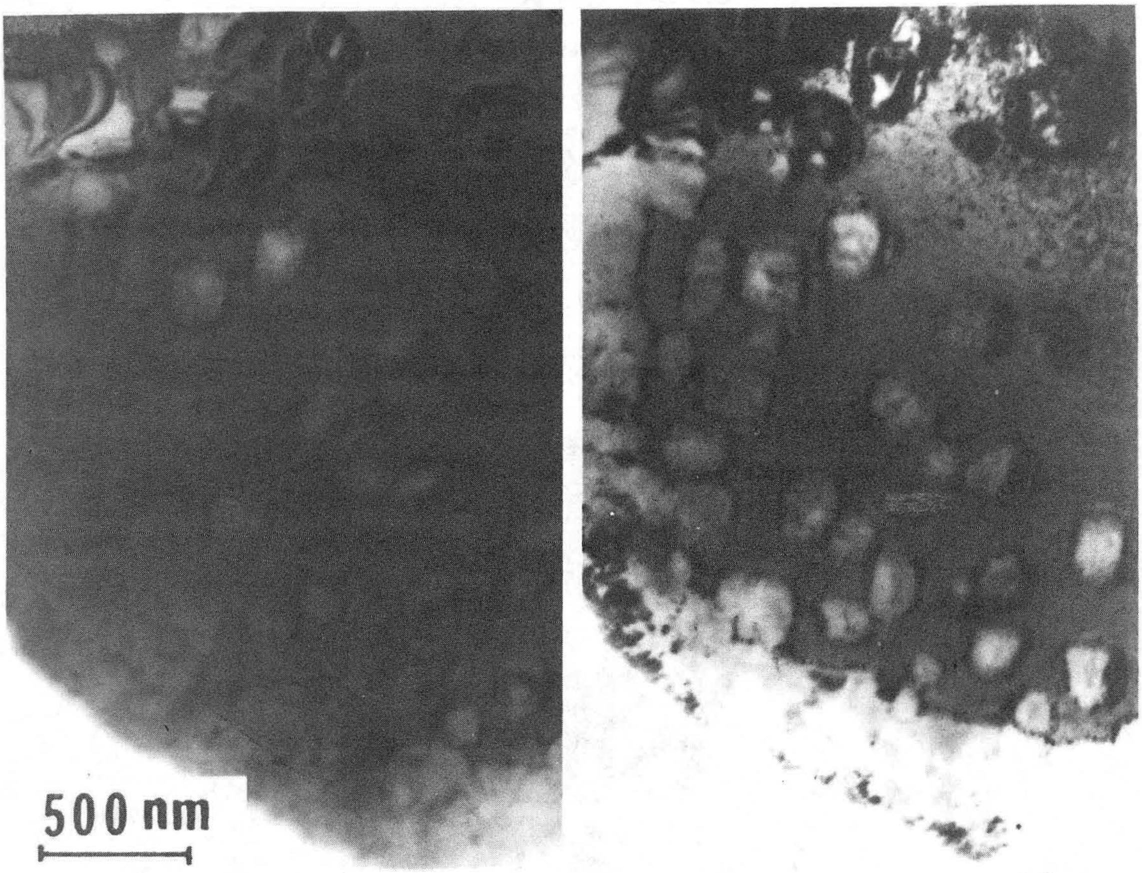

XBB 840-9597

Figure 53.

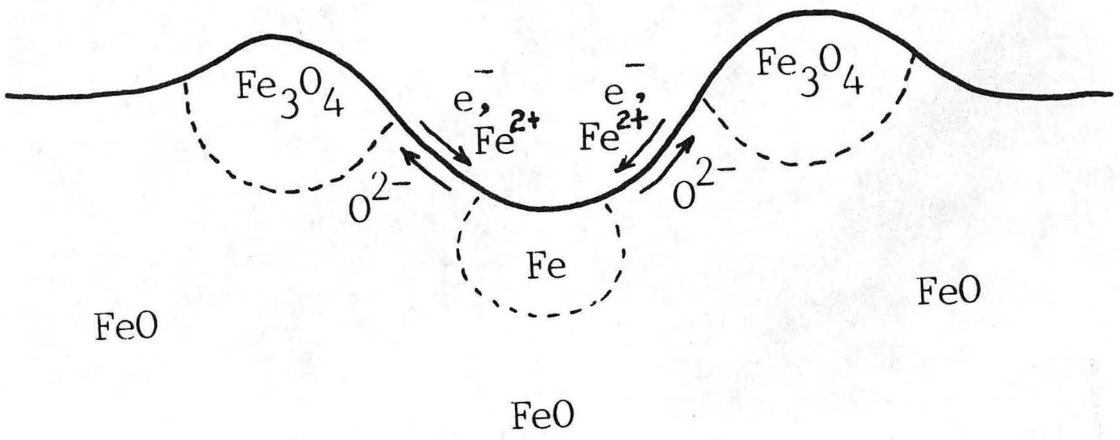

XBL 8412-5445

Figure 54.

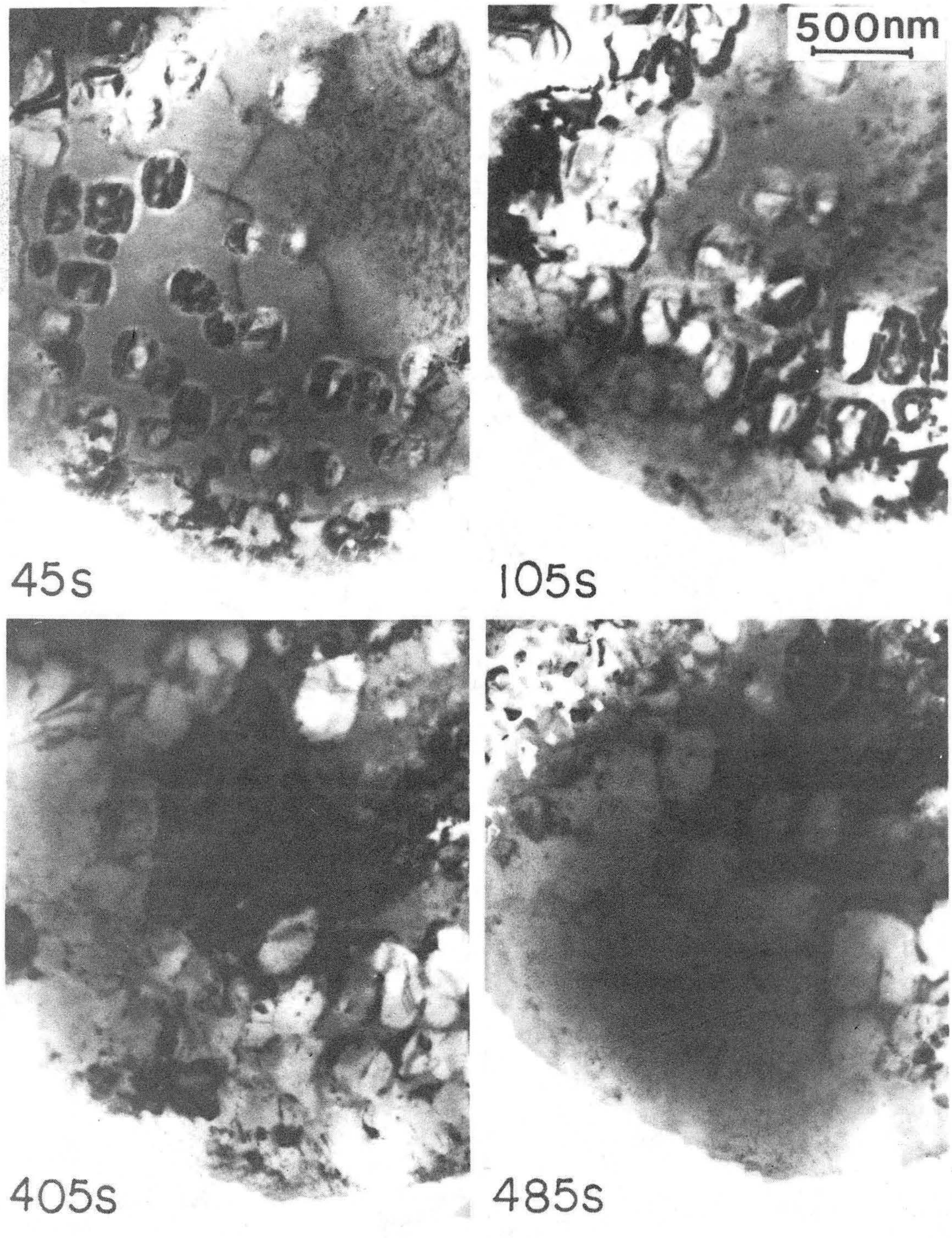

XBB 840-9187

Figure 55.

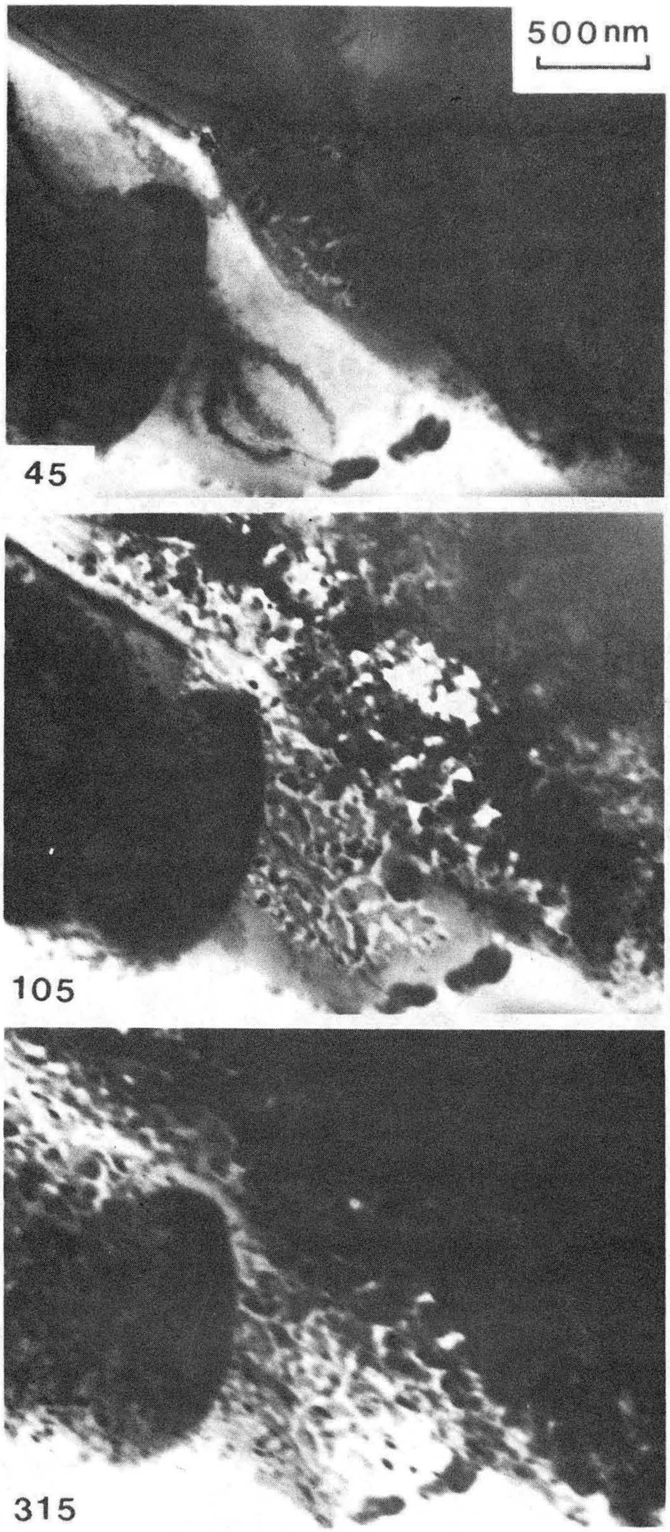

XBB 840-9186

Figure 56.

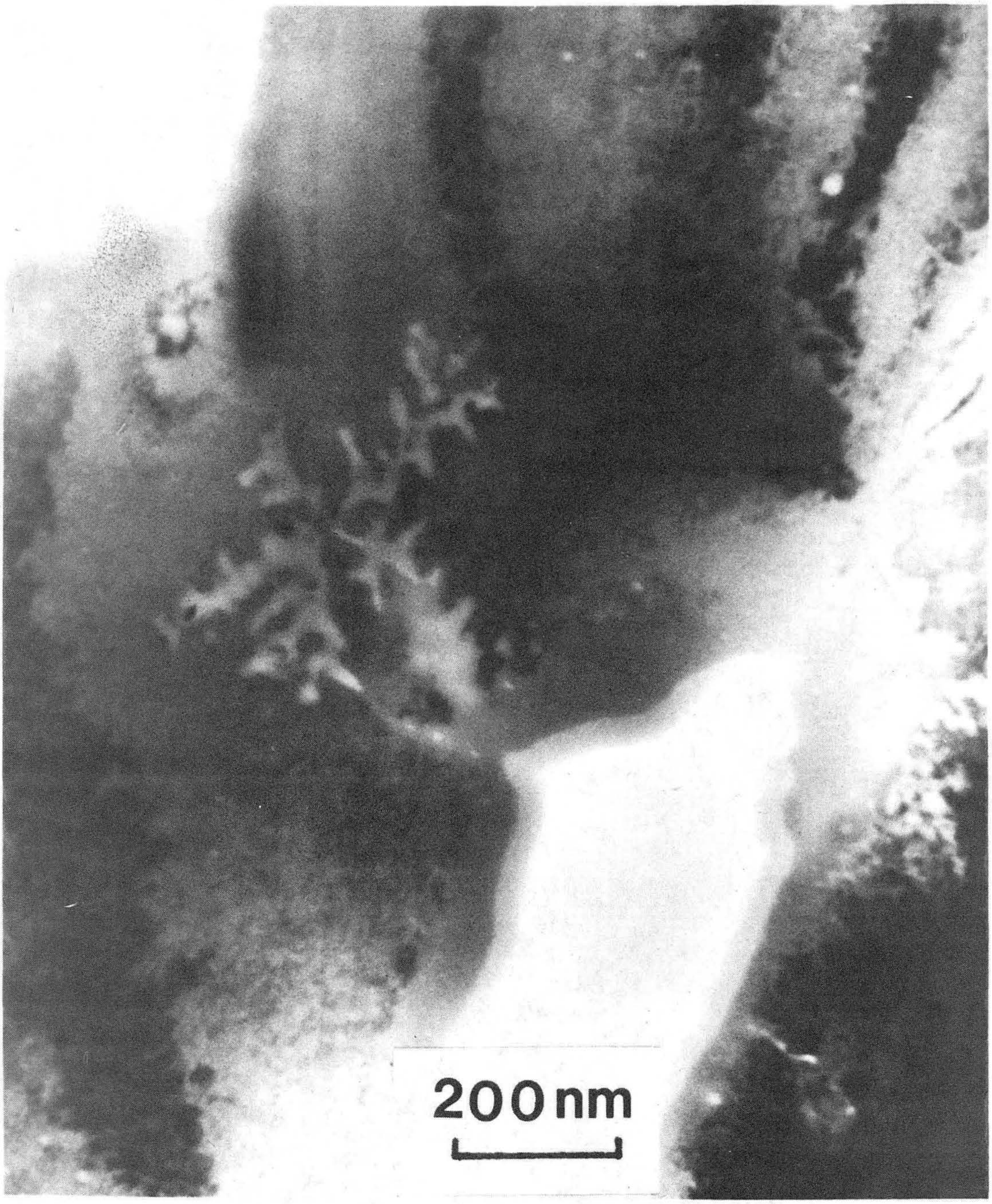

XBB 840-9588

Figure 57.

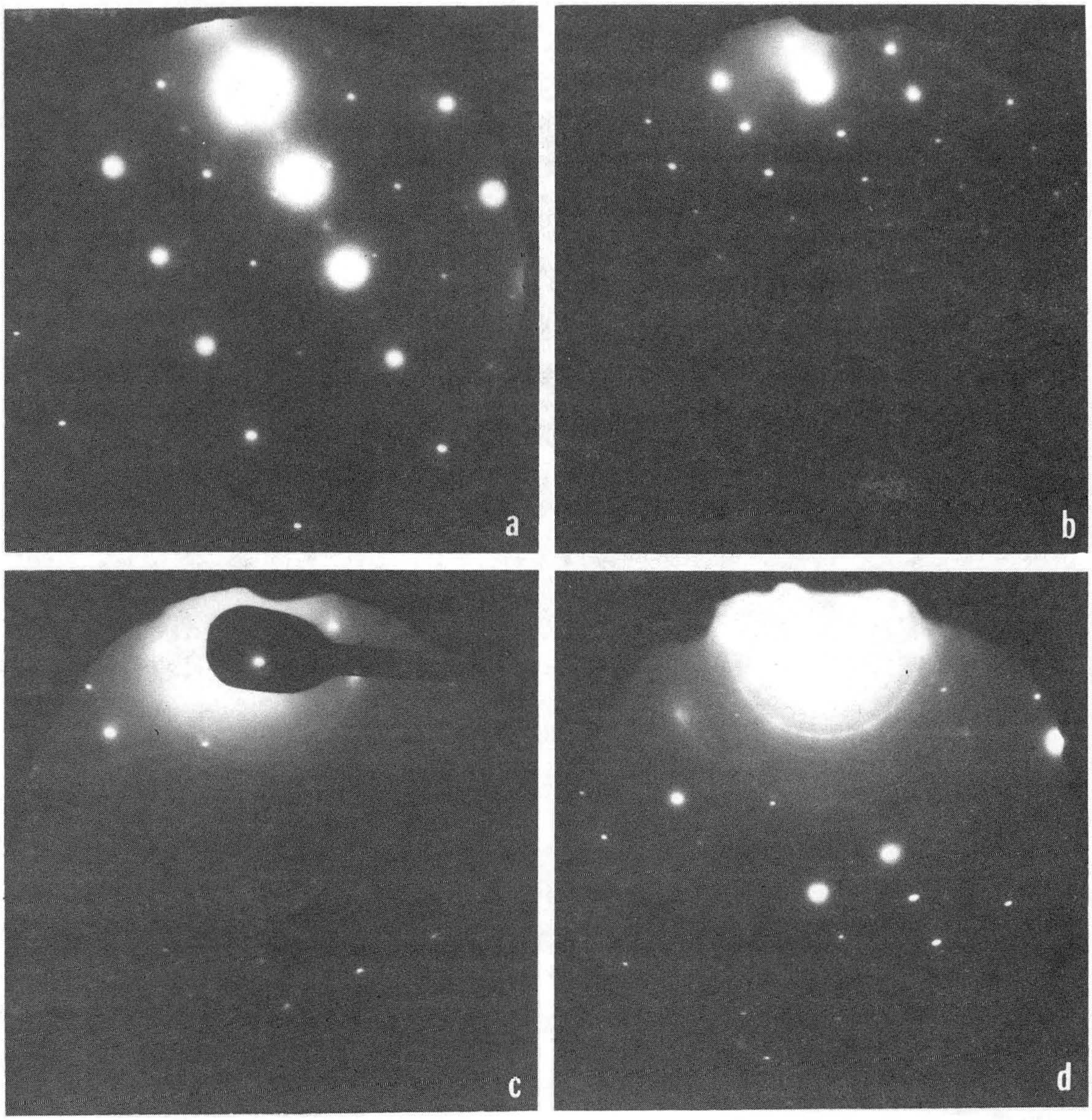

XBB 840-9589

Figure 58.

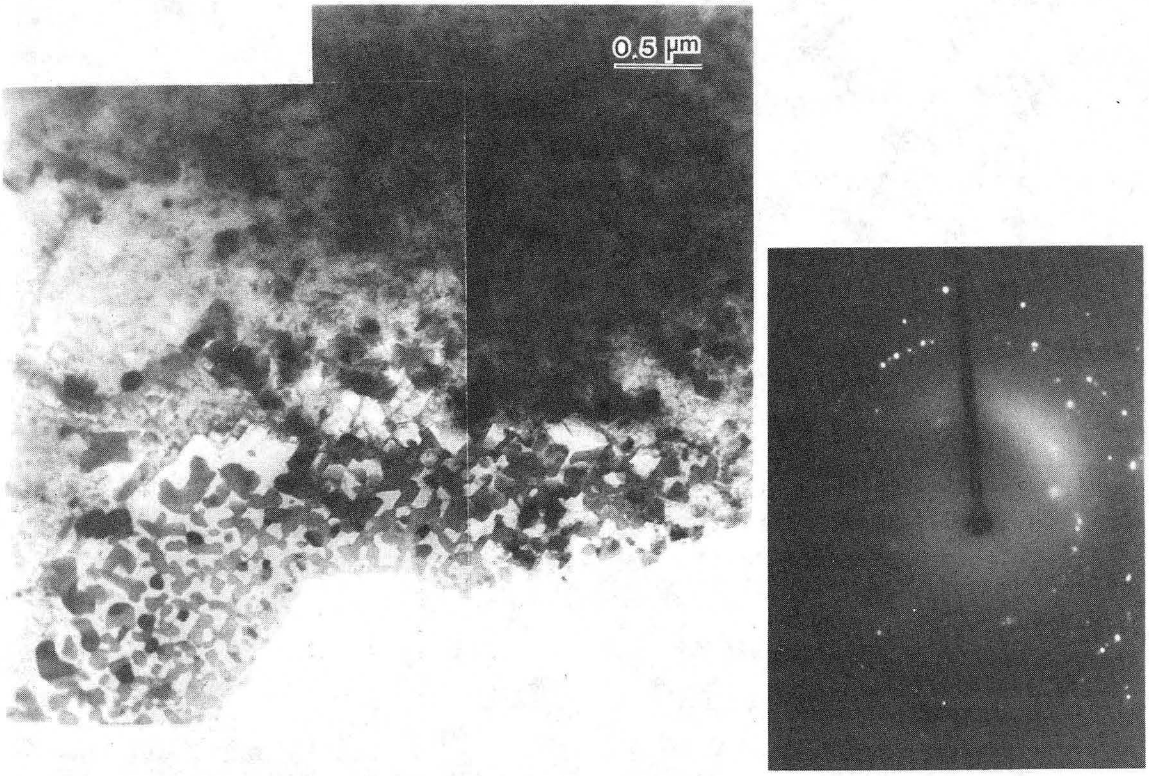

XBB 830-10293

Figure 59.

TECHNICAL INFORMATION DEPARTMENT
LAWRENCE BERKELEY LABORATORY
UNIVERSITY OF CALIFORNIA
BERKELEY, CALIFORNIA 94720